Relativistic Laser Plasma Interaction:
A Novel Route to Intense, Single Attosecond Pulses

Dissertation

vorgelegt von

Patrick Heißler

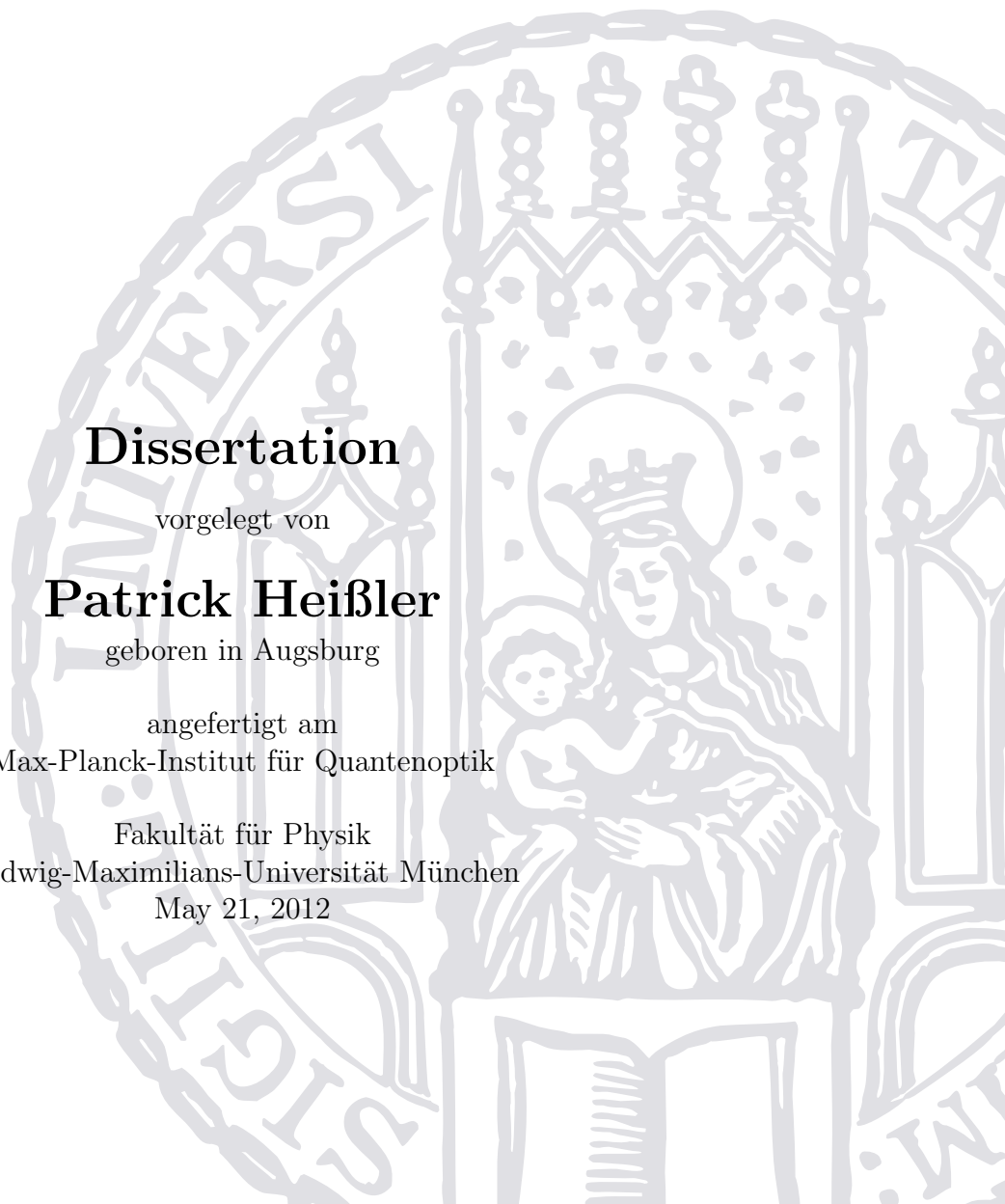geboren in Augsburg

angefertigt am
Max-Planck-Institut für Quantenoptik

Fakultät für Physik
Ludwig-Maximilians-Universität München
May 21, 2012

'Ultimate excellence lies
Not in winning
Every battle'
(Sun-tzu)

Zusammenfassung

Mit fortschrittlichsten Lasersystemen werden heute durch die stark nicht lineare Wechselwirkung des Laserpulses mit einem Edelgas, Lichtblitze im extrem ultravioletten (XUV) Spektralbereich mit Pulsdauern von nur noch $\sim 80\,as$ erreicht, welche Beobachtungen mit Attosekundenauflösung ermöglichen. Diese Pulse sind in ihrer Photonenzahl und damit auch in ihrer Anwendbarkeit jedoch beschränkt und können die hohen Pulsenergien neuester Lasersysteme nicht effizient nutzen.

Diese Doktorarbeit zeigt einen Weg auf, um mit modernsten, hochintensiven Kurzpulslasersystemen, Lichtblitze bisher unerreichter Intensität und einer Pulsdauer im Attosekundenbereich zu erzeugen. Anstelle eines gasförmigen Mediums wird hierfür ein an einer Oberfläche lokal erzeugtes Plasma genutzt. Die Wechselwirkung des Laserpulses mit den auf relativistische Geschwindigkeiten beschleunigten Elektronen erzeugt im reflektierten Puls, zeitlich stark lokalisierte Verschiebungen der Trägerfrequenz des Lasers hin zu höheren Frequenzen. Durch die Anwendung eines geeigneten Filters können die hochfrequenten Teile des Spektrums extrahiert werden und manifestieren sich dann zeitlich als Zug ultrakurzer Pulse und im Extremfall als einzelner Puls mit einer Dauer im Attosekundenbereich.

In den hier beschriebenen Experimenten wird dieser Vorgang erstmals mit einem treibenden Laserpuls, mit einer Pulsdauer von nur wenigen Lichtschwingungen, gezeigt. Anschließend wird die theoretisch vorhergesagte hohe Effizienz des Vorgangs und die Emission in einen Kegel mit kleiner Divergenz experimentell bestätigt. Diese intensiven Lichtblitze werden im letzten Teil der Arbeit schließlich benutzt um den nicht linearen Prozess der zwei Photonen Ionisierung über die Ionisationsschwelle von Argon anzustoßen, was durch die Messung des erzeugten Photoelektronenspektrums gezeigt wird. Dies ist die erstmalige Demonstration eines nicht linearen Prozesses mit ultrakurzen Lichtpulsen aus der beschriebenen relativistischen Plasmaquelle und gleichzeitig die erste Messung von Photoelektronen, welche mittels XUV-Strahlung aus der kohärenten Wechselwirkung eines Lasers mit einer Festkörperoberfläche erzeugt wurden.

Die erhaltenen Ergebnisse dieser Arbeit verdeutlichen das enorme Potential dieser neuartigen Quelle von ultrakurzen Lichtblitzen von bisher unerreichter Intensität. Diese Arbeit ebnet daher den Weg zu ersten Anwendungen dieser Pulse in XUV-XUV Attosekunden-Anrege-Attosekunden-Abfrage-Experimenten.

Abstract

The most advanced laser systems to date allow the generation of flashes of light in the extreme ultra-violet spectral region (XUV) with durations as small as $\sim 80\,as$ by the non-linear interaction of the laser pulse with a noble gas. These short pulses allow for observations with attosecond resolution. However, they are limited in their photon number, and hence, also in their applicability. Additionally, the high pulse energies of novel laser systems can not be used efficiently with this technique.

This thesis paves the road to intense, isolated attosecond pulses by using state-of-the-art high peak power laser systems. Instead of a gaseous medium a plasma that is locally generated on a solid surface is used. The interaction of the laser pulse with the electrons of the plasma that are accelerated to relativistic velocities leads to a temporarily confined frequency up-shift in the reflected light of the carrier frequency of the laser. The application of an appropriate filter separates the high frequencies, which manifest themselves in the temporal domain as a train of ultra-short pulses or in the most extreme case, as a single pulse with a duration in the attosecond regime.

The experiments presented here demonstrate, for the first time, this process which is triggered by a laser pulse with a duration of only a few cycles of its carrier frequency. Subsequently, the theoretically predicted high conversion efficiency and emission into a well defined beam of small divergence are experimentally confirmed. In the last part of the thesis, these intense light pulses are used to trigger a non-linear process, the two-photon above-threshold ionization of Argon, which is shown by the measurement of the generated photo electron spectrum. This is the first demonstration of a non-linear process with ultra-short light pulses from the relativistic laser-plasma interaction and at the same time the first measurement of a photo electron spectrum generated by XUV radiation emanating from the coherent interaction of a laser pulse with a surface plasma.

The achievements of this work show the enormous potential of this novel source of ultra-short flashes of light with unprecedented intensities. Hence, this thesis opens up the route to the first application of these pulses in XUV-XUV attosecond-pump-attosecond-probe experiments.

Contents

Data Storage and Analysis   **109**

Publications   **117**

Acknowledgements   **119**

Curriculum Vitae   **123**

1. Introduction

Since its very beginning, mankind has tried to image and describe the motion of objects surrounding it. Already in the oldest known drawings to date, with an age of ~ 32000 years, the movement of a bison is indicated by multiple drawn legs [1]. In this thesis, the relativistically oscillating mirror (ROM) mechanism, is studied in detail and refined as tool for studying moving entities with unprecedented temporal resolution.

The motion of things has persistently captivated human minds, and especially the paths of the objects in the sky always fascinated people throughout the ages. It was Grecian philosophers like Thales of Miletus ($\sim 600\ BC$) and Aristarchus of Samos ($\sim 300\ BC$) who dissociated these movements from religious believes and put them on a scientific foundation. Another Grecian philosopher, Aristotle ($\sim 300\ BC$), formulated an early theoretical definition of motion in his books on physics [2].

New breakthroughs in the physical understanding of phenomena in our environment are almost always directly connected to technical inventions. For example, the invention of the telescope by Hans Lipperhey in 1608 allowed the pioneering observations of Galileo Galilei, which in turn promoted the work of Nicolaus Copernicus, Johannes Kepler and also Isaac Newton. The telescope and almost simultaneously the microscope allowed for observations with higher spatial resolution, whereas higher temporal resolution, exceeding the bare human eye, were only made possible in the nineteenth century by the use of electricity and the invention of the photographic camera. In 1864, August Toepler [3] used electric discharges to perform the first pump-probe measurements, triggering a sound wave with a first discharge, and then illuminating, or probing, it with a delayed second discharge making thus its evolution over time visible. Producing images similar to the first cave drawings, Eadweard Muybridge was the first in 1878 to capture a 'Horse in Motion' using photographic cameras [4].

Still the temporal resolution was limited by the fastest electronics available, which could only resolve signals in the nanosecond ($1\ ns = 10^{-9}\ s$) regime. The realisation of the laser [5, 6] and the development of laser pulse generation by mode locking [7, 8] and Q-switching [9] for the first time opened up the picosecond ($1\ ps = 10^{-12}\ s$) and even femtosecond ($1\ fs = 10^{-15}\ s$) regimes for observation. By the use of the chirped-pulse amplification technique [10], ever more powerful laser pulses with durations of few femtoseconds [11–13] became available and observations of bond formation and bond breaking in molecules became possible,

starting a whole new field of research called 'Femtochemistry' [14]. In particular the development of chirped mirrors for the accurate control of the dispersion of ultra-short laser pulses [15] enabled the generation of few-cycle pulses down to 1.5 cycles [16] and by applying advanced techniques for the control of the electric field [17, 18], even down to 0.88 cycles [19]. But observing processes, like the dynamics of electron wave packets, on even shorter time scales [20], i.e. on the order of hundreds of attoseconds ($1 \, as = 10^{-18} \, s$) or less, is again asking for a novel technique for the generation of such short light pulses. The generation of ever shorter laser pulses is limited by the duration of a single cycle of the carrier frequency of the pulse. For a pulse with a central wavelength of $800 \, nm$, the duration of one cycle is $2.67 \, fs$, hence a transition to shorter wavelengths is needed in order to be able to generate light pulses of shorter duration.

The state of the art technique for the generation of light pulses with durations as short as $80 \, as$ [21] is the non-linear interaction of a moderately intense laser pulse with a noble gas [22–24]. During the interaction, the electric field of the laser increases in strength to the point, that an electron is freed from an atom and accelerated. During the next half-cycle, the electric field changes its polarization, and the electron is hurled back to the atom and re-collides emitting a high energy photon [25] with energies reaching the extreme ultra-violet (XUV) or even soft x-ray regime. This process happens twice per cycle of the laser field. This periodicity leads to an emitted spectrum consisting of odd high-order harmonics of the frequency of the driving laser that is formed by Fourier synthesis of the individual, continuous spectra of the temporarily equally spaced pulses [26, 27]. One can intuitively see that for few-cycle driving laser pulses, the absolute position of the electric field under the temporal envelope of the pulse, that is defined by the so-called carrier envelope phase (CEP) is very important in this process [16]. For example, for a cosine like pulse, where a maximum of the oscillations of the electric field coincides with the maximum of the envelope of the pulse, the electrons accelerated during this strongest single half-cycle reach higher energies and are hence emitting photons of higher energies when re-colliding with their atoms [28]. Here a transition from the spectrum of odd harmonics to an unmodulated cut-off is observed for the highest frequencies generated. By applying the right spectral filter, and selecting only the part of the spectrum within the cut-off, a single pulse with sub-femtosecond duration can be extracted [29]. The stabilization of the CEP of the driving laser pulses [30, 31] is hence a prerequisite for the steady generation of isolated, attosecond (as) pulses.

The availability of these pulses directly led to an upsurge of experiments probing the dynamics of electronic wave packets with a time resolution down to a few attoseconds in gases [19, 23, 32–35], solids [36] and nano-structures [37]. A major problem of these investigations is the low pulse energy of the attosecond pulses. This low energy per pulse has two origins. First, the conversion efficiency, since it is a highly non-linear process, is very low, with values on the order of $\sim 10^{-5}$

[38]. Second, the applicable laser intensity for driving the process is limited to levels below $\sim 10^{15} \, \frac{W}{cm^2}$ before saturation sets in due to the ionization of the gaseous medium [39]. Accordingly the highest attosecond pulse energies reported to date have few tens of nJ in energy in the $20 - 40 \, eV$ spectral range [38, 40]. Due to the small energies available per pulse, the aforementioned experiments rely on cross-correlation techniques. This means, that instead of splitting one XUV-attosecond pulse into two and using one pulse as a trigger for the electronic wave packet and the other, delayed pulse as a probe, the evolution of the electrons is visualized with the residual infra-red (IR) driving laser. The attosecond pulse generates photo electrons which experience a shift in energy and angular distribution depending on the phase of the ambient electric field of the IR laser at the specific point in time of their generation [41]. The mechanism is hence very similar to a classical streak camera that relies on temporarily changing electric fields between deflection plates and is accordingly named attosecond streaking. The problem that arises with this approach is that the applied IR field has substantial influence on the measured quantities [42, 43] and can lead to ambiguous results.

For all measurements of temporal quantities, detailed knowledge of the temporal structure of the light pulses is crucial [44]. In the spectral region of interest in attosecond metrology, i.e. the XUV- and soft x-ray regime, conventional characterization techniques known from fs-metrology and based on the non-linear response of crystals is not applicable due to the lack of active material. Hence an adaptation of these techniques to much shorter wavelengths is needed. Multi-photon ionization processes in atoms provide a non-linear response in the spectral region of interest and can be exploited for pulse characterization techniques [45]. A direct implementation of the second-order auto-correlation technique for example is possible by using two-photon ionization of atoms [46] and has been already realized for trains of attosecond pulses [47–49] as well as XUV-pulses with durations of a few fs [50–53]. The temporal characterization techniques therefore rely on the detection of either photo electrons or their respective ions. To generate measurable amounts of these charged species, the low cross-sections of the multi-photon processes in gases [54, 55] require high XUV intensities in the interaction region. The limited pulse energy of state of the art sources of isolated attosecond pulses from gaseous media prohibits the use of the auto-correlation technique and demands reverting to cross-correlation techniques with the driving IR laser. Two methods have been successfully implemented in this respect. The reconstruction of attosecond beating by interference of two-photon transition (RABBIT) technique relies on a two-photon process where an electron is photo-ionized by an XUV-photon and then, in the field of the IR laser, gains or loses the energy corresponding to one IR-photon. Accordingly, in the photo-electron spectra, side-bands occur between two neighbouring harmonic photo-electron peaks which are modulated with the delay between the XUV- and IR-pulse [24]. This modulation

gives insight into the relative spectral phase of the harmonics, but for trains of pulses, gives only averaged values [56]. The second technique is directly connected to the streaking measurements that were discussed before and named frequency resolved optical gating (FROG) for complete reconstruction of attosecond bursts (CRAB) [57]. Streaking curves are measured, and an algorithm extracts the temporal envelope as well as the phase of the attosecond pulse [21, 56, 58, 59]. To overcome the limitations on pulse energy, extensions of the attosecond pulse generation technique in gaseous media are considered such as the use of already ionized atoms [60]. An especially promising way to achieve higher attosecond pulse energies is the optimization of the phase matching between the laser and the XUV pulse over longer periods directly [61, 62] or by a scheme called quasi phase matching [63–65].

In this thesis, a different approach to the generation of an isolated attosecond pulse with unequalled intensity is followed. The generation relies on the interaction of an ultra-intense laser pulse with a solid surface. The strong electric field of the laser detaches the electrons of the atoms the solid target consists of and a surface plasma forms. The electrons then perform an anharmonic motion in the electric field resulting from the oscillating field of the laser and the field of the static ion background. This electronic motion strongly alters the reflected laser field and leads to the formation of sharp gradients in its temporal profile. Due to symmetry breaking on the surface, this process only happens once per cycle, thus resulting in even and odd harmonics in frequency space. Applying the right filters to this spectrum, as in the case of gas harmonics, then results in the generation of trains of pulses with a duration in the attosecond regime and with sufficiently short driving pulses or gating techniques in isolated attosecond pulses. Since the process relies on plasma formation on a solid surface, there is no intrinsic limitation on the intensity of the driving laser pulse allowing the use of state of the art high power laser systems exceeding focused intensities of $10^{19} \frac{W}{cm^2}$. In fact, using higher driving laser intensities raises the conversion efficiency into the XUV-attosecond pulse η_{XUV}, and values up to $\eta_{XUV} \approx 10^{-2}$ are predicted [66].

Scientific studies on high-harmonic generation from solid surfaces have been performed for more than 30 years [67–69], and a short historical introduction can be found in chapter 3 and, in more detail in references [70–72]. Despite the history of high-harmonic generation from solid surfaces there are still a lot of unanswered questions, and no source for readily available isolated attosecond pulses based on this concept has yet been established.

1.1. Outline

The experiments presented in this thesis aim at characterizing and understanding the physical processes necessary for the operation of the first dedicated beam-line for the application of attosecond pulses from solid surfaces in XUV-XUV attosecond-pump-attosecond-probe-type experiments. These measurements include the generation of high harmonics with a driving laser having an unrivalled combination of a few-cycle pulse duration with pulse energies of $\sim 100\,mJ$ [73], the determination of the efficiency of the generation process, the divergence and focusability of the emitted harmonic radiation, and the initiation of a non-linear process with these harmonics.

The achieved results demonstrate that the generation of isolated attosecond pulses with few-cycle driving lasers is possible and opens the route to pump-probe-measurements using these pulses [74]. They show that the XUV conversion efficiency reaches the high values predicted by simulations, and the harmonics are emitted in a cone with a small divergence and can be focused down to spots of a few micrometers (μm) in diameter [75]. This allows the use of this kind of XUV radiation for prompting two-photon above-threshold ionization and energy resolved measurement of photo electrons in an argon gas jet [76], which in turn can be used for measurements in the XUV spectral region equivalent to the FROG measurements that are well known from fs-pulse metrology [77].

The achievements of the performed experiments in the characterization, optimization and application of high-order harmonics from solid surfaces together with the design, assembly and commissioning of a dedicated beam-line will facilitate the full spectral, spatial as well as temporal characterization of the generated attosecond pulses and their application in XUV-XUV attosecond-pump-attosecond-probe-type experiments.

Before the presentation and discussion of the experimental results in chapter 2 the basic concepts of the interaction of ultra-intense laser pulses with solids are briefly reviewed.

In chapter 3 the two mechanisms, coherent wake emission (CWE) and the relativistically oscillating mirror, responsible for the generation of high-order harmonics on solid surfaces are introduced, and their properties and characteristics are discussed. Special attention is paid to the prospects of isolated attosecond pulses generation.

The generation for the first time of high-order harmonics by the ROM process with a few-cycle driving laser is presented in chapter 4. The employed experimental setup and basic concept as well as parameters of the laser, the light wave synthesizer 20 (LWS-20) are described. The obtained results, together with the considerations of section 3.3 demonstrate the occurrence of isolated attosecond pulses. The results are published in [74].

The conversion efficiency and harmonic beam-profile are addressed in chapter 5. The basic concept of the ATLAS system, the laser that was used for these and following measurements, is introduced, the operational parameters are given, and the experimental setup is explained. The measurements show high conversion efficiencies in agreement with simulations and emission into a well defined cone. A strong dependence of the spatial as well as spectral properties on the conditions of the pre-plasma formation is found.

In chapter 6, the first measurement of photo electrons generated by a non-linear process, the two-photon above-threshold ionization of argon atoms, triggered by harmonic radiation from solid surfaces is presented. To achieve this outcome, a sophisticated beam-line was constructed which is explicitly discussed. For full control over the focused XUV radiation, detailed measurements of the XUV focus are performed which yield an upper limit for the size of the XUV spot. Subsequently the measurement of single-shot two-photon above-threshold photo-electron spectra is presented, which is the first demonstration of a non-linear process triggered by ROM harmonics. This paves the way towards a FROG-type measurement in the XUV-spectral region for full, direct temporal characterization of attosecond pulses. Two publications resulted from the work shown in this chapter [75, 76].

A summary of all the results shown in the preceding chapters is given in chapter 7. Prospective new target materials, which relieve limitations of the state of the art solid discs, and an advanced single-shot technique for the temporal characterization of isolated attosecond pulses as well as pulse trains are given.

2. High-Intensity Laser Pulses and Solid-Density Plasmas

This chapter will give the theoretical framework for the discussion of the results of this thesis shown in the following parts. It gives an introduction to the physics of the interaction of intense laser pulses with solid matter and the conditions leading to the generation of high-order harmonics of the fundamental laser wavelength. Since this field is much broader than the scope of this thesis and still constantly evolving, the discussion in this chapter is by no means complete. It will rather cover the most important aspects needed for the analysis of the findings in the following chapters.

2.1. Laser Pulses at High Intensities

Laser pulses are short bursts of electromagnetic radiation. The framework for their description is hence given by the Maxwell equations (in SI units)

$$\nabla \cdot \mathbf{E} = \frac{1}{\epsilon_0}\rho, \tag{2.1}$$

$$\nabla \times \mathbf{E} = -\frac{\partial \mathbf{B}}{\partial t}, \tag{2.2}$$

$$\nabla \cdot \mathbf{B} = 0, \tag{2.3}$$

$$\nabla \times \mathbf{B} = \mu_0 \mathbf{J} + \mu_o \epsilon_0 \frac{\partial \mathbf{E}}{\partial t}, \tag{2.4}$$

which connect the electric field $\mathbf{E}$, the magnetic field $\mathbf{B}$, the current density $\mathbf{J}$ and the charge density ρ in vacuum. The constants ϵ_0 and μ_0 are the permittivity and permeability of free space. These equations lead, with the introduction of potentials

$$\mathbf{B} = \nabla \times \mathbf{A}, \tag{2.5}$$

$$\mathbf{E} = -\nabla \cdot \Phi - \frac{\partial \mathbf{A}}{\partial t} \tag{2.6}$$

and the use of the Lorentz gauge [78]

$$\nabla \mathbf{A} = -\mu_0 \epsilon_0 \frac{\partial \Phi}{\partial t}, \tag{2.7}$$

to the inhomogeneous wave equation for the magnetic vector potential $\mathbf{A}$

$$\nabla^2 \mathbf{A} - \mu_0 \epsilon_0 \frac{\partial \mathbf{A}}{\partial t} = -\mu_0 \mathbf{J} \Leftrightarrow \Box^2 \mathbf{A} = -\mu_0 \mathbf{J}. \tag{2.8}$$

In the absence of currents and charges, that means for $\mathbf{J} = 0$ and $\rho = 0$ respectively, this reduces to a homogeneous wave equation. A general solution of which is

$$\mathbf{A} = \mathbf{A}_0 e^{i(\mathbf{k} \cdot \mathbf{r} - \omega t)}, \tag{2.9}$$

a monochromatic plane wave of frequency ω and with wave vector $\mathbf{k}$.

For now, we limit ourselves to the simpler case of linearly polarized plane waves, described by

$$\mathbf{A} = A_0 \cos(kx - \omega t + \varphi)\hat{z}, \tag{2.10}$$

which travel in the x direction. It is straight forward to calculate the corresponding equations for the electric and magnetic field:

$$\mathbf{E} = -\omega A_0 \sin(kx - \omega t + \varphi)\hat{z}, \tag{2.11}$$

$$\mathbf{B} = k A_0 \sin(kx - \omega t + \varphi)\hat{y}. \tag{2.12}$$

By just comparing equations 2.10, 2.11 and 2.12, a simple relation between the amplitudes of the fields can be found with the speed of light given by $c = \frac{1}{\sqrt{\mu_0 \epsilon_0}} = \frac{\omega}{k}$:

$$E_0 = \omega A_0 = c B_0 \tag{2.13}$$

It is important to note that the amplitude of the magnetic field is a factor of c smaller than the amplitude of the electric field. This has important implications on the force acting on a particle with charge q in an electromagnetic field:

$$\mathbf{F} = -q(\mathbf{E} + \mathbf{v} \times \mathbf{B}). \tag{2.14}$$

This so called Lorentz force consists of two parts. One is governed by the electric field and points in its direction. The other one is given by a cross term of the magnetic field with the velocity of the particle and points in propagation direction of the wave. Resulting from the relatively small amplitude of the magnetic field compared to the electric field, this part of the force can be neglected for velocities much smaller than the speed of light. If we consider a single electron, with charge e and mass m_e, in a linearly polarized plane wave given by equation (2.11), the

maximum velocity that the electron will reach within the field with $\mathbf{F} = \frac{\partial \mathbf{p}}{\partial t} = \frac{\partial}{\partial t}(\gamma m_e v)$ is

$$v_{max} = \frac{eA_0}{\gamma m_e} = \frac{a_0}{\gamma}c. \tag{2.15}$$

The dimensionless parameter a_0, called the normalized vector potential, is given by

$$a_0 = \frac{eA_0}{m_e c} = \frac{eE_0}{m_e c \omega} \tag{2.16}$$

and delineates the non-relativistic regime for $a_0 \ll 1$, where the effects of the magnetic field can be neglected, the ultra-relativistic regime for $a_0 \gg 1$, where these effects are dominant and the relativistic regime for $a_0 \approx 1$, where the velocity of the electrons become relativistic and both effects need to be considered. Hence this parameter is widely used to characterize high-intensity laser pulses. In experiments, the value of E_0 is mostly not accessible, but rather the intensity I, which is the average power per unit area, is known. The link between these two quantities can be made by the use of the Poynting vector $\mathbf{S}$, describing the energy flux density transported by the fields [78]:

$$\mathbf{S} = \frac{1}{\mu_0}(\mathbf{E} \times \mathbf{B}) \tag{2.17}$$

The intensity is then given by the time average of the Poynting vector

$$I = \langle S \rangle = \frac{1}{2}c\epsilon_0 E_0^2 \tag{2.18}$$

and hence the normalized vector potential can be written as

$$a_0^2 = \frac{2e^2 I}{m_e^2 c^3 \omega^2 \epsilon_0} = I[\frac{W}{cm^2}]\lambda^2[\mu m^2]/1.37 \cdot 10^{18} \tag{2.19}$$

with the wavelength λ given by $\lambda = 2\pi c/\omega$. The laser pulses used throughout this thesis are in the mildly relativistic regime with a normalized vector potential in the range of $1 < a_0 < 10$. This corresponds to a focused intensity of $2 \cdot 10^{18} \frac{W}{cm^2} < I < 2 \cdot 10^{20} \frac{W}{cm^2}$.

2.2. Laser Plasma Interaction

When laser pulses of such intensities interact with a solid material, the atoms forming this material are ionized and a plasma forms. There are several ways in which this ionization can happen. One way is photo-ionization, where the energy of one incoming photon is transferred to an electron. Thereby, the electron

gains enough energy to overcome the potential barrier, given by the binding energy E_{Ion}, of its atom (compare figure 2.1). The lasers that were used for the
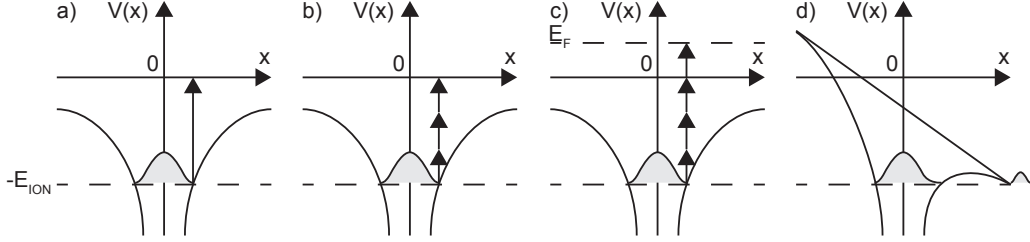

Figure 2.1.: In figure a) a single photon gives enough energy to the electron to directly ionize the atom. In b) multiple photons with energies below the ionization threshold are absorbed. In c) the electron gains excess energy, by absorbing more photons than needed for ionization. In d) the binding Coulomb potential is distorted by the strong external field giving the electron a finite probability to tunnel out of the potential.

experiments in this thesis have a wavelength of $\lambda \approx 800\,nm$, which corresponds to a photon energy of $E_{Ph} \approx 1.55\,eV$. This energy is far below the binding energy of the used target materials. Hence a single laser photon is not sufficient to ionize an atom of the target, and the aggregated energy of several photons is required. This is then called multi-photon ionization where the n-photon ionization rate Γ_n, with the cross-section σ_n, is given by [79]

$$\Gamma_n = \sigma_n I^n \tag{2.20}$$

and becomes significant at intensities $I > 10^{10}\,\frac{W}{cm^2}$. The electron can gain excess energy by absorbing more photons than needed to ionize the atom, giving this process the name above-threshold ionization (ATI). Since this happens in the vicinity of the parent ion, momentum conservation is still fulfilled. The high-intensity laser pulses used in the experiments exert a very strong electric field on the atoms of the target material. This electric field will eventually become so strong that it exceeds the internal electric field the electron experiences within the atom. Taking a classical hydrogen atom as a simple example, the internal electric field E_a the electron feels is given by

$$E_a = \frac{e}{4\pi\epsilon_0 a_B^2} \simeq 5.1 \cdot 10^{11} \frac{V}{m} \tag{2.21}$$

with the Bohr radius, $a_b = \frac{\hbar^2}{m_e e^2}$. From this the atomic intensity [79] can be calculated to be

$$I_a = \frac{1}{2} c \epsilon_0 E_a^2 \simeq 3.5 \cdot 10^{20} \frac{W}{m^2} = 3.5 \cdot 10^{16} \frac{W}{cm^2}. \tag{2.22}$$

A laser intensity $I_L > I_a$ will ionize any material [79]. This is satisfied by the laser intensities used in the experiments discussed throughout this thesis. In fact, since the electron within the atom has to be treated quantum mechanically, ionization will already occur at a fraction of I_a. As soon as the electric field applied by the laser is strong enough to distinctly bend the atomic potential, a substantial probability for the electron to tunnel out of the potential exists (see figure 2.1). This process, named over-the-barrier or barrier suppression ionization, starts to occur for the hydrogen atom at an intensity [79] of

$$I_{app} = \left(\frac{E_a}{16}\right)^2 = \frac{I_a}{256} \simeq 1.4 \cdot 10^{14} \frac{W}{cm^2}. \tag{2.23}$$

The Keldysh parameter,

$$\gamma = \omega_L \sqrt{\frac{E_{Ion}}{I}} \tag{2.24}$$

describes the transition from the multi-photon regime to the tunnelling regime by looking at the point where the external electric field noticeably distorts the atomic potential. Roughly, for a Keldysh parameter $\gamma > 1$ the multi-photon process is dominant, whereas for $\gamma < 1$, the tunnelling process takes over.

All considerations up to now covered free atoms and electrons, and although the situation in a bulk material is far more complex ionization of atoms in the bulk will already start at intensities around $10^{10} \frac{W}{cm^2}$. This corresponds to 8 to 10 orders of magnitude less intensity than the peak intensity of laser pulses used in this work. Thus it is not only important to have knowledge of the temporal structure of the main laser pulse, but also of the pedestal it is sitting on (compare figure 2.2). A pedestal that is too high or contains a pre-pulse, i.e. a small pulse in front of the main pulse, will ionize the target well before the main pulse. The generated plasma then has time to evolve, stretch out into the vacuum and possibly give rise to instabilities. The shape of this so-called pre-plasma strongly influences the interaction of the main laser pulse with the target. Therefore great care has to be taken to control and shape the pedestal of the pulse and the resulting pre-plasma to comply with the experimental needs.

As soon as the laser pulse enters the pre-plasma, it is no longer travelling in vacuum, and therefore the assumption of the absence of currents in section 2.1 is no longer valid. Following the discussion in [80], the ions can be assumed to be stationary, since they are too heavy to follow the fast oscillations with
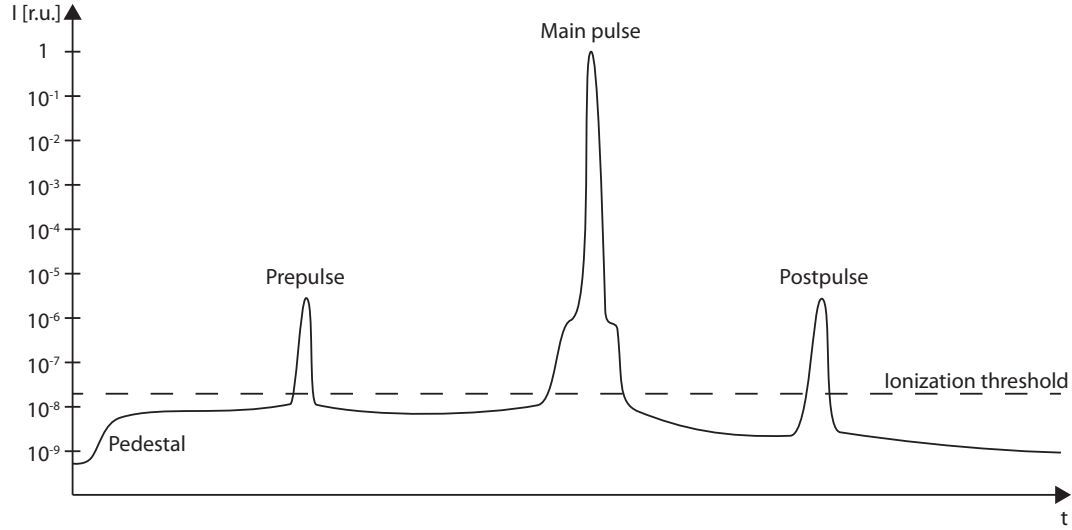
Figure 2.2.: The temporal structure of high-intensity laser pulses may show pre-pulses and pedestals, exceeding the ionization threshold of the target material already well before the main pulse. Thus, plasma formation is triggered, giving the plasma time to evolve and hence alter the interaction of the main pulse with the target.

frequency ω of the electric field. Treating the electrons as a fluid surrounding the ion background and solving their equation of motion leads to the well known dispersion relation for electromagnetic waves in a plasma [80]

$$\omega^2 = \omega_P^2 + k^2 c^2. \tag{2.25}$$

The plasma frequency ω_P is the resonance frequency of the plasma electrons with electron density n_e given by

$$\omega_P = \sqrt{\frac{e^2 n_e}{\epsilon_0 m_e}}. \tag{2.26}$$

For frequencies $\omega < \omega_P$, equation (2.25) shows that k becomes imaginary. Accordingly, ω_P is the minimum frequency for propagation of a light wave in a plasma. A laser pulse entering a plasma gradient can only penetrate up to the point where the condition $\omega = \omega_P$ is fulfilled and is then reflected. The electron density at this point is called critical density, $n_{e,cr}$, and can be calculated with

$$n_{e,cr} = \frac{\omega^2 \epsilon_0 m_e}{e^2}. \tag{2.27}$$

The maximum reachable electron density of a certain material can be calculated by

$$n_e = \rho \frac{\sum\limits_i N_{e,i}}{\sum\limits_i \rho_{u,i}} N_A, \tag{2.28}$$

given its density ρ, the number of electrons per atomic species $N_{e,i}$, and their respective molar weights, $\rho_{u,i}$, with the Avogadro constant N_A. The target material used throughout this thesis is fused silica. It consists of SiO_2 and has a density of $2.2 \frac{g}{cm}$. Hence the maximum electron density is

$$n_{e,SiO_2} = \rho_{SiO2} \frac{N_{e,Si} + 2 \cdot N_{e,O}}{\rho_{u,Si} + 2 \cdot \rho_{u,O}} N_A =$$

$$= 2.2 \frac{g}{cm^3} \frac{14 + 16}{(28 + 32)\frac{g}{mol}} 6 \cdot 10^{23} \frac{1}{mol} \simeq 6.6 \cdot 10^{23} \frac{1}{cm^3} \tag{2.29}$$

Comparing this value to the critical density of an electromagnetic wave with a wavelength of $\lambda = 800 \ nm$, corresponding to the wavelength of a Ti:Sapphire laser, a density ratio of $n_{e,SiO_2} \simeq 380 n_{e,cr,800nm}$ is obtained from equation (2.27). This has important implications for the interaction of this material with a laser pulse. For pulse intensities in the region of $10^{18} - 10^{20} \frac{W}{cm^2}$, the surface of a target will be fully ionized, and even for a perfect Gaussian pulse, the ionization will start well before the main peak of the pulse. The laser pulse will therefore not reach the target surface but will, as described before, be reflected at the so-called critical surface with $n_e(x) = n_{e,cr}$ within the pre-plasma.

On its way through the plasma the laser pulse will loose energy to the plasma due to various absorption processes. Two especially important mechanisms for the scope of this thesis are resonance absorption and Brunel absorption. Both require the laser pulse to be p-polarized, i.e. the electric field component oscillates in the plane spanned by the wave vector and the normal to the reflecting surface, and obliquely incident on the plasma gradient resulting in a component of the electric field that points along the density gradient, i.e. $\mathbf{E} \cdot \nabla n_e \neq 0$. In the case of resonance absorption this component sets up charge oscillations in form of electrostatic waves at $\omega(x) = \omega_p(x)$. Due to resonance conditions the component of $\mathbf{E}$ along the gradient is greatly enhanced. This mode conversion leads to a transfer of electro-magnetic energy to electro-static energy the subsequent dissipation of which leads to resonance absorption [80]. For Brunel absorption, which is an essential part of the coherent wake emission mechanism discussed in section 3.1, the electric field accelerates electrons out of the plasma during one half-cycle and pulls them back into the plasma during the following cycle, where they deposit their energy and simultaneously trigger plasma waves in their wake [81].

3. Generation of Attosecond Pulses from Solid Surfaces

Building on the basic concepts of laser plasma interactions, this chapter focuses on the generation of high-order harmonics in laser-irradiated solid-density plasmas. The observation of high-order harmonics of the fundamental laser frequency in the spectral domain is, as can be seen by a simple Fourier transform, connected to the periodic occurrence of bunches of light in the temporal domain. Two mechanisms are presently known to lead to the generation of short light pulses in the interaction of a laser pulse with a dense plasma. One is called Coherent Wake Emission (CWE), while the other is referred to as the Relativistically Oscillating Mirror (ROM). While the ROM-process, as can be deduced from the name, requires the intensity of the laser pulse to be well above the relativistic limit, i.e. $a_0 > 1$, CWE takes also place at moderate laser intensities. In this chapter, the basic concepts and selected properties of these mechanisms which are important for the understanding of the following chapters are discussed. A detailed overview over the evolution of this field can be found in the thesis of Y. Nomura [70], and in-depth reviews can be found in references [71, 72].

3.1. Coherent Wake Emission

The first observations of high-order harmonics of the initial laser frequencies generated on solid-density plasmas have already been made in the late seventies and early eighties of the last century [67–69], but the explanation for these findings was only given at the beginning of this century [82, 83]. The recorded harmonic spectra have some interesting features in common. They show a very sharp cut-off at a frequency which depends on the target material [49, 84–87]. The harmonic generation works best for p-polarized incoming pulses, resulting in harmonics that are also p-polarized [67], whereas the efficiency is lowered by at least 3 orders of magnitude for s-polarization [88, 89]. The measured conversion efficiencies, of incoming laser energy into energy within the harmonic spectrum, for the generation process are in the high 10^{-5} range [49, 70].

The underlying mechanism of the CWE harmonic emission is closely related to the Brunel absorption described in section 2.2. The component of the impinging electric field parallel to the plasma density gradient, i.e. parallel to the target

normal, accelerates electrons out of the plasma during one half-cycle. The electrons that start first will feel a bigger portion of the electric field and hence will reach higher velocities and have longer excursions than the electrons launched at the very end of the half-cycle. In the next half-cycle, when the electric field has changed its sign, the electrons are hurled back inside the plasma gradient. Since the plasma can be regarded as a perfect conductor, the electrons feel no field after entering and hence move with a constant velocity. Thus the electrons with a higher velocity will, at some point, overtake the slower ones and an electron bunch will form (see figure 3.1). This bunch then triggers plasma waves in
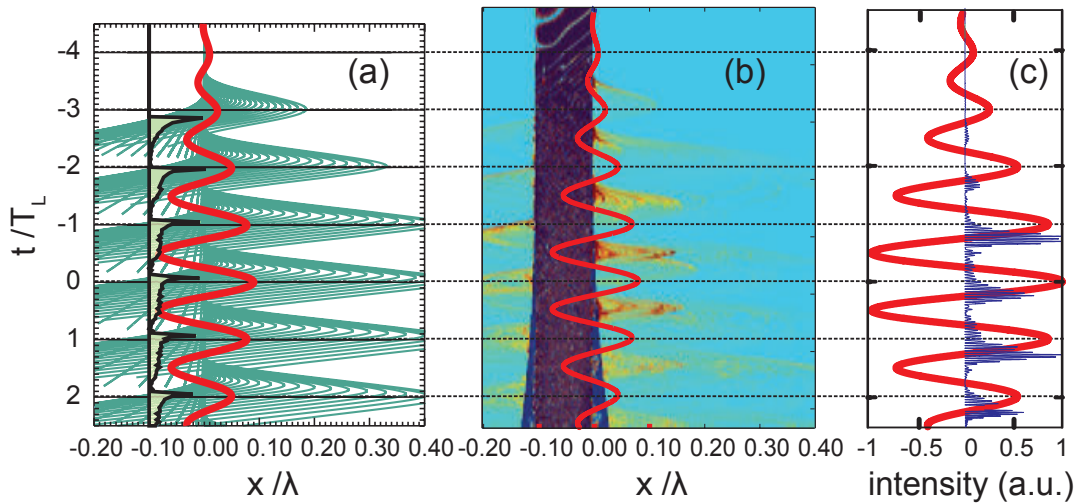
Figure 3.1.: Electron trajectories (green), driven by the electric field of a short laser pulse (red), derived by model calculations in (a) show the formation of electron bunches (black line green filled), unequally spaced in time, at a depth of $x = -0.1\lambda$ within the plasma by overtaking of slow electrons with small trajectories by faster electrons with longer trajectories. The electron density evolution obtained by 1-D-PIC simulations in (b) shows a very similar behaviour and the generated attosecond pulses shown in (c) (blue) temporarily coincide with the return of the expelled electrons.

the density gradient, which by undergoing linear mode conversion [90, 91], can again emit electromagnetic radiation. Due to phase matching conditions of the linear mode conversion, the electromagnetic radiation will be released in a short light pulse, confined to less than an optical cycle. The stimulated plasma waves have, as described previously, specific frequencies depending on the local plasma density $\omega_P(x) \propto \sqrt{n_e(x)}$ (see figure 3.2). This immediately introduces a relative delay, i.e a chirp, between the individual emitted frequencies [83] and accordingly an elongation of the emitted light pulse [87]. The whole process will be repeated once every laser cycle, leading to a train of short pulses, each with a continuous spectrum. Using a spectrometer to look at the time averaged spectrum of this
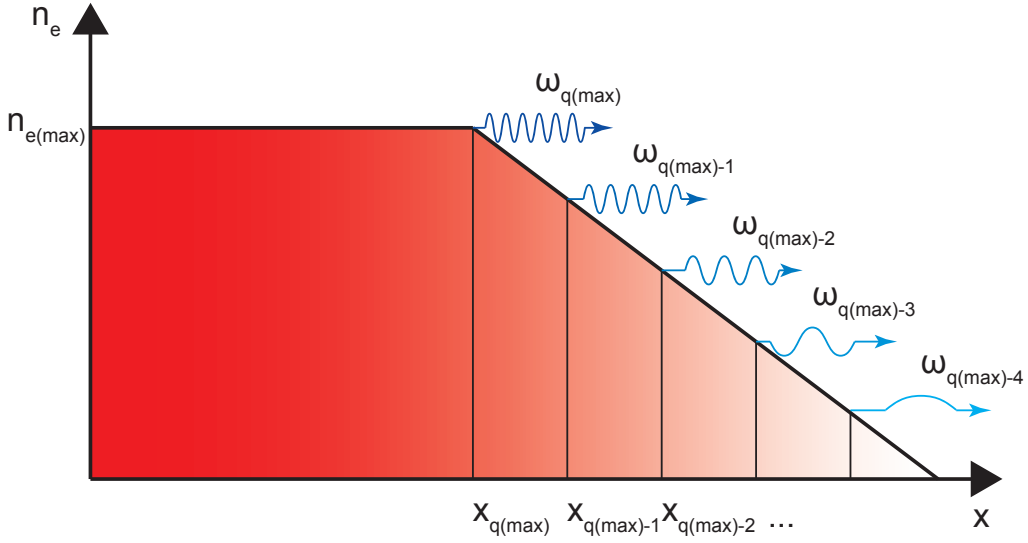
Figure 3.2.: The plasma in the gradient radiates at its local resonance frequency. This leads to a chirp between the individual components of the emitted spectrum due to the different path lengths within the gradient and a sharp spectral cut-off at the plasma frequency corresponding to the bulk density.

train reveals a spectrum of harmonics of the fundamental laser frequency due to constructive and destructive interference of the individual spectra. Nomura et al. [49, 70, 92] experimentally demonstrated this generation of a train of pulses by doing a second-order volume auto-correlation measurement. They were able to show the lengthening of the pulses by analysing the envelope of the individual peaks.

Another very important implication of the high-harmonic generation mechanism by plasma waves is the occurrence of a defined cut-off frequency in the emitted spectra (see figure 3.2). This cut-off solely depends on the maximum plasma frequency and is therefore directly related to the target material [49, 84–87]. The highest harmonic order q_{CO} that the plasma can sustain can then be calculated as

$$q_{CO} \leq \sqrt{\frac{n_{max}}{n_c}}. \tag{3.1}$$

Using again fused silica as an example, one can reach harmonics up to a cut-off at $q_{CO} \lesssim 20$ as can be seen in figure 3.3.

Besides the chirp coming from the different emission depths of different frequencies, the so-called atto-chirp, there is a second chirp term, the so-called harmonic-chirp, leading to phase fluctuations within the single harmonics. As described above, the generation of the light pulses goes hand-in-hand with the
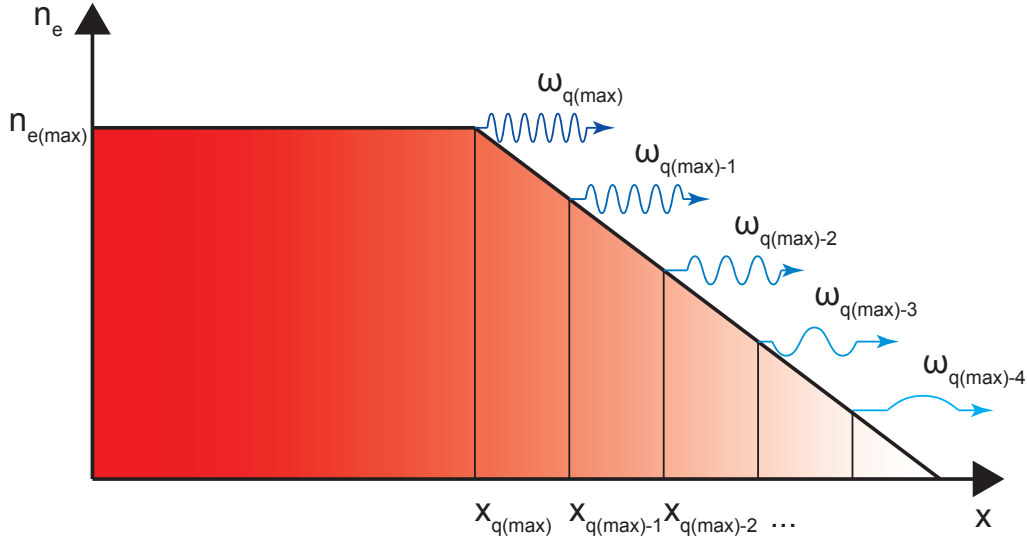
Figure 3.2.: The plasma in the gradient radiates at its local resonance frequency. This leads to a chirp between the individual components of the emitted spectrum due to the different path lengths within the gradient and a sharp spectral cut-off at the plasma frequency corresponding to the bulk density.

train reveals a spectrum of harmonics of the fundamental laser frequency due to constructive and destructive interference of the individual spectra. Nomura et al. [49, 70, 92] experimentally demonstrated this generation of a train of pulses by doing a second-order volume auto-correlation measurement. They were able to show the lengthening of the pulses by analysing the envelope of the individual peaks.

Another very important implication of the high-harmonic generation mechanism by plasma waves is the occurrence of a defined cut-off frequency in the emitted spectra (see figure 3.2). This cut-off solely depends on the maximum plasma frequency and is therefore directly related to the target material [49, 84–87]. The highest harmonic order q_{CO} that the plasma can sustain can then be calculated as

$$q_{CO} \leq \sqrt{\frac{n_{max}}{n_c}}. \tag{3.1}$$

Using again fused silica as an example, one can reach harmonics up to a cut-off at $q_{CO} \lesssim 20$ as can be seen in figure 3.3.

Besides the chirp coming from the different emission depths of different frequencies, the so-called atto-chirp, there is a second chirp term, the so-called harmonic-chirp, leading to phase fluctuations within the single harmonics. As described above, the generation of the light pulses goes hand-in-hand with the
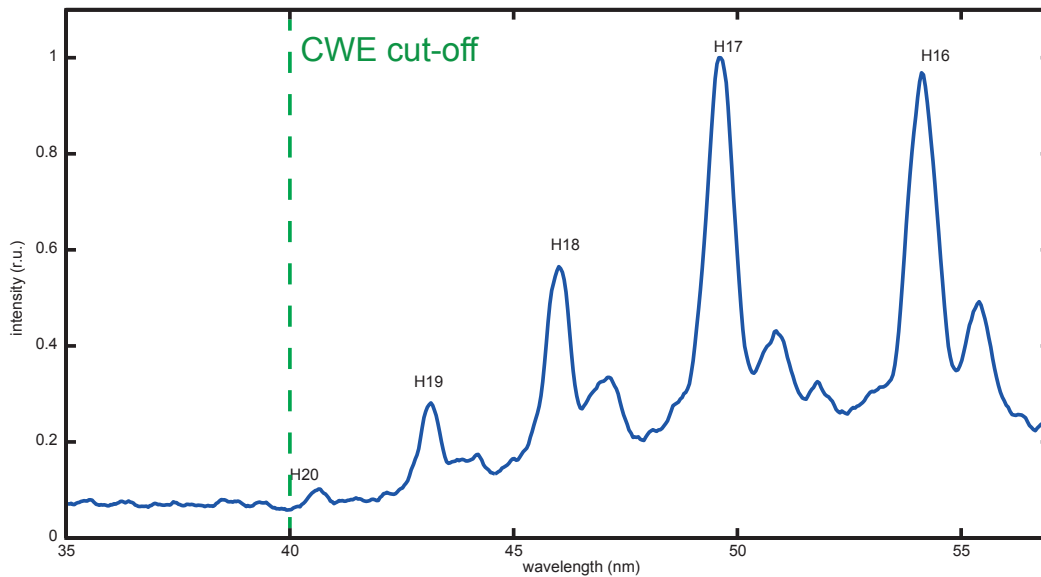
Figure 3.3.: A spectrum showing CWE harmonics generated with a 3-cycle driving laser. The spectrum shows harmonics with side peaks caused by the unequal spacing of the emission time of the attosecond pulses and a distinct cut-off defined by the used target material (fused silica).

occurrence of electron bunches within the plasma. The relative timing of these bunches now depends on the instantaneous intensity of the laser pulse [93]. The electrons have longer excursion times for higher laser intensities [94]. At the rising edge of the pulse the excursion times increase and then on the falling edge, they decrease again. The relative emission times of the light pulses are hence changed by fractions of an optical cycle of the driving laser pulse, where the relative distance is increasing at the beginning and then decreasing at the end of the pulse. This unequal spacing of the light pulses can be observed in the harmonic spectra. Since the harmonics are formed by constructive and destructive interference of the coherently overlapped spectra, a deviation from perfect periodic emission times will lead to distortions in the harmonic spectra due to the introduced phase differences. These distortions lead to effects ranging from simple broadening of the harmonics to the introduction of new peaks in the spectrum. Selected examples are shown in figure 3.5. Chirping the driving laser pulse can counteract these effects. Applying the right amount of positive chirp will generate equally spaced electron bunches and hence nicely shaped harmonics. In contrast, applying a negative chirp will further intensify the modulation of the spectra [83, 89]. This effect is more pronounced for harmonics generated by very short driving laser pulses, i.e. with durations of only a few optical cycles [89]. In these laser pulses, the relative change in intensity from one cycle to the next

is much bigger than in long laser pulses, introducing stronger deviations in the timing of neighbouring bunches. To address this behaviour more quantitatively a model based on the Brunel absorption [81] and the Corkum three-step model for high harmonic generation in an atomic medium [25] was developed.

Following the formulation of Brunel [81], the electron dynamics can be described in a simplified fashion by a one-dimensional equation of motion along the x-axis, parallel to the target normal, where x=0 at the plasma-vacuum boundary. In the relativistically correct form, the electronic motion in the combined electric field of the laser and the electrostatic field due to space charge accumulation is described by:

$$\frac{d\beta}{dt} = 4\pi \sin(\Theta) a_0 (1 - \beta^2)^{\frac{3}{2}} \cdot$$
$$\cdot \left[E_L(t + t_0) \cos(\omega_L(t + t_0 + \phi)) - E_L(t_0) \cos(\omega_L(t_0 + \phi)) \right] \tag{3.2}$$

Here β is defined by $\beta = \frac{dx}{dt}$ and x is the distance from the plasma vacuum interface. The temporal envelope of the electric field of the laser is given by $E_L(t) = e^{(-t^2)/(0.72\tau_L^2)}$ with the emission time of the electron t_0 and the pulse duration τ_L. Θ is the angle of incidence of the laser on the plasma. The time is normalized to periods of the laser electric field T_L, hence $\omega_L = 2\pi$. Space is given in units of the laser wavelength λ_L and the carrier envelope phase ϕ is normalized to 2π. The last term of equation (3.2) describes the space charge at the instant of time when the electron is released. Since the bulk plasma can be regarded as a grounded perfect conductor, the space charge term is constant over time. Although this formula is relativistically correct, the influence of the magnetic field is neglected. This is valid up to mildly relativistic intensities. Equation 3.2 can be solved numerically, and a solution for $a_L = 1.5$, $\tau_L = 3$ and $\Theta = 45°$ is shown in figure 3.1 a). In this figure one can see trajectories of electrons emitted from the plasma at different times during the laser cycles. Only trajectories of electrons that return to the plasma are plotted. The excursion length varies clearly with the emission time, and the electrons pulled out at the beginning of the respective circle show longer trajectories. In the histogram of electrons per unit time crossing a certain depth within the plasma, clear temporal bunching of the electrons can be observed.

A comparison to results of a 1D simulation using the PIC code PICWIG [95] can further substantiate the validity of this model. The input parameters of the simulation are chosen to resemble real world experiments with $a_0 = 1.5$, $\Theta = 45°$, $\frac{n_e}{n_c} = 400$ and a linear density ramp with a scale length of $L = 0.2\lambda_L$. The electron trajectories that are gained from the simulation and shown in figure 3.1 b) are very similar to the ones from the model. The PIC simulation not only give the trajectories of the electrons, but also the emitted electromagnetic waves of the plasma. Taking the spectrum of these waves, filtering out everything but the

spectral region spanning from the 10th to the 20th harmonic and then inverse Fourier transforming the resulting spectrum into the temporal domain results in a train of pulses with durations on the scale of some hundred attoseconds, as shown in figure 3.1 c). The timing of these attosecond pulses almost perfectly mimics the timing of the electron bunches determined from the model calculations.

This very good agreement of the simulation with the model allows for further analysis of the results of the numerical solution, similar to the analysis done in reference [93]. In figure 3.1 the unequal spacing of the electron bunches is obvious. The distance between the individual bunches monotonically increases with time. The time difference Δt_n between the nth positive-to-negative crossing of the electric field and the resulting electron bunch first decreases on the rising edge of the pulse and then increases again on the falling edge. In figure 3.4 this is shown for two cases, a 15- and a three-cycle pulse. These data points follow very closely a $\Delta t_n(t, \phi) = A|\frac{t-(\phi-\phi_0)}{\tau_L}|^p + B$ dependency with the fitting parameters A, B, ϕ_0 and p. p is found to be weakly dependent on τ_L, but for the two cases here to a good approximation equal to 3. Under the assumption that the emitted spectrum $E_A(\omega)$ of a single electron bunch is constant over the spectral range of interest and equal for each individual electron bunch in the train, it is possible to calculate the resulting spectrum of the train $E_T(\omega)$ with

$$E_T(\omega) = E_A(\omega) \sum_n E_L(t_n)e^{i\omega t_n}. \tag{3.3}$$

According to the model, the time of occurrence of the nth attosecond pulse is given by $t_n = \Delta t_n(n, \phi) + n - (\phi - \phi_0)$. The spectra for the two pulse lengths under consideration are given in figure 3.4. While the long laser pulse shows a spectrum of clean harmonics, the harmonics of the short driving pulse exhibit strong modulations. The effect of the unequal spacing is much stronger for the short pulse, since the change in the instantaneous intensity from one cycle to the next is much larger here than for the long pulse. Hence the change in excursion and the time of bunch formation is altered in a much stronger way from cycle-to-cycle than for a long driving laser pulse. Figure 3.4 also shows the relative timing of the bunches for 3 different values of the carrier envelope phase of the driving laser pulse. As expected, the generation of the electron bunches shifts with the electric field under the envelope. This change in relative timing leads to different spectral features for different values of the CEP. This effect can be observed in PIC simulations, model calculations and in experiments with short driving pulses. Examples are shown in figure 3.5. Independently, this has been confirmed by recent measurements with phase stable, high repetition rate driving lasers with very short pulse durations [96, 97].

Given that the plasma oscillations are responsible for the emission of the at-tosecond pulses, it is evident, that changes in the extent or shape of the pre-
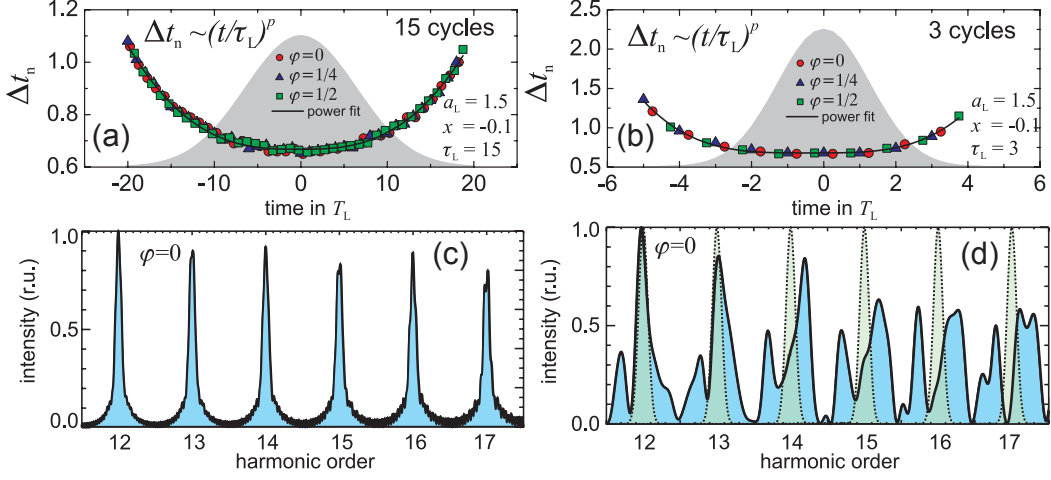
Figure 3.4.: The time difference between the nth positive to negative crossing of the electric field of the driving laser pulse and the formation of the electron bunch within the plasma gradient is shown for three different CEP values for a driving laser pulse duration of 15 cycles in a) and 3 cycles in b). The intensity envelope of the laser pulses is given as a reference (grey shaded area). Corresponding spectra for the two pulse durations are given in c) and d) for a CEP value of $\varphi = 0$, an additional spectrum for equally spaced pulses is given in d) for comparison.

plasma will alter the emitted radiation. Földes et al. [98] and Zepf et al. [88] investigated the influence of the pre-plasma scale length L on the harmonic conversion efficiency η. A $\eta \sim e^{-\frac{L}{l_q}}$ dependency has been shown by Zepf et al. [88], with a length l_q which depends on the harmonic order q. By shaping the pre-plasma appropriately, spectral features can be enhanced or suppressed [99]. At the same time, the harmonic spectra can be used as a tool for plasma diagnostics [93, 100], for example, in inertial confined fusion experiments.

3.2. Relativistically Oscillating Mirror

In contrast to the CWE mechanism, the underlying process of the relativistically oscillating mirror (ROM) mechanism, i.e., the Doppler upshift of radiation by the reflection off a mirror moving with relativistic velocity, has already been described by A. Einstein in one of his annus mirabilis papers in 1905 [101]. The difference to this description is that the reflection does not happen on a perfect mirror, flying freely at a constant speed, but on an electron sheet being forced to an oscillatory motion by the same electromagnetic wave that is reflected off it. This has some important implications on the boundary conditions of this process
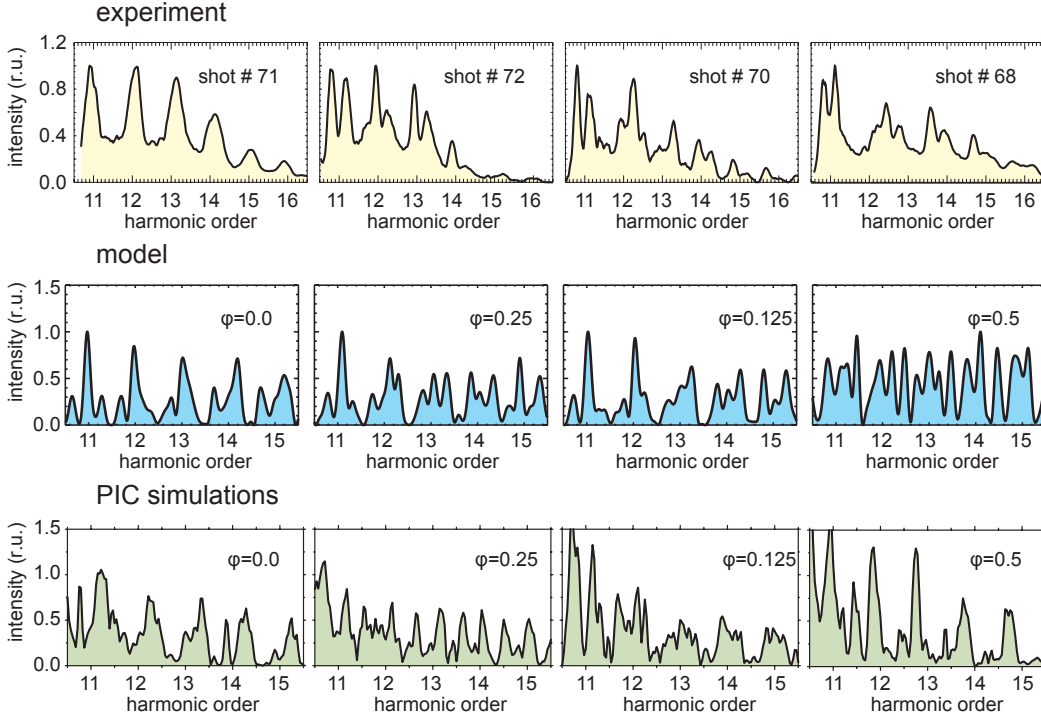
Figure 3.5.: Comparison of experimentally obtained spectra with results from model calculations and 1-D-PIC simulations for a 3-cycle driver laser. For the experimental spectra all controllable laser parameters were kept constant, leaving the CEP as the only free variable. Although no clear one to one correlation of the CEP values can be made, very similar spectral structures in all three subsets can be found.

[102]. A first description of the process has been given by Bulanov et al. in 1994 [103]. Since then it has been profoundly studied theoretically and numerically [66, 95, 102, 104–120] as well as experimentally [75, 87, 100, 121–130].

A simplistic oscillating mirror model for normal incidence is given by Tsakiris et al. [66]. Due to its simplicity, it gives a vivid picture of the process, but at the same time, it reproduces the properties of more evolved models and experiments very well. Therefore, this model will be briefly introduced and is schematically shown in figure 3.6. A relativistically intense electromagnetic wave, $E(t) \propto \sin(\omega_L t)$ passes an observer at time t and hits a step like plasma vacuum interface at a distance R at a later time t'. There, it drives an oscillatory motion of the electrons around the plasma vacuum interface. Due to the normal incidence, the force applied to the electrons by the laser is only the $\mathbf{v} \times \mathbf{B}$ part of the Lorenz force, oscillating with twice the laser frequency, and a restoring force builds up between the immobile ions and the moving electrons. The accurate time dependent deflection of the electron layer $X_m(t')$ can be very complex
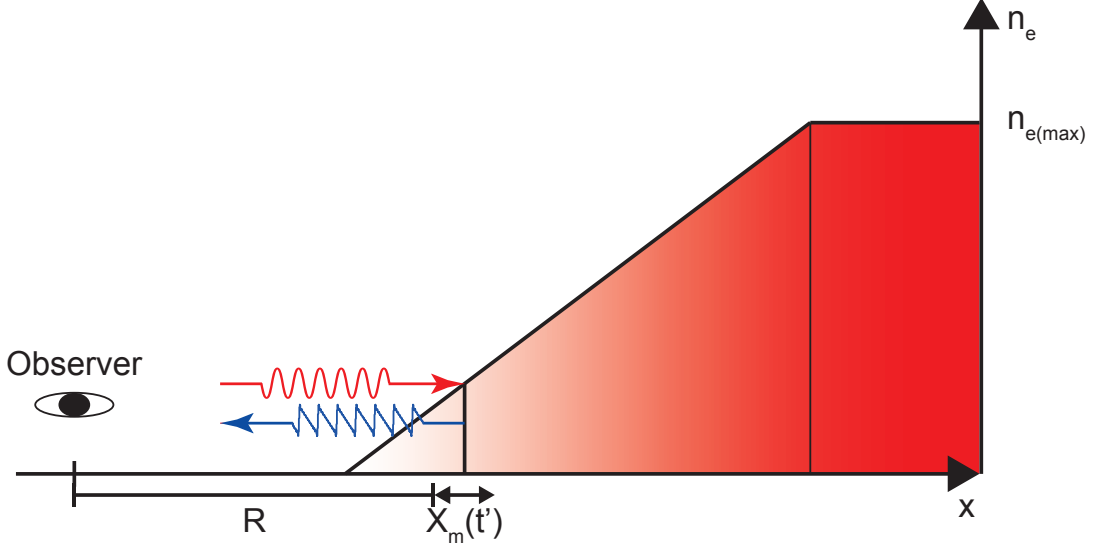
Figure 3.6.: Illustration of the oscillating mirror model. The incident electric field of the laser is reflected off an oscillating layer of electrons. The phase of the reflected field seen by the observer depends on the position of this layer at the time of reflection. These phase distortions lead to a strong harmonic content in the reflected field.

due to the complicated interplay of the forces within the plasma. But as Baeva, Gordienko and Pukhov show in their so-called BGP-model [107], the emitted harmonic spectrum shows universal features that are independent of the exact form of the function $X_m(t')$. Hence, a reasonable simplification is that the motion of the electrons closely follows the $\mathbf{v} \times \mathbf{B}$ force, with a phase shift ϕ_m and a time dependent amplitude $A_m = \frac{\lambda_L}{4\pi} \frac{a_0}{\sqrt{1+a_0^2}}$ [66]. The time of arrival of the laser pulse at the oscillating surface is then given by:

$$t' = t + \frac{R + X_m(t')}{c} \tag{3.4}$$

with the function for the motion

$$X_m(t') = \frac{\lambda_L}{4\pi} \frac{a_0}{\sqrt{1 + a_0^2}} \sin(2\omega_L t' + \phi_m). \tag{3.5}$$

By solving this implicit function for t', it is possible to calculate the reflected field $E_{ref}(t) \propto \sin(\omega_L t + 2k_L X(t'))$ seen by the observer at time $t + 2(t' - t)$, omitting the constant phase terms $2k_L R$ and ϕ_m. Since the laser is reflected by a moving surface, its frequency is shifted by the doppler effect. The important quantity for the shift is the maximum velocity v_{max} of the reflecting object, which

in the relativistic case, is mostly given in terms of the relativistic gamma factor $\gamma_{max} = \frac{1}{\sqrt{1-v_{max}/c}} = \sqrt{1 + a_0^2}$. Figure 3.7a) shows the motion of the mirror for $a_0 = 10$ in its own as well as in the lasers reference frame. It can be seen that in the laser frame, the motion is no longer sinusoidal but quasi-triangular with a sharp rise that is compressed by a factor of $4\gamma_{max}^2$ [66] when the laser and the mirror are counter-propagating. These sharp edges correspond to spikes in the velocity of the mirror motion and are predicted by more advanced models [107]. At these spikes, the highest upshift of the laser frequency occurs, resulting in the emission of ultra short pulses of light in the atto- or even zeptosecond regime. These pulses are separated by half a laser cycle, leading to the emission of only odd harmonics in frequency space (see figure 3.7 c)). The overall emitted spectrum shows a power law roll-off $I \propto \omega^q$ with $q = -\frac{5}{2}$ up to a cut-off harmonic $n_{co} = \frac{\sqrt{1+a_0^2}+a_0}{\sqrt{1+a_0^2}-a_0}$, which for $a_0 \gg 1$ goes to $n_{co} \approx 4\gamma_{max}^2$. Beyond this harmonic number, an exponential decay of the spectrum can be observed. This cut-off corresponds exactly to the expected value from Einstein's theory [101], whereas the more refined model of Baeva et al. [107] provides some corrections. This model predicts a power law decay of the spectrum with $q = -\frac{8}{3}$ which first starts to deviate from the power law behaviour at $n_{co} \approx 4\gamma_{max}^2$ and then at $n \propto \sqrt{8}\gamma_{max}^3$, decays exponentially. Both the cut-off at $n \propto \sqrt{8}\gamma_{max}^3$ and the $I \propto \omega^{-\frac{8}{3}}$ scaling have also been validated experimentally [123, 124], but numerical simulations show deviations of this universal spectrum for certain laser and plasma parameters [117–120]. A peculiar feature of the spectra produced by the simple model discussed above is the appearance of only odd harmonics (see figure 3.7). This stems from the normal incidence, and in which case, the only driving force of the mirror surface is the $\mathbf{v} \times \mathbf{B}$ term of the Lorentz force with its 2ω periodicity. A simple adaptation to oblique incidence, where the mirror surface is allowed to be moved by the electric field of the laser with a 1ω periodicity, will immediately show the emission of odd as well as even harmonics. This change of harmonic spectrum with the angle of incidence is a simple example for selection rules of the ROM process. More of these rules, for example for different incident laser polarizations, have been studied by R. Lichters [116, 131]. One flaw of the ROM-models is the lack of an explanation for the emission of relativistic harmonics in forward direction in thin-foil experiments and simulations [100, 132, 133]. New, refined mirror models [134, 135], adapted doppler upshift models, looking closely at the generated non-linear currents within the plasma [132] and single particle pictures dealing with the emission of synchrotron radiation of accelerated electrons [115, 136] can explain this behaviour.

The relativistic harmonics generated in reflection off of solid-density targets have some properties that are superior to the harmonics generated by the CWE mechanism. One of these properties is the strong temporal as well as spatial
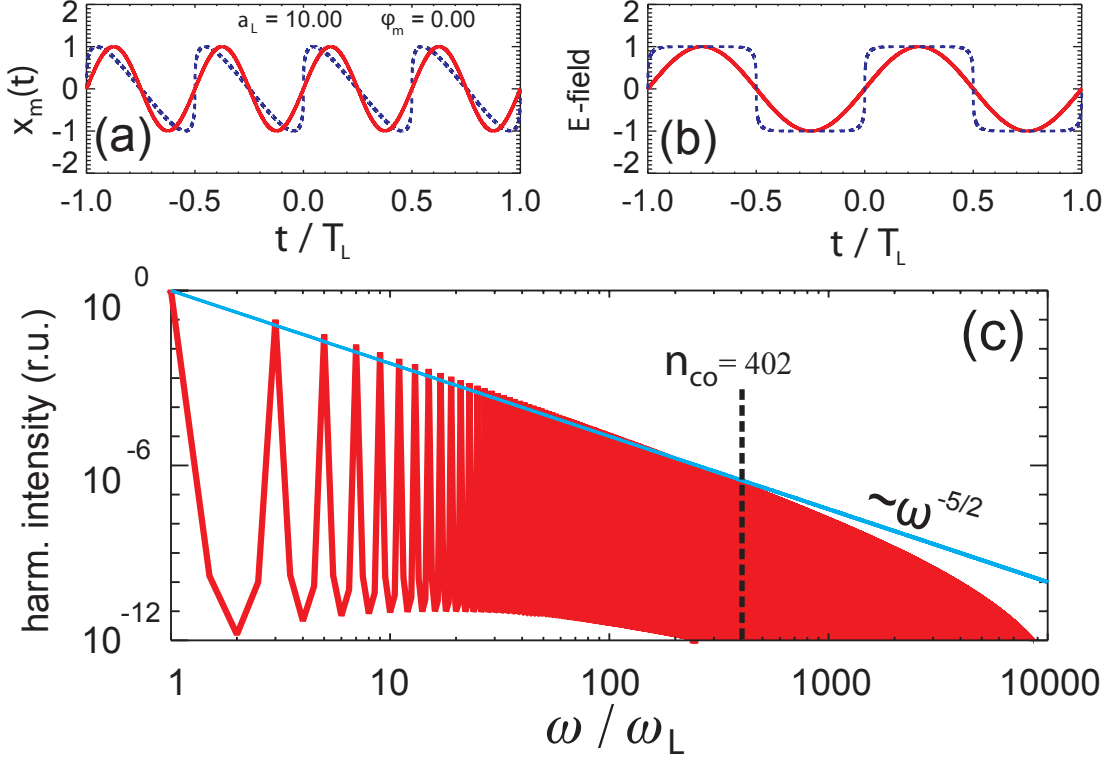
Figure 3.7.: Results of the oscillating mirror model for $a_L = 10$, taken from [66]. (a) Mirror motion in the frame of the mirror (——) and the frame of the laser (– – – –). (b) Electric field before (——) and after (– – – –) reflection of the mirror in the frame of the observer. (c) A Fourier transform of the reflected field results in a spectrum closely following the predicted power law $1/\omega^q$ with a $q \approx 5/2$ roll-off.

confinement of the generation of the upshifted frequencies within one cycle of the driving field. According to the BGP-Model [107], the reflection of the laser occurs mainly during the so-called gamma spikes of the reflecting electron layer, which are the instants of time where the reflecting surface reaches its maximum velocity. Due to this strong confinement, there is no intrinsic phase between the emitted frequencies, and the formation of unchirped ultrashort pulses is feasible. Another superior feature of the ROM process is the higher conversion efficiency of laser light into short wavelength radiation. Efficiencies larger than 10^{-2} are predicted numerically for harmonics in the regime of some $10 eV$ and are still larger than 10^{-5} around $1 keV$ [66, 72, 107]. These have also been confirmed experimentally [124]. Various parameters, e.g., the laser intensity, length of the pre-plasma or angle of incidence, strongly influence the efficiency of the process. Also, with higher intensities, the conversion efficiency into a specific spectral region increases [66, 72]. Teubner et al. [130] report on a $I^3 - I^4$ scaling for single harmonics

with the incoming intensity. But beyond a certain intensity, depending on the chosen energy range, saturation sets in [66]. Especially the length and shape of the pre-plasma have severe impact on the generated spectrum. A very short pre-plasma will reduce the conversion efficiency [72]. This can be understood by a simple argument. For a short pre-plasma gradient, it is harder for the laser to move the reflecting surface, since the surrounding plasma is more dense than in a longer gradient. The optimum length of the gradient depends on the intensity of the laser pulse and also its duration, since a long laser pulse can compress the pre-plasma by the ponderomotive force. But also, gradients that are too long are not preferable, since the plasma surface can become unstable and start to ripple [113, 137, 138]. The incoming laser then no longer interacts with a smooth and clean electron layer, but with a chaotic and rough plasma cloud. Hence the selection rules for the incoming laser polarization no longer fully apply, since various angles of incidence are formed, and accordingly, the reflection is not a well collimated beam any more but is scattered into all directions [121, 137, 139]. Small degrees of surface roughness will be cleaned by the interaction [125], and the reflected harmonic beam will then have an even smaller divergence than expected due to the denting of the reflecting surface by the light pressure of the incoming laser and the corresponding focusing of the reflected radiation [87, 125]. Here the intensity of the focused radiation can be high enough to reach the Schwinger limit [140] due to the small exponent of the power law decay [87, 104, 125]. The light pressure also leads to a net movement of the reflecting surface during the interaction. This movement reveals itself in the generated harmonic spectrum. Since the points of generation of the upshifted radiation in the individual cycles will not coincide when the reflecting surface is not moving perfectly periodically, a net phase shift between the respective spectra will occur, similar to the case of unequal spacing in the CWE mechanism. This phase shift manifests itself in a modulation of the observed harmonic spectra. Depending on the velocity of the movement of the oscillating surface, this can lead to everything from a slow modulation of the spectrum [117, 128] to a fast disturbance [127]. These spectral features can then be used to gain deeper insight into the motion of the reflecting plasma layer and therefore also into the details of the laser-plasma interaction.

3.3. Single Attosecond Pulse Generation

In the previous two sections, the mechanisms leading to and properties of trains of attosecond pulses generated by the interaction of a high-intensity laser pulse with an overdense plasma have been described in detail. The question now arises how to isolate a single pulse out of these trains which then can be used for time resolved measurements with unprecedented resolution. In general, there are two

possibilities to achieve this goal: either to confine the emission to a single cycle of the laser pulse, or to separate a single pulse out of the train after the generation.

The splitting-off of a single pulse out of a train is very challenging since there are no mechanical or electrical shutters that are fast enough. A solution to this problem is presented by Vincenti and Quéré [141] who propose to use spatio-temporal coupling [142] of the driving laser pulses to separate the individual pulses within the train geometrically. Their idea is to introduce a certain amount of pulsefront tilt, i.e., a tilt of the pulsefront against the phasefront of the laser pulse [143], into the driving laser beam, which will lead to a rotation of the wavefront in the focus of the laser (see figure 3.8). This rotation can be understood as a time dependent variation of the angle of incidence of the laser and hence leads to the emission of the individual pulses into different directions (see figure 3.8). By matching the amount of pulsefront tilt to the length of the laser pulse, geometrically well separated pulses can be achieved, and further cleaning can be done by applying apertures at the right distances [141].
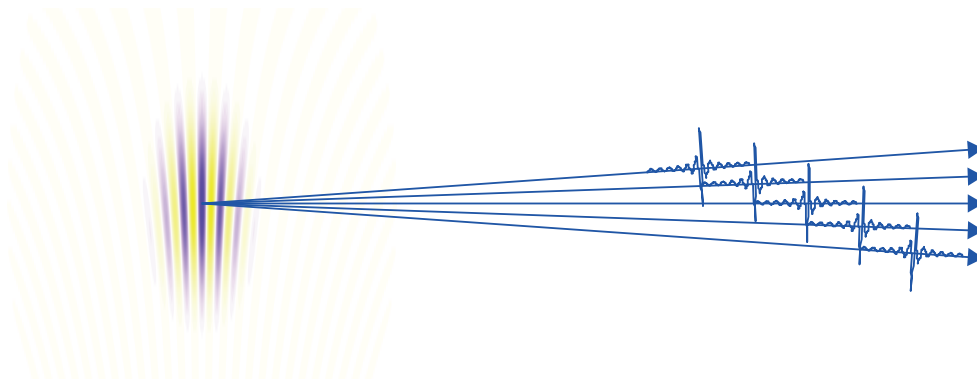

Figure 3.8.: A spatial chirp on the driving laser field (yellow-purple) manifests itself in a rotating electric field in the focus. This leads to a change in the effective angle of incidence over time and hence an emission of the single attosecond pulses (blue) of the train into different solid angles.

The second method to create a single pulse is to already confine the emission to only one cycle of the driving laser field. This can be done by either using a long driving laser pulse and applying a suitable gating technique to suppress the emission of all but one cycle or by directly using a pulse which is short enough. The most prominent implementation of the gating approaches is the polarization gating technique [38, 95, 144]. Out of two replicas of the pulse, a new pulse with varying polarization is synthesized. The polarization is selected in such a way, that the pulse is circularly polarized at the beginning and at the end, but has a single linearly polarized cycle in the centre. Using such a pulse as a driver for relativistic harmonics of solid surfaces, the emission of the harmonics is greatly suppressed during the circularly polarized parts and has a substantial

contribution only during the single linearly polarized cycle [95]. The need for such a technique, which wastes most of the pulse energy, can be circumvented by direct use of few-cycle laser pulses as a driver. The problem here is that the production of few-cycle laser pulses with relativistic intensities is a not a simple task from many points of view. Appropriate active laser materials and optics which support a very broad bandwidth and at the same time withstand the high intensities are necessary. Nevertheless, first systems based on optical parametric chirped-pulse amplification (OPCPA) technology are already available [73, 145] or are in the state of being commissioned [146, 147]. Compared to harmonics from gases, the harmonic emission from solid surfaces relaxes the demands on the laser pulse duration since the harmonic emission happens only once per cycle. The ROM harmonic process is further alleviating this condition due to the higher degree of non-linearity of this process. This non-linearity α is defined with $I_{harm} \propto I_{Laser}^{\alpha}$ as the exponent connecting the intensity of the laser to the emitted XUV-radiation. Teubner et al. [130] show that the degree of non-linearity for the ROM-process with an $\alpha \approx 3 - 4$ is higher than for the CWE-process with $\alpha \approx 1 - 2$. Assuming that this also holds for the instantaneous intensity within the pulse envelope of the driving laser, the high non-linearity effectively shortens the envelope of the XUV-emission.

The question now arises, how short a laser pulse needs to be in order to generate only a single attosecond pulse by the ROM-mechanism. A crucial parameter for the interaction with these short laser pulses is the CEP. This phase describes the absolute positioning of the electric field under the envelope of the pulse. In figure 3.9 a) and d), two cases of electric fields with different values of the CEP are shown. Since the emission of attosecond pulses is connected to the maxima of the electric field, it is obvious, that a change of the CEP causes a change in the emitted attosecond pulse train structure. The assumption that a cosine pulse, where the maximum of the electric field coincides with the maximum of the pulse envelope, produces a single attosecond pulse seems likely. But due to the complex interaction of the laser pulse with the plasma, this is not so obvious.

A valuable tool to address such questions are PIC simulations (for a detailed introduction see for example reference [80]). Using the 1D PIC-Code LPIC [131] for CEP values between $\phi = 0$ and $\phi = 2\pi$ reveals some interesting results. The parameters of this numerical study are chosen close to the ones experimentally achievable with the Light Wave Synthesizer 20 (LWS-20) (see section 4.1). The pulse length τ_L is 3 cycles full width at half maximum (FWHM) in intensity, corresponding to $\tau_L \approx 8 fs$ at a central wavelength of $\lambda_L = 800 nm$. The intensity and angle of incidence are given with $a_L = 2.0$ and $\theta = 45°$ respectively. A target density of $n_e = 400 n_c$, corresponding to fused silica, with an assumed exponential density ramp with a scale length of $L = \frac{\lambda_L}{8}$ is set. For each case of input electric field (red line in figure 3.9 a) and d)), the PIC code gives the complete reflected electric field of the pulse (blue line in figure 3.9 a) and d)). Doing a fast fourier
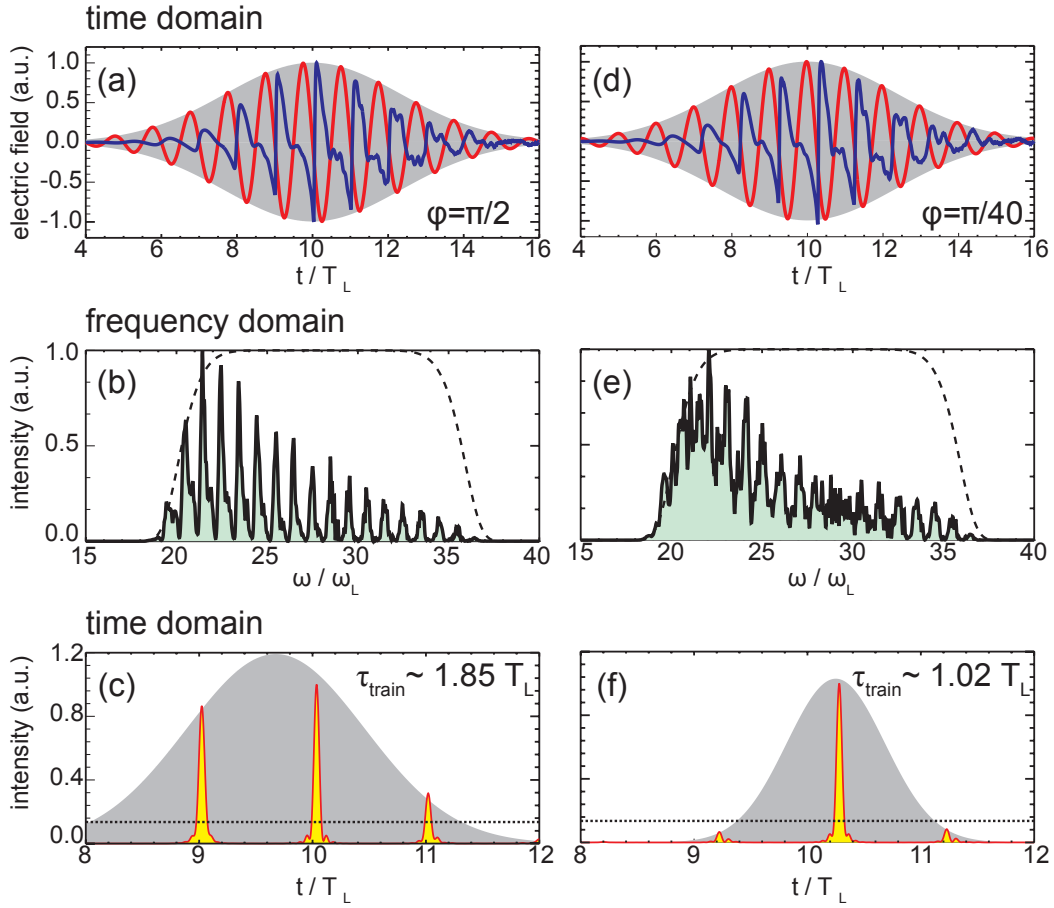
Figure 3.9.: 1D PIC simulation of the interaction of a three-cycle laser pulse with a solid plasma for two values of CEP. In a) and d) the incoming (red) and reflected (blue) electric field are shown for CEP values of $\varphi = \pi/2$ and $\varphi = \pi/40$ respectively. The temporal envelope is shown in grey. b) and e) show the spectra of the reflected fields obtained by FFT and multiplied by a super-Gaussian filter function (dotted line). The time domain behaviour of the filtered fields gained from an IFFT are shown in c) and f). The intensity of the attosecond pulse train is plotted as a red line (yellow filled) and the dotted black line corresponds to $1/e^2$ of the strongest attosecond pulse. The grey area is a Gaussian fit to the pulse train to deduce its width.

transform (FFT) of this reflected field reveals the generated harmonic spectrum. In figure 3.9 b) and e) two of these spectra are shown multiplied with a super-Gaussian filter function (dotted line) modelling the spectral field of view of the spectrometer used in the experiments in chapter 4. An inverse fourier transform (IFFT) of these filtered spectra provides the temporal structure of the attosecond pulse train (see figure 3.9 c) and f)). If only pulses with an intensity higher than $\frac{1}{e^2}$ of the most intense pulse within the respective train are counted, then, for the chosen examples in figure 3.9, a train of three pulses ($\phi = \frac{\pi}{2}$) and a single pulse ($\phi = \frac{\pi}{40}$) can be observed. These pulses are results of the strong distortions of the electric field and are temporarily localized at the points of the steepest slopes in the waveforms. The strong non-linearity of the process confines the emission of the attosecond pulses to only the strongest cycles within the laser pulse. Performing a non-linear least squares Gaussian fit $I_{train}(t) \propto e^{-4ln2(t^2/\tau_{train}^2)}$ to the peaks of the pulses extracts the duration of the train τ_{train} (gray area in figure 3.9 c) and f)). For the case of a single attosecond pulse, the harmonic structure in the spectrum is still visible, but the harmonics start to overlap and a coherent background forms (see figure 3.9 e)). The temporal structure of the generated pulse trains for 40 CEP values between $\phi = 0$ and $\phi = 2\pi$ is shown in figure 3.10 a) and color-coded on a logarithmic scale. It can clearly be seen,
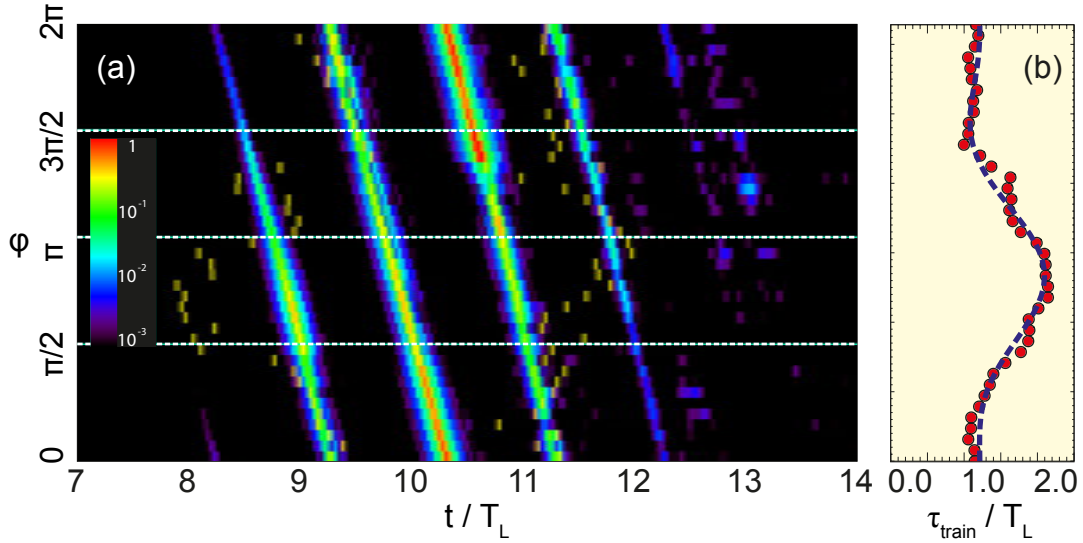

Figure 3.10.: In figure a) the CEP dependence of the number and timing of the attosecond pulses in the generated train is shown in a colour coded plot on a logarithmic scale, for a three-cycle driving laser pulse with an intensity of $a_L = 2$. The region where all the pulses are higher than $1/e^2$ of the main pulse of the respective train is marked by yellow bars. The deduced width of the train is plotted as a function of the CEP in b).

that the emission times and relative intensities of the emitted pulses shift with

the CEP. The yellow lines mark the region, outside of which all the satellite pulses have less than $\frac{1}{e^2}$ of the intensity of the main attosecond pulse. This shows that there are intervals where only a single attosecond pulse is produced but also intervals of up to four pulses in the train. Evaluating the Gaussian fit to the pulse train of each CEP value reveals that the envelope of the attosecond pulse train is shortened compared to the driving laser envelope to between 1 and 2 T_L, depending on the CEP value. In figure 3.10 b), the FWHM duration of the pulse train is given as a function of the CEP. The average width of the trains is $\langle \tau_{train}/T_L \rangle = 1.47 \pm 0.4$. From this the instantaneous non-linearity α can be estimated as $\alpha \simeq \langle (\tau_L/\tau_{Train})^2 \rangle = 5.0 \pm 2.3$. This value is in good agreement with previous measurements for the overall non-linearity of the process by Teubner et al. [130].

Treating φ as a random parameter, i.e. no phase stabilization is applied, the percentage of shots, that deliver a certain number of attosecond pulses in the train can be deduced. For a 3-cycle driving laser this gives a 5% likelihood for getting four pulses in the train. 49% and 29% of the shots will lead to three and two pulses in the train, respectively. The remaining 17% of the shots will deliver isolated attosecond pulses. For example, in a window of $\Delta\varphi \simeq \pm 0.31 rad$ around $\varphi \simeq 4.71 rad$ single attosecond pulses are reliably produced. Doing the same analysis for a 2-cycle driver already reveals a probability of more than 50% for isolated attosecond pulses relieving the need for CE-stabilization of the laser and allowing experiments with CE-tagging [148] only.

4. High-Harmonic Generation with a Few-Cycle Driver

In the previous sections, the principles of the generation of single attosecond pulses with relativistically intense laser pulses have been introduced. Theory, simulation and earlier experimental results suggest that there is a significant relaxation of the requirements on the pulse length of the driving laser compared to the gas-harmonic case due to the strong instantaneous non-linearity. With the Light Wave Synthesizer 20 (LWS-20) [73] at the MPQ, delivering the most powerful few-cycle pulses to date, a unique light source is available to test these predictions experimentally.

In this chapter, the first observation of relativistic harmonics generated with a few-cycle driver will be presented. The measured spectra extend up to the 47th harmonic order and, although still discrete in form, are considerably broadened and exhibit some overlapping in agreement with the simulated data of section 3.3. Before the experimental results will be presented, the components and parameters of the LWS-20 which are important for the measurements will be introduced in section 4.1 and then an overview of the experimental setup will be given in section 4.2.

4.1. The Light Wave Synthesizer 20

The LWS-20 is an all-optically synchronized, non-collinear optical parametric chirped-pulse amplification (NOPCPA) system [10, 149]. The front-end consists of a Ti:Sapphire oscillator delivering pulses of some nJ in energy and a pulse length of 5-6 fs. These pulses are then unequally split into two, and 2/3 of the energy are used as a seed for the amplification chain and are directly amplified in a 1 kHz Ti:sapphire 9-pass amplifier. The pulses with the remaining 1/3 of the energy are used as a seed for the pump lasers to fully optically synchronize the system [73]. This all-optical synchronization results in a timing jitter of less than 1 ps for the temporal overlap of the pump and seed pulses in the amplification stages [150]. In the amplification chain, the seed is first spectrally broadened in a hollow-core fibre, subsequently stretched in a combined grating and prism (grism) stretcher and then partially compressed in an acousto-optic modulator (DAZZLER, Fastlite) to a pulse duration of $\sim 25\, ps$. An optional

cross-polarized wave generation (XPW) stage can be introduced into the system before the pulse is stretched to improve the temporal contrast of the laser. The use of a grism stretcher with negative dispersion permits the use of a positive dispersion compressor at the end of the amplification chain consisting of bulk glass and chirped mirrors, which results in a higher transmission and smaller polarization dependence than a grating compressor. The Dazzler gives the opportunity to pre-compensate distortions of the spectral phase of the laser pulse. This allows, for example, for precise control of the spectral phase to minimize the measured pulse duration in a second-order auto-correlator or for fine-tuning of the laser pulse to achieve the favoured harmonic signal. The pulses are amplified from a few μJ after the dazzler to up to $170\,mJ$ in two consecutive single-pass Type I BBO stages at a repetition rate of $10\,Hz$. The spectrum of the amplified pulses stretches from $700\,nm$ up to $980\,nm$ with a central wavelength of $\sim 800\,nm$ (figure 4.1 a)). A bulk glass compressor consisting of $160\,mm$ SF57 and $100\,mm$ Quartz pre-compresses the pulses, which subsequently enter a vacuum chamber equipped with four positively-chirped mirrors to fully compress the pulses down to $\sim 8\,fs$ (see figure 4.1 b)). An adaptive mirror connected to a wavefront sensor in a closed-loop scheme is used to optimize focusability, and is mounted right before the vacuum chamber. A double plasma mirror can be inserted into the beam to further improve the contrast of the laser [151] after the chirped mirrors. From there, the pulses, with a diameter of $\sim 45\,mm$, are steered through a fully motorized vacuum beam-line to the experimental chamber, where the vacuum prevents self-phase modulation.

A number of diagnostics are available to characterize the laser pulses. A spectrum and a corresponding second-order auto-correlation trace are shown in figure 4.1 a) and b), respectively. A home-built third-order auto-correlator is used to measure the temporal pulse contrast (see figure 4.1 c)). The intensity contrast on the $100\,ps$ scale is intrinsically good and below the detection limit, due to the use of pump pulses with only an $80\,ps$ duration and the OPCPA technique for amplification. A first significant rise of the relative intensity to $\sim 10^{-6}$ is observed on the $20\,ps$ scale when the pump pulses start to interact with the BBO material. The pulse exhibits a further sharp rise to a plateau at the $\sim 10^{-4}$ level at $\sim 5\,ps$, before rising towards the main peak within the final $\sim 1\,ps$. By inserting the XPW unit into the system, the contrast can be significantly enhanced to $< 10^{-7}$ at a few ps before the pulse (see figure 4.1 c)).

4.2. Experimental Setup

After being transported to the experimental chamber with a measured combined throughput of the compressor and the beam-line of $\sim 60\%$, the laser is focused using a 30° off-axis parabolic mirror with an effective focal length of $160.8\,mm$.
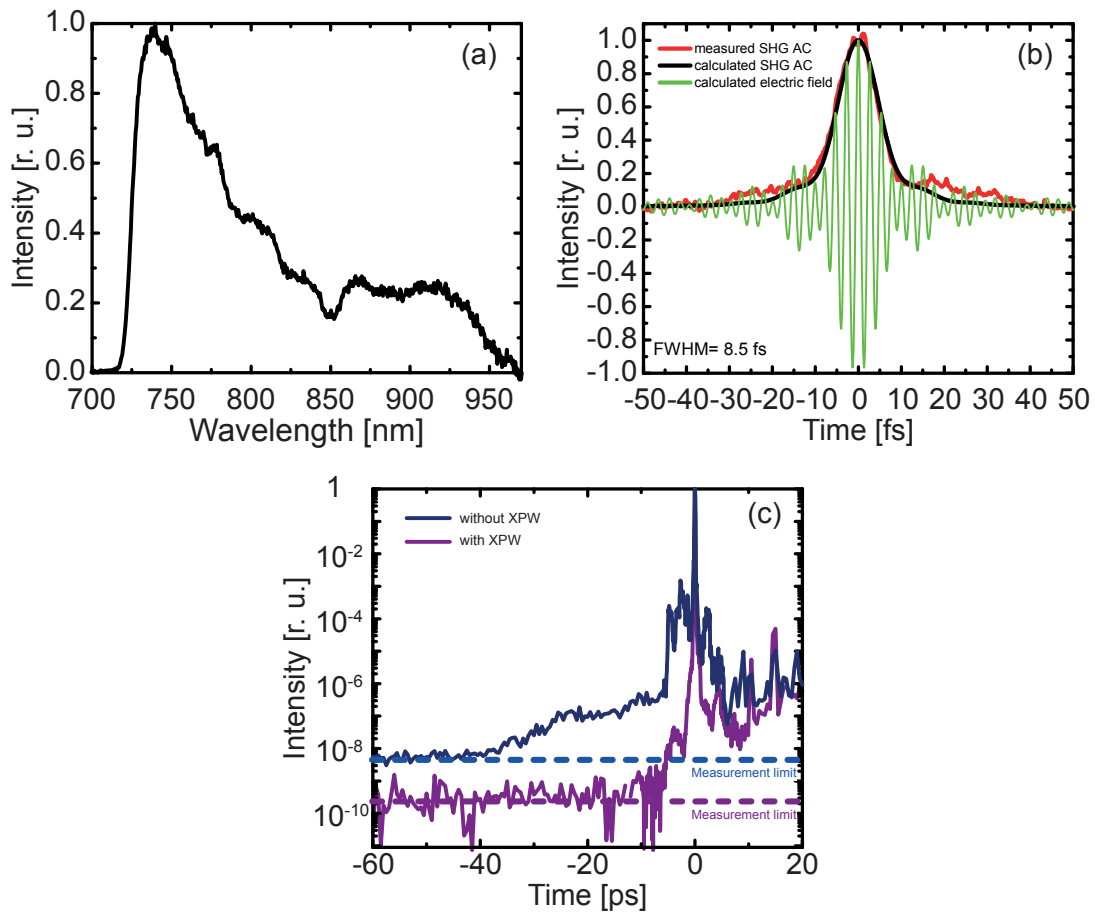
Figure 4.1.: a) The LWS-20 spectrum stretches from $\sim 700\,nm$ to $\sim 980\,nm$. b) The measured (red) second-order auto-correlation-trace deviates only slightly in its wings from the calculated one (black) obtained from the spectrum in a). c) The measured third-order auto-correlation-trace shows an intrinsically good contrast (blue), which can be further enhanced by the use of the XPW technique (purple).

The intensity on the target is determined by measuring the focal energy distribution of the attenuated beam using a microscope objective in combination with a 14-bit CCD camera. The alignment of the parabolic mirror is manually optimized, and residual higher order aberrations are removed by using the adaptive mirror. Thus a focal spot distribution with $\sim 75\%$ of the energy within the first
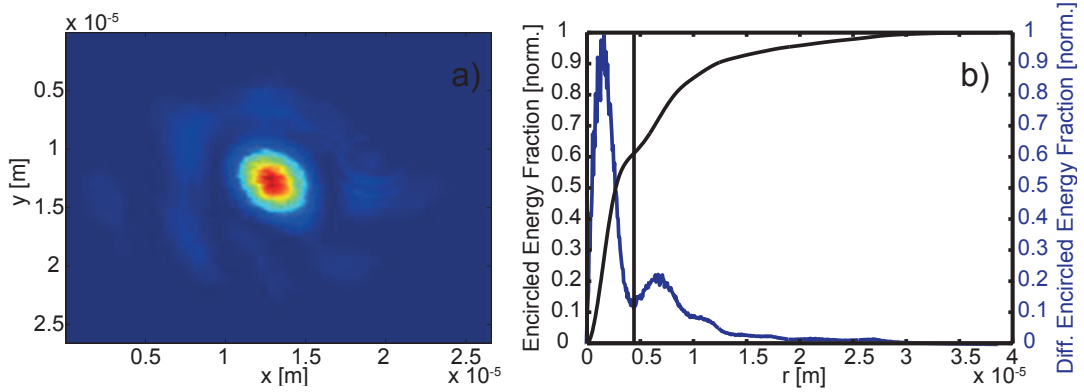
Figure 4.2.: a) shows the measured intensity distribution in the focus, and b) shows the fraction of the energy encircled within a certain radius (black) and its first derivative (blue) to determine the first Airy minimum.

Airy disk ($r \approx 4.5\,\mu m$) can be achieved, resulting in an averaged normalized vector potential, in this area, of $\overline{a}_L \approx 2$ and a peak value of $a_L^{Peak} \approx 3$.

The microscope and the target mechanism are attached to a joint motorized translation stage to bring them in and out of the beam (see figure 4.3 a)). The employed targets are fused-silica discs with a diameter of $120\,mm$ which are mounted at an angle of $45°$ to the incoming beam on top of three additional motorized, computer-controlled stages. One translation stage is mounted parallel to the incoming beam to set the target in focus. The second translation stage together with a rotation stage move the target substrates after every impinging laser pulse on a spiralling trajectory to ensure a clean interaction surface. The reflected radiation is collected by a $75\,mm$ spherical mirror with an unprotected gold coating at a $70°$ angle of incidence (see figure 4.3 b)) and then directed onto the entrance slit of a grazing-incidence imaging XUV spectrometer (McPherson 248/100G). This spectrometer is equipped with a $133.6\,\text{lines}/mm$ grating and an optional $150\,nm$ thick Al foil filter for background suppression. The spectrometer is described in detail in [86].

In the course of the data analysis, it was found that the calculated wavelength scale of the spectrometer shows a deviation from the observed harmonic spectra. Therefore, a calibration by an oxygen spectral line at $17.2\,nm$ [152] and its 2nd order is applied. These lines are registered by the spectrometer when the laser interacts with a damaged region on the target, e.g., from a previous shot
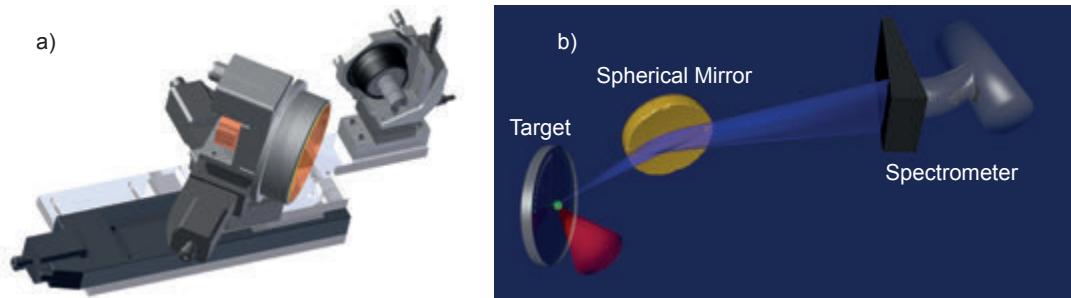
Figure 4.3.: a) The fused-silica targets are mounted on 3 motorized stages for alignment of the targets in the focal plane of the laser and movement to an undamaged spot of glass after every shot. An additional motorized stage is used to place a microscope objective in focus. b) The experimental setup consists of a fused-silica target, a spherical, bare-gold collection mirror and a grazing-incidence spectrometer.
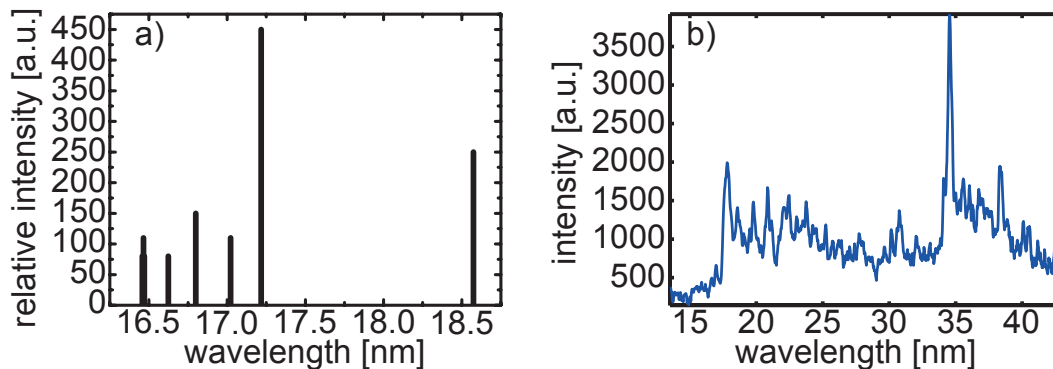
(figure 4.4). These oxygen spectra are also used to quantify the spectrometer

Figure 4.4.: a) Emission lines of oxygen in the region around the Al filter cut-off. All lines stem from the OV ion (data from [152]). b) Measured spectrum of the interaction of a laser pulse with a previously damaged target spot. The line at $17.2\,nm$ and its second order at $34.4\,nm$ are clearly visible.

resolution, which was determined to be $\Delta\lambda \approx 0.19\,nm$ by assuming an infinitely narrow single line. This leads to a broadening of the harmonics from $\sim 3\%$ at the 20th to $\sim 12\%$ at 30th.

4.3. Measurement of High-Harmonic Spectra with a Few-Cycle Laser

Throughout the experiments with LWS-20, harmonics were readily observed. The transition to the relativistic regime and the associated occurrence of ROM harmonics beyond the CWE cut-off, though, was only achieved by careful tuning of the laser parameters, especially the focal spot distribution. With an average focused intensity of $\overline{a}_L \approx 2$, within the first Airy minimum, the experiments are operated right at the onset for relativistic harmonic generation. This prevents, for example, the use of a plasma mirror setup, since the reduced throughput will suppress relativistic effects. Once the conditions pertaining to the interaction are met, harmonics well above the CWE cut-off at harmonic 20, i.e. $40\,nm$, and down to the Al filter cut-off at $17\,nm$ are reproducibly observed. An exemplary spectrum, together with a raw image of the CCD, is shown in figure 4.5. The
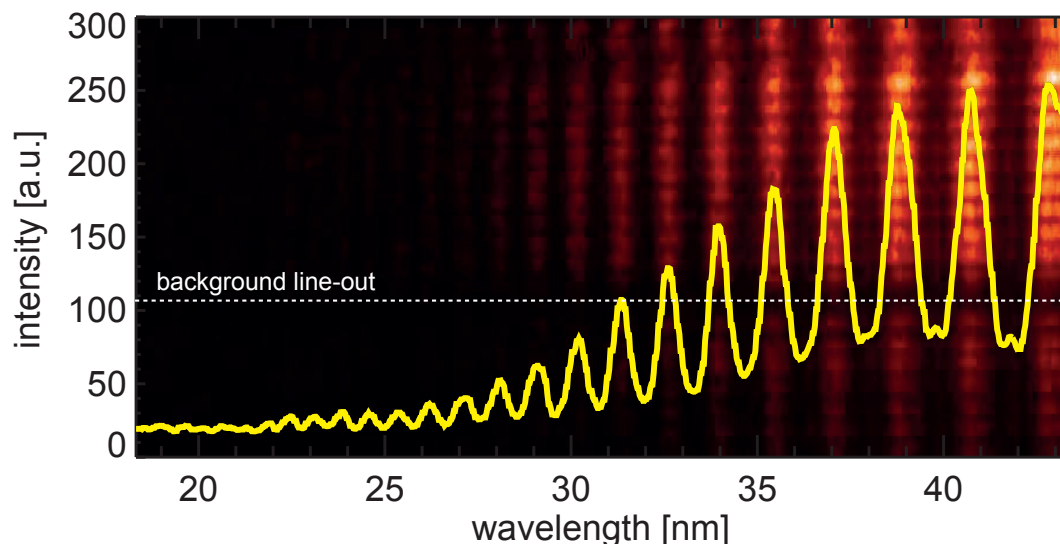
Figure 4.5.: The raw CCD image shows the support grid of the Al-filter. The white line shows the possible position for the line-out for the background correction.

CCD image shows a horizontal modulation of the signal, which comes from the supporting mesh of the thin Al foil. By taking a line-out in the shadow of one of the support bars (see figure 4.5), an estimation of the background level can be made.

Evaluating these spectra in terms of the relative width of the harmonics gives a measure for the smallest possible temporal envelope of the attosecond pulse train. By fitting Gaussians to the individual harmonics (see figure 4.6), an average
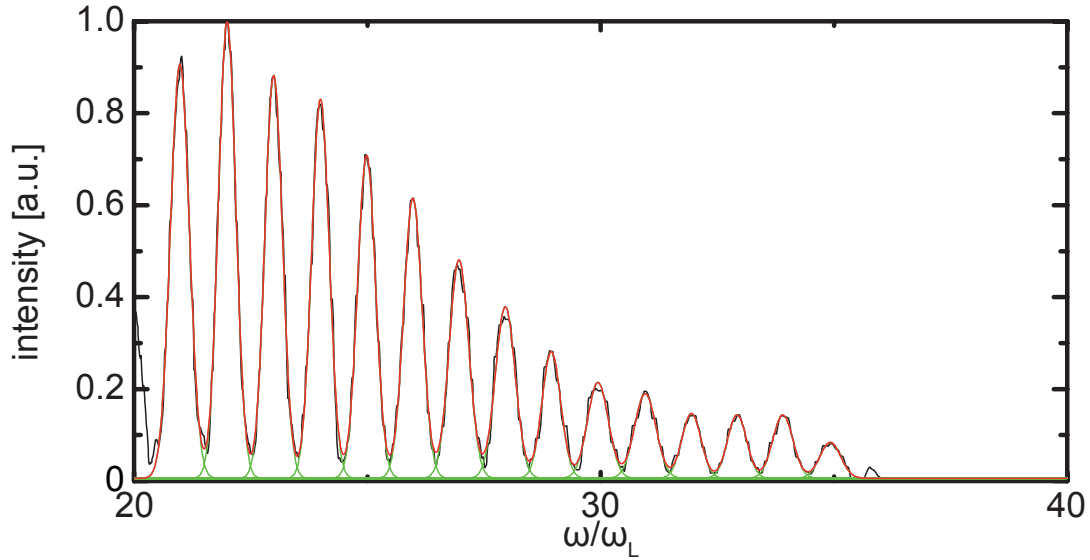
Figure 4.6.: The harmonics are fitted with Gaussian functions to obtain their relative width for an estimation of the pulse train length.

spectral width of $\langle \Delta\omega/\omega_L \rangle = 0.45 \pm 0.017$ is obtained. This is significantly broader than the Fourier-Transform limited value of the driving laser envelope of $\Delta\omega/\omega_L = 0.44 T_L/\tau_L \approx 0.15$, and hence implies that the temporal duration of the envelope of the harmonic pulse-train can be substantially shorter than the driving laser pulse, which is in agreement with the PIC simulations of section 3.3.

As already mentioned, a pivotal parameter in connection with the generation of intense, single attosecond pulses is the inherent non-linearity α of the efficiency η_{XUV} of the conversion process. To address this, an intensity variation is performed by introducing an iris into the laser beam. For four settings of the aperture ($39mm$, $34mm$, $30.5mm$, $27mm$), the average of the integrated intensity in the spectral region between harmonic 20 and harmonic 30 of approximately ten shots is determined. Considering the effect of the iris on the focal spot distribution this results in relative XUV intensities for four different laser intensities on the target, which are shown in figure 4.7. The absolute efficiency of the process is not accessible by this measurement due to the use of non-calibrated detectors and optics but will be determined in section 5.3. Fitting a power law to these data points reveals an extremely high apparent non-linearity of $\alpha = 6.3 \pm 0.49$ which is attributed to the dynamic behaviour of the plasma evolution at the interface. The different laser intensities lead to different onset times of the plasma formation: The sooner the plasma forms, the more time it has to stretch out into the vacuum. Since the scale length is another critical parameter in the XUV generation besides the laser intensity, this will greatly influence the efficiency of the process. To further substantiate this conclusion, 1D PIC simulations with param-
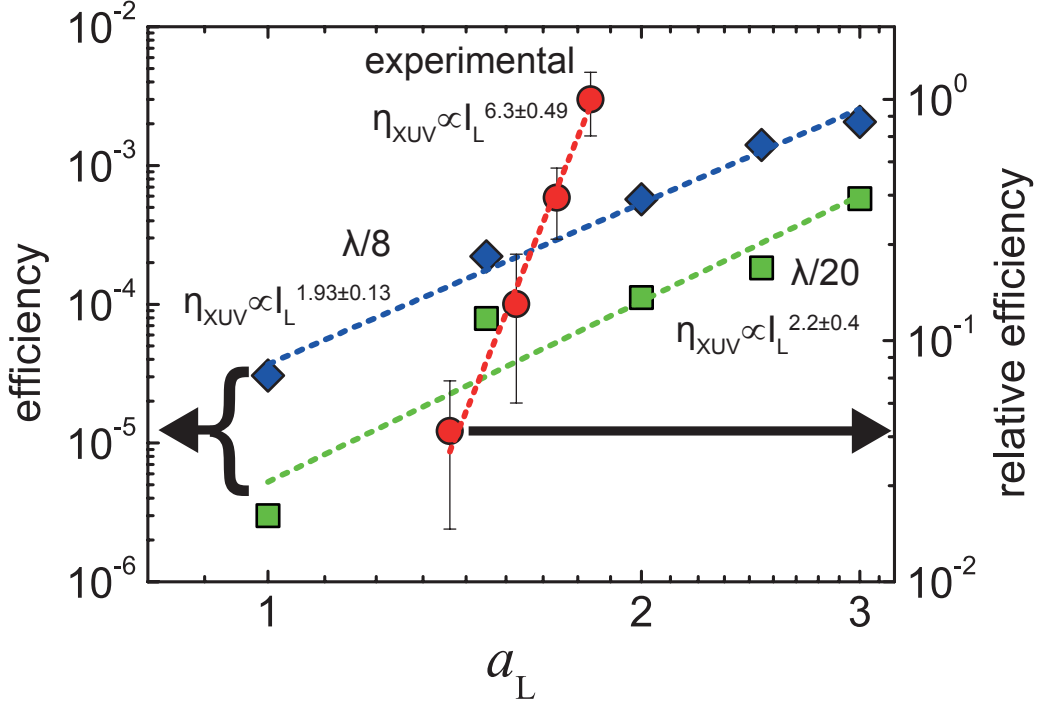
Figure 4.7.: Dependence of the XUV conversion efficiency on the laser intensity. Data from 1D-PIC simulations for plasma scale lengths of $L = \lambda/8$ (blue) and $L = \lambda/20$ (green) are compared to experimentally obtained, normalized data (red).

eters close to the experimental values ($n_e/n_c = 400$, $\tau_L = 3$, angle of incidence $\Theta_L = 45°$) are performed at various intensities and two scale lengths L ($L = \lambda/8$ and $L = \lambda/20$). The use of a 1D PIC code is based on the assumption that the electrons see a uniform field and surface deformations are negligible. This is justified since the laser focal spot size is larger than the length of the three-cycle laser pulse of $\sim 2.4\ \mu m$ and the transverse amplitude of the electron oscillations [153], and surface denting [87] are on the nm scale. The results are shown in figure 4.7. The resulting non-linearities of $\alpha = 1.93 \pm 0.13$ and $\alpha = 2.2 \pm 0.4$ for $L = \lambda/8$ and $L = \lambda/20$ respectively are in very good agreement with each other but far lower than the experimental value. This can be explained by the aforementioned effect of the pre-plasma. While for the two PIC cases, the scale length L is constant for all intensity values, the scale length will increase with higher intensity in the experimental case. It has been found that longer scale length enhances the harmonic generation efficiency within certain limits [88] and hence, will here efficiently increase the observed non-linearity. Concluding, the plasma medium has an efficiency for the up-conversion in the currently readily

accessible range which varies as $\eta_{XUV} \propto I_L^\alpha$ with $\alpha \gtrsim 2$. This lower limit for α is in good agreement with the value of $\alpha = 5.0 \pm 2.3$ obtained from the PIC simulations in section 3.3.

A special characteristic of the harmonic spectra generated with a few-cycle driving laser is a change of the shape of the individual harmonics with the CEP of the driving laser pulse. In the case of CWE harmonics, this has been shown theoretically and experimentally and is caused by the unequal spacing of the generated attosecond pulses due to varying excursion lengths of the connected electrons (see section 3.1 or reference [89]). In the ROM case also small variations in the relative positions and intensities of the generated attosecond pulses for different values of the CEP of the driving laser pulse occur (see figure 3.10) and hence give rise to a fine structure on the observed harmonic spectra. The LWS-20 system with its three-cycle pulses can be used to experimentally observe this fine structure. Since the CEP of the system is currently not stabilized, every shot has a different value of the CEP. Taking single shot spectra and leaving all accessible laser parameters unchanged should thus result in varying harmonic spectra from consecutive shots. In figure 4.8, eight consecutive harmonic spectra are shown. These spectra exhibit strong variations in the spectral features of the harmonics, as expected from the PIC simulations in section 3.3. Although no one-to-one correspondence can be made between the experimental and the simulated spectra due to the lack of CEP measurements in the experiment, strikingly similar features in experimental and simulated spectra can be found. The smooth spectrum in figure 3.9 b) corresponding to a triple pulse train, for example, strongly resembles the experimental spectra in figure 4.8 b) and e). The structured spectrum in figure 3.9 c) corresponding to a single, isolated attosecond pulse, however, is remarkably similar to the experimental spectra in figure 4.8 f) and g). Since the observed spectra span the whole transmission window of the used Al filter, the spectral width of this window can be used to estimate the pulse duration, giving a value of $\tau_{XUV-Pulse} \approx 80\,as$ [66]. As mentioned before the shot-to-shot variations in the measured spectra are attributed to fluctuations of the CEP. Fluctuations of other parameters such as pulse duration and energy were measured and observed to be very small ($< 5\%$) and thus can not be responsible for the observed variability. A similar behaviour has been reported recently for multi-cycle pulses by Behmke et al. [127]. However, the explanation furnished in this case is not applicable to our measurements. A prerequisite for the mechanism claimed by Behmke et al. is a soft pre-eplasma caused by a laser pulse with poor temporal contrast. This can be excluded in the experiments shown in this chapter, since the LWS-20 has, due to the use of the NOPCPA technique, an inherently good contrast and hence it produces a very steep pre-plasma. Additionally, measurements with the XPW unit introduced into the laser chain improved the contrast but had no influence on the observed spectral variation. Therefore, the effect
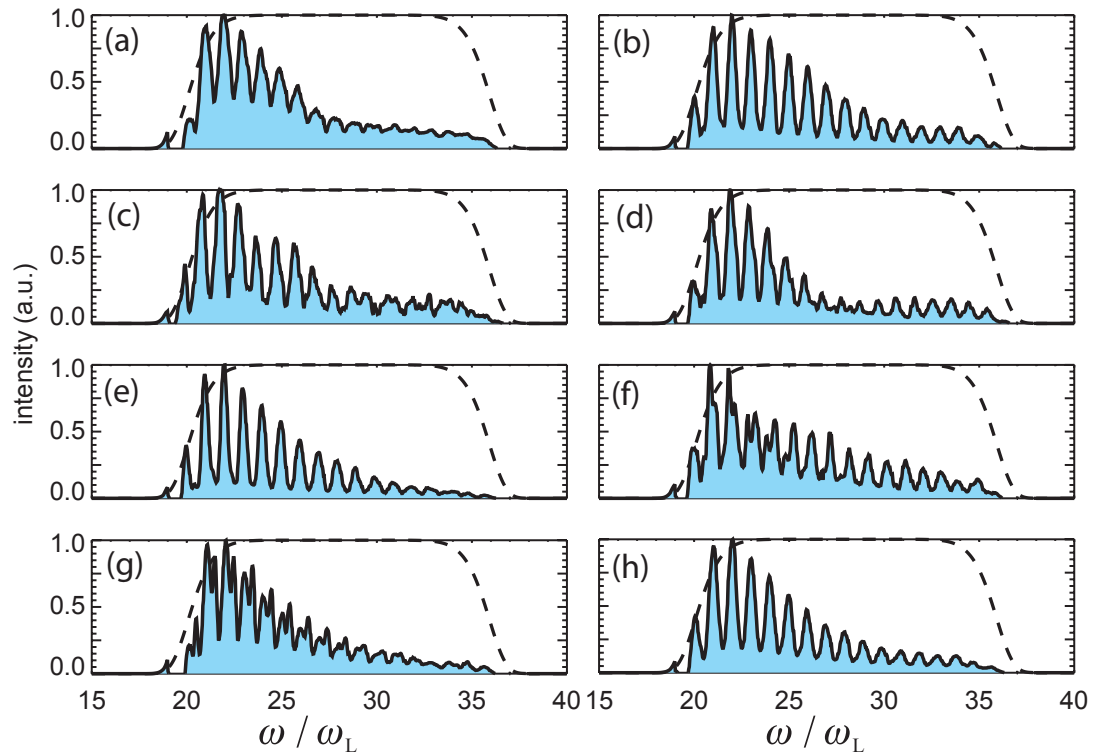
Figure 4.8.: Sample harmonic spectra in the frequency domain after background subtraction. While all accessible laser parameters are kept constant, a clear change in the spectral structure is observable due to the changing CEP.

explained by Behmke et al. can be safely excluded and the observed spectral features are solely attributed to the varying CEP.

5. Generation Efficiency and Divergence of Relativistic Harmonics

The previous chapter established the possibility of generating single pulses spanning a spectral bandwidth wide enough to support pulse durations on the $100\,as$ scale. For utilizing the pulses, two other parameters are very important: the conversion efficiency of the process and the divergence of the emitted upconverted light. Both are discussed in this chapter.

For the ROM process, high conversion efficiencies have been predicted compared to the case of high-harmonic generation from gases. Tsakiris et al. [66] calculated efficiencies as high as $\eta_{XUV} \approx 10^{-2}$ in a spectral range of $20 - 70\,eV$, which corresponds to the transmission window of an Al filter. This means that for a laser intensity of $I_L \simeq 10^{19}\,\frac{W}{cm^2}$ isolated attosecond pulses with a duration of $\tau \approx 80\,as$ and pulse energies of $200\,\mu J$ are feasible [66]. These pulse energies are orders of magnitude higher than what is currently achieved by state of the art harmonic sources based on gaseous media. Here, the highest energy isolated attosecond pulses to date in the $20-40\,eV$ spectral range are on the order of a few tens of nJ [38, 40] partially owing to the much lower applicable laser intensities of only $I_L \simeq 10^{15}\,\frac{W}{cm^2}$.

Besides the conversion efficiency, the emission characteristics of the XUV is very important for the applicability of this source. Of special interest are the divergence, which is examined in section 5.3 and the focusability, which is the topic of section 6.2. As discussed in section 3.2, the pre-plasma has a strong influence on the conversion efficiency as well as the beam properties. For a short pre-plasma, the relativistic harmonics are emitted in a small cone with a divergence that is even smaller than the diffraction limit [87, 125], but a very long and turbulent pre-plasma undermines this beamed emission and rather, leads to a scattered emission into a wide angle [121, 137, 139].

Before showing and discussing the experimental findings in section 5.3, the Advanced Ti:Sapphire Laser (ATLAS) located at the MPQ, which was used for the experiments is introduced in section 5.1, and then an overview over the experimental setup is given in section 5.2.

5.1. The Advanced Ti:Sapphire Laser (ATLAS)

The ATLAS is a Ti:sapphire-technology based chirped-pulse amplification system which has already undergone several upgrades. It is based on a broadband oscillator, which delivers pulses with a duration of $\tau_L \approx 20\,fs$ and $E_L \approx 5\,nJ$ of energy. These are subsequently amplified in a multi-pass pre-amplifier before being stretched in a grating stretcher. Similar to the LWS-20 an acousto-optic modulator (DAZZLER) is used to control the spectral phase. A regenerative amplifier, incorporating another acousto-optic modulator (MAZZLER) to prevent gain narrowing, boosts the pulses to $\sim 2\,mJ$ of energy before they are sent to a chain of 4 multi-pass amplifiers. After the last amplifier the system delivers $\sim 3\,J$ of pulse energy at a repetition rate of $5\,Hz$. Lower pulse energies are possible by leaving the pump lasers of the last or even the two last multi-pass amplifiers off, taking a loss from the laser pulse passing the unpumped amplifiers. The reduction of the number of amplifiers in operation has the additional advantage of making the system much faster to turn on and easier to operate. A fine tuning of the pulse energy can be done by shifting the timing of the pump-pulses in the amplifiers with respect to the seed pulse, hence reducing the overlap and the resulting gain. After the amplification chain, the laser pulses hit an adaptive mirror connected to a wave-front sensor to increase the focusability. Contrary to the adaptive mirror in the LWS-20, it is not possible to use the adaptive mirror in the ATLAS to directly improve the focus. At the end, the pulses enter a vacuum chamber connected to the same beam-line system as the LWS-20 and are compressed to $\sim 30\,fs$ by a grating compressor. The transmission of the compressor combined with the beam-line was measured to be $(38 \pm 2.5)\%$. Also for the ATLAS, a number of diagnostics are available. The contrast on the $\sim 300\,ps$ scale is measured by a commercial third-order cross-correlator (Sequoia, Amplitude Technologies) or the same home-built third-order auto-correlator also used for LWS-20 (see figure 5.1). Since the ATLAS uses long pump pulses for pumping the crystals in the amplifier chain, it is much more prone to contrast problems than the LWS-20. The measured trace reveals a contrast of $\sim 10^{-7}$ at $10\,ps$ (see figure 5.1) and a contrast of $\sim 10^{-11}$ on the nanosecond scale was measured by using calibrated photo-diodes. The two measurement techniques leave an unaccessible region from $\sim 300\,ps$ to a few nanoseconds where no information about the contrast is available. A third-order auto-correlator with an observation window on the $\sim 10\,ns$ scale has been partially developed in the course of this thesis and is currently being tested. A double plasma-mirror setup for contrast improvement is available, but was not used for the described experiments. For the pulse control on the femtosecond scale, a FROG device (GRENOUILLE, swamp optics) is available (figure 5.1).
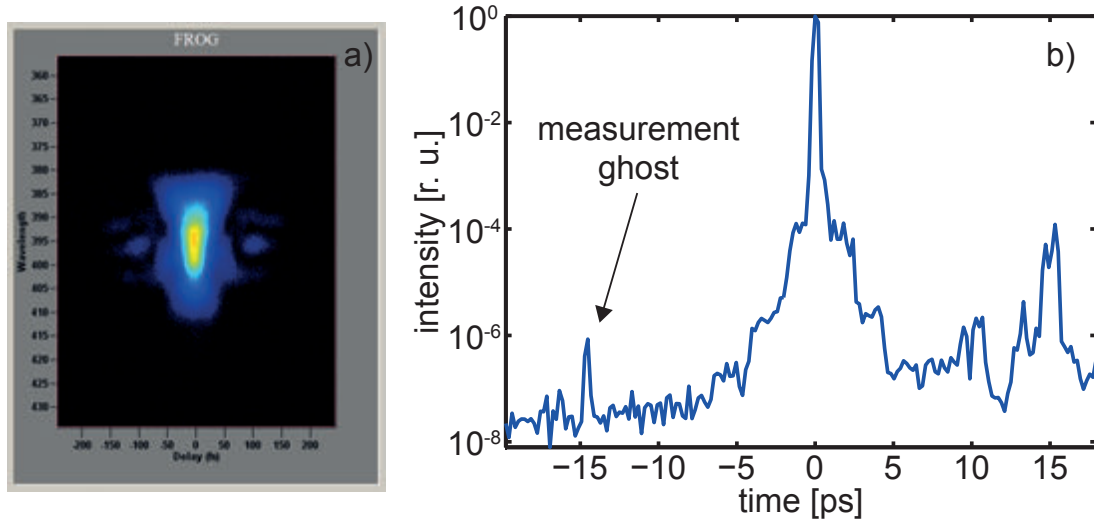
Figure 5.1.: Temporal characterization diagnostics of ATLAS. A FROG device is used to measure 2nd and higher order dispersion to achieve pulse durations of $28\,fs$. A FROG trace is plotted in a). The third-order auto-correlation trace in b) shows a contrast of $\sim 10^{-7}$ on the $10\,ps$ scale. The peak at $-15\,ps$ is a measurement artefact of the post-pulse at $15\,ps$.

5.2. Experimental Setup

For these experiments a new focusing off-axis parabolic mirror is used. The geometry was specifically designed in the course of this thesis for high field experiments with the laser systems available at the Max Planck Institute of Quantum Optics (MPQ), and the coating of enhanced silver was chosen accordingly. The mirror has a 90° off-axis angle with a clear aperture of $100\,mm$ and an effective focal length of $f_{eff} = 200\,mm$. It is hence a F/2.5 optic for the ATLAS beam with a diameter of $80\,mm$. The surface roughness is specified better than $60/40$ (scratch/dig), and the surface quality is better than $\lambda/3$ at $633\,nm$.

The focus is monitored, like in chapter 4, by a microscope objective mounted on a 14-bit CCD camera. The focal spot with a diameter of $3\,\mu m$ contains 34% of the focused energy, whereas within the first Airy-minimum with a diameter of $7\,\mu m$, 63% of the focused energy is encircled (see figure 5.2). The target mechanism is slightly modified compared to section 4.2. An additional motorized rotation stage is introduced beneath the target for scans and fine adjustment of the angle of incidence. To characterize the beam-profile of the generated harmonic radiation, a Multi-Channel-Plate (MCP) detector with a diameter of $75\,mm$ is mounted in the reflected beam at a distance of $750\,mm$ from the target (see figure 5.3). The MCP is attached to a phosphor screen, which is optically coupled to a 14-bit CCD camera. Special care is taken to prevent any reflected
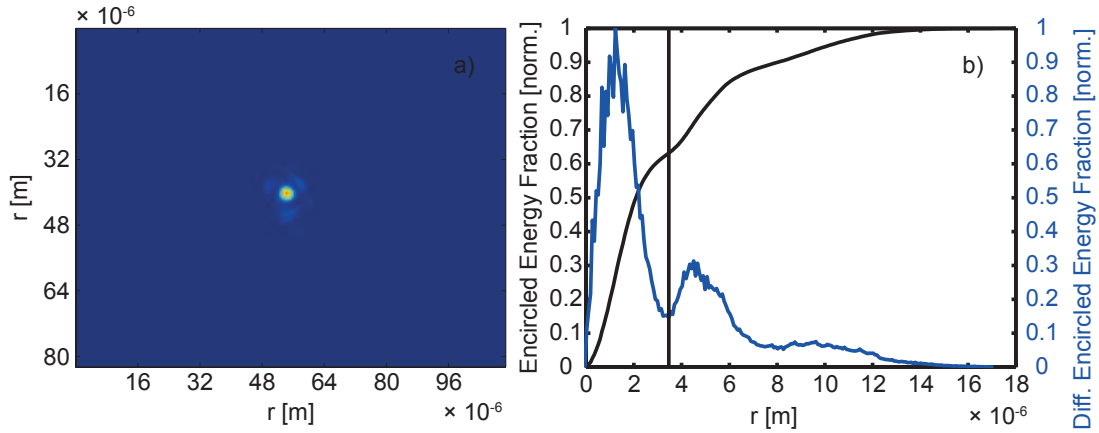
Figure 5.2.: The intensity distribution of the ATLAS focus is shown in a). In b) the encircled energy fraction (black) of the focus and its first derivative are shown to determine the size of the Airy disk.

or scattered light from the laser or any other source, from reaching the MCP. A $500\,nm$ thick Al filter with a diameter of $25.4\,mm$ is used to spectrally filter the light reflected off of the target. This filter is mounted on a cone with covered holes to allow for differential pumping while at the same time hindering any stray light from entering the chamber. A calibrated IRD AXUV diode, connected to an oscilloscope, is mounted on a long manipulator and can be introduced between the MCP and the Al filter inside the light-tight chamber (see figure 5.3). This allows for simultaneous measurements of the XUV conversion efficiency with the diode and the XUV beam-profile with the MCP. From these simultaneous measurements, the fraction of the beam covered by the diode is directly accessible. An additional $750\mu m$ thick Al filter is attached to the diode to prevent saturation.

To monitor the generated harmonic spectra, a flat-field spectrometer, which is described in detail in reference [87], and equipped with a Hitachi flat-field grating with $1200\,\frac{lines}{mm}$ is used. A simultaneous observation of the beam-profile and the spectrum is not possible since an Au mirror is introduced into the harmonic beam-path in front of the MCP chamber to couple light into the spectrometer (see figure 5.3).

5.3. Efficiency and Divergence of Relativistic Harmonics

The ATLAS is capable of delivering $\sim 3\,J$ of pulse energy, and various experimental runs at these highest pulse energies have been performed. The generation of CWE harmonics up to the cut-off at $40\,nm$ was readily achievable. The re-
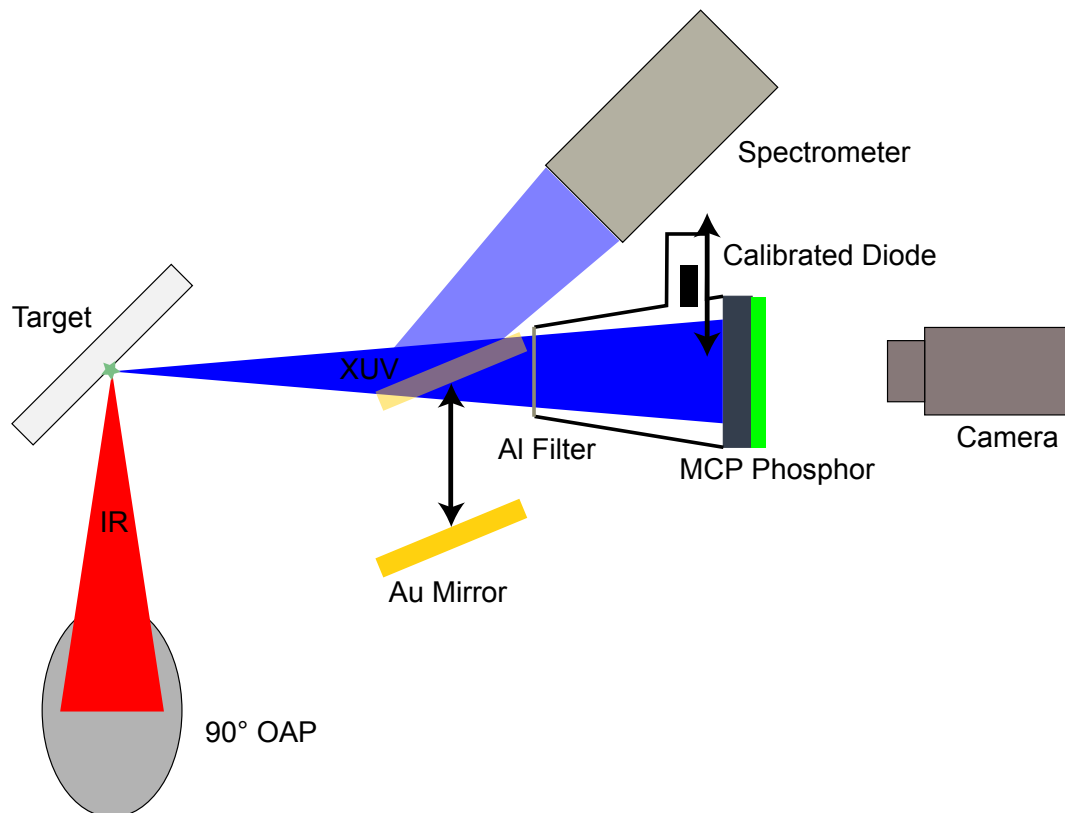
Figure 5.3.: A 90° off-axis parabolic mirror focuses the laser beam onto a fused silica target. The generated XUV beam enters a light sealed chamber and hits a MCP detector connected to a phosphor screen that is imaged by a 14-bit CCD camera. An absolutely calibrated photo diode can be moved into the beam. To control the emitted harmonic spectrum, the beam can be coupled into a flat-field spectrometer by a gold mirror.

producible generation of a broad ROM-harmonic spectrum nevertheless was not possible at these high pulse energies. Only very few ROM harmonics above the CWE cut-off with wavelengths larger than $34\,nm$ were repeatedly observed, and in all shots, a high line-radiation background in combination with increased levels of ionizing radiation has been measured. A likely explanation for this behaviour is an unstable and long pre-plasma due to ionization of the target well before the main peak of the laser pulse. As described in chapter 3, the ROM process is far more sensitive to the pre-plasma conditions than the CWE process. Hence, CWE harmonics will still be observed even when the pre-plasma gets too long for ROM harmonics.

It is technically very difficult to do a parameter study of the pre-plasma length alone without changing any other laser parameter, since this would need the introduction and measurement of a defined and variable pre-pulse and full control over the laser contrast. Additionally, the direct measurement of the onset time of pre-plasma formation as well as the scale length at the instant of the interaction with the main pulse is very challenging. For the attainment of ideal interaction parameters, a different, rather heuristic approach, the variation of the laser pulse energy, can be used, which comes with the disadvantage of lower pulse energies. Since the amplification in the various amplifiers not only raises the energy of the main pulse, but also of possible pre-pulses and the pedestal the main pulse is sitting on, a reduction of the gain of the last amplifier will reduce the energy of these distortions by the same factor it reduces the main pulse. Hence, sufficient lowering of the energy of the main pulse will eventually lead to the suppression of the long-term contrast below the ionization threshold of the target and therefore to desired pre-plasma conditions for ROM harmonic generation. As described in section 3.2, the length and shape of the pre-plasma for most efficient high-harmonic generation depends on the parameters of the driving laser pulse, i.e., amongst others on the pulse energy. Hence an optimum value for the given parameters of the used laser system has to be found.

In figure 5.4, raw images of the spectrometer together with corresponding spectra for three pulse energies are shown. The images and spectra are not corrected for e.g. filter transmission or grating efficiency. In figure 5.4 a) and d) a shot with $\sim 70\,mJ$ pulse energy on the target is shown. The raw image in figure 5.4 a) shows well defined lines at the expected harmonic positions. The corresponding spectrum in figure 5.4 d) confirms the well shaped spectral structure and shows harmonics well beyond the CWE cut-off at $40\,nm$. The maximum of the emission around $40\,nm$ can be explained by the influence of the gold mirror that was used. Figures 5.4 c) and f) show harmonics generated with a laser pulse of $\sim 300\,mJ$ on target. A completely different emission structure can be observed in the raw image (figure 5.4 c)). Harmonic emission is still visible, but it shows a strong modulation with various side peaks. Also in the corresponding spectrum (figure 5.4 f)), the side peak structure clearly appears. The spectrum shows a
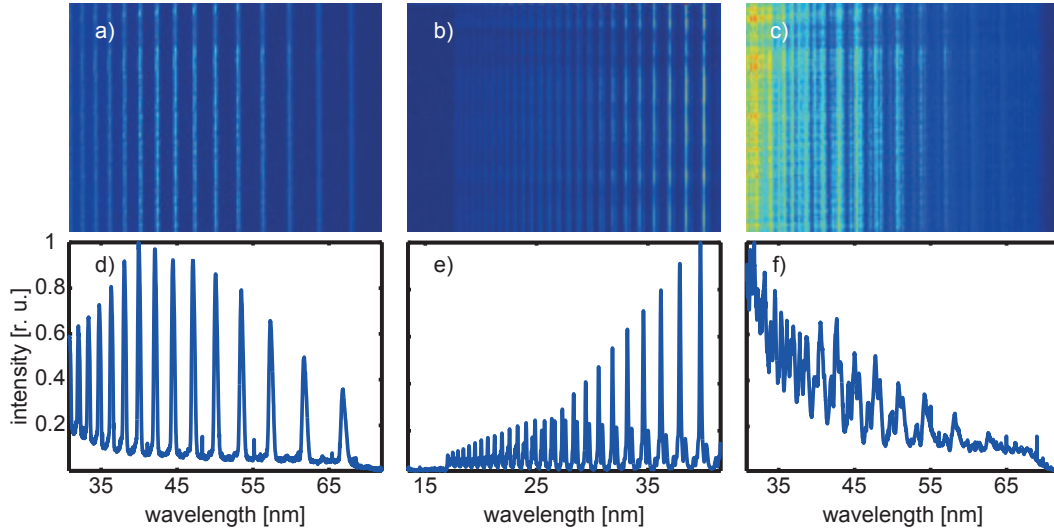
Figure 5.4.: Raw spectrometer images and corresponding spectra generated with 3 different laser pulse energies on target. A clean harmonic structure occurs at low laser pulse energies of $\sim 70\,mJ$, shown in a) and d). A modulation of the spectrum due to higher order motion of the reflecting plasma surface can be observed in b) and e) at $\sim 140\,mJ$ pulse energy. With $\sim 300\,mJ$ on target the pre-plasma gets turbulent and the harmonic structure shows very strong distortions as presented in c) and f).

strong rise towards lower wavelengths stemming from an intense line radiation background. An intermediate case is shown in figure 5.4 b) and e) with a laser pulse energy of $\sim 140\,mJ$ on the target. For this shot, the spectrometer was mounted directly in the harmonic beam, hence the additional gold mirror was not used. The wavelength range seen by the CCD camera on the spectrometer was chosen such that the cut-off of the Al filter at $17\,nm$ could be observed. The raw image in figure 5.4 b) shows a structure that has features of both of the cases described before. Distinct harmonic peaks are visible but every harmonic peak also possesses a small side peak. The structure, while still well defined, is a clear transition from the tidy spectrum in figure 5.4 a) and d) to the more chaotic case in figure 5.4 c) and f). Looking at the spectrum of this transitional state in figure 5.4 e) reveals another peculiar feature of this case. The harmonic spectrum shows a slow modulation of the harmonic peaks, where the side peaks become stronger, exceeding the main peaks at a certain point and then decline again. The modulation of the harmonic spectrum can be explained by the dynamics of the plasma surface [127, 128]. In case of a longer pre-plasma, the reflecting surface moves over time due to the ponderomotive force of the laser and hence the reflected attosecond pulses are no longer perfectly equidistant in time. This, in turn, leads to a modulation of the observed harmonic spectrum similar to the case

of CWE harmonics as explained in section 3.1 [127]. For the high-intensity case, where the harmonic spectrum is strongly distorted, an additional effect plays a role. When the pre-plasma expands long enough, it will at some point get turbulent, and instabilities form [113, 138]. As pulses generated on these instabilities have different pathlengths to the spectrometer, they will not perfectly interfere to form a nice harmonic spectrum but rather form a spectrum similar to the one shown in figure 5.4 f).

Since these instabilities form a rough surface, the incoming laser beam is not specularly reflected but scattered into a large solid angle. This can be directly observed by removing the gold mirror from the beam path allowing the observation of the XUV beam-profiles with the MCP. The beam-profile in figure 5.5 a) is taken with a laser energy on the target of $\sim 320\,mJ$. No clear XUV beam-profile can be observed except a cloudy distribution of the XUV over the detector. This is exactly what is expected from the generation of the attosecond pulses on a rough, unstable plasma surface. In contrast, figure 5.5 b) shows the XUV foot-print of the generated harmonic radiation when the driving laser energy is reduced to $\sim 85\,mJ$ on the target. A clear, although elongated, beam-profile is observed as expected from a specular reflection off a plane surface. The generation of a clean harmonic beam is especially important for applications and hence for the experiments discussed in chapter 6. Furthermore, the measurements of the efficiency using the calibrated photo-diode can only be reliably evaluated when the emission characteristic and hence the fraction of the generated XUV intercepted by the diode is known. Therefore in all the following experiments, reduced laser pulse energies close to $\sim 100\,mJ$ on the target are used to assure reproducible emission characteristics.

The measurement of the efficiency of the ROM process is performed by moving the calibrated photo-diode into the beam. An image of a beam-profile with inserted diode is shown in figure 5.5 c). In order to be able to calculate the energy in the full XUV beam, the fraction of the energy that hits the diode has to be determined. The simultaneously measured beam-profile of the MCP is used for this task, but the gap in the data left by the shadow of the calibrated diode and its holder and the beam part lying outside the active MCP area have to be retrieved. This is achieved by applying a 2D-curve fitting algorithm in MATLAB to the image, using a quadratic polynomial. The result of the fit for the data of figure 5.5 c) is shown in figure 5.5 d). This method has been applied to 10 images in order to get limited statistics on the measurement. The fit has also been verified by a second method where the data is completed by hand and subsequently smoothed by an algorithm. The two methods agree to within $< 1\%$. On the fitted data, the contour where the intensity of the signal drops below half of the maximum value can be determined and then fit to an ellipse to quantify the elongation of the beam as well as its tilt. The mean rotation of the harmonic beam from the horizontal plane is $\alpha_{tilt} = 17° \pm 4.0°$. What is of more interest
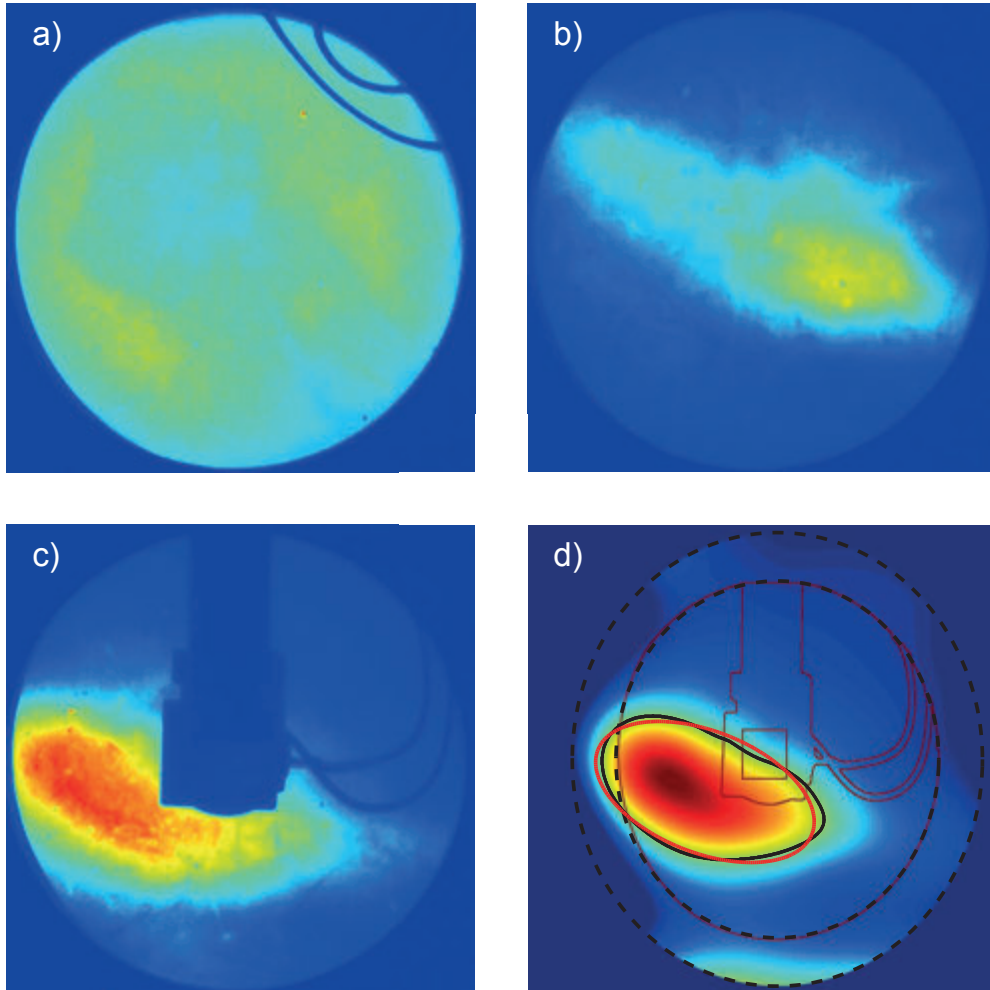
Figure 5.5.: Images of beam-profiles measured with the MCP. In a) the XUV emission goes into a wide solid angle for a pulse energy of $\sim 300\,mJ$. At reduced pulse energies of $\sim 85\,mJ$ beamed emission is observed, shown in b). c) shows a sample shot with the calibrated diode moved into the beam. In d) the retrieved beam-profile by 2D surface fitting of the shot presented in c) is shown. The position of the edge of the MCP, the calibrated diode and its holder are indicated. The half maximum contour (black) of the beam-profile and the corresponding fitted ellipse (red) are plotted.

is the divergence of the beam. The major and minor axis of the ellipse have an average length of $l_{major} = (33 \pm 4.2)\,mm$ and $l_{minor} = (13 \pm 2.4)\,mm$ respectively. This corresponds, using the distance of $750\,mm$ of the MCP from the target, to divergences of $\theta_{major} = (44 \pm 5.6)\,mrad$ and $\theta_{minor} = (17 \pm 3.2)\,mrad$, respectively. The divergence of the small axis agrees perfectly with previous measurements of Dromey et al. [125] where values of $\sim 19\,mrad$ for slightly higher laser intensities have been measured.

Several effects can lead to the observed elongation of the harmonic beam-profile. Residual astigmatism in the focusing laser beam caused by imperfect alignment of the focusing parabola or other focusing optical elements in the beam path can lead to a similar effect. Due to the monitoring of the laser focus with high resolution, this explanation can be ruled out. Additionally, the astigmatisms changes its direction by 90° when scanning through the focus. Accordingly, the direction of the XUV beam on the MCP also has to change its direction when the target was moved along the laser direction through the focus, which was not observed. The direction of the elongation was constant over all days of the measurements, although the alignment of the parabolic mirror was checked and corrected at least once per day, hence the residual astigmatism is supposed to change slightly after these checks and therefore also cause a change in the elongation of the XUV. Higher order aberrations in the laser beam are also able to cause a behaviour similar to the one observed here. Although this can not be fully ruled out, two conditions speak against it. A spatial filter and an adaptive mirror are built into the ATLAS to generate a nice wavefront of the laser beam and remove higher order aberrations. Additionally, any strong aberration of the beam is observable by the high resolution focus diagnostic in the experimental chamber. A distortion of the beam that is not observable by this diagnostic is the so-called pulsefront tilt [143], already described in section 3.3. A laser pulse with a tilted pulsefront has a rotating wavefront in the focus and hence effectively a varying angle of incidence over the duration of the laser pulse. This means, that the attosecond pulses of each cycle are emitted into a slightly different direction. During the duration of the laser pulse the emission thus sweeps over a certain angle, given by the rotation velocity of the wavefront. In the direction of this sweep, the beam therefore has an elongated shape, similar to the XUV profiles observed here, with a long axis defined by the pulsefront tilt and a small axis given by the divergence of the harmonic beam. In the measurements described here, the beam would have to sweep over a distance of $l_{sweep} = l_{major} - l_{minor} \simeq (20 \pm 4.1)\,mm$ at the position of the MCP during the duration of $\tau_{laser} \simeq 30\,fs$ of the laser pulse, corresponding to an angle of $\theta_{sweep} = (27 \pm 5.4)\,mrad$. Using the formulations of Pretzler et al. [143] and Vincenti and Quéré [141] the amount of pulsefront tilt needed for such a sweep can be calculated. The pulsefront tilt ξ is related to the

angular chirp C_a by

$$C_a = \left| \left(\frac{d\phi}{d\lambda} \right)_{\lambda_0} \right| = \frac{1}{\lambda_0} \tan(c\xi) \tag{5.1}$$

with λ_0 being the central frequency of the laser pulse. The rotation velocity v_r of the electric field in the focus and accordingly the change of the emission angle β over time is then given by

$$v_r = \frac{d\beta}{dt} = \frac{w_i^2}{f\tau_{laser}^2} \frac{\xi}{1 + (\frac{w_i\xi}{\tau_{laser}})^2}. \tag{5.2}$$

Here w_i is the beam diameter before focusing, and $w_i = 80\,mm$ for ATLAS. Finally, f is the focal length of the focusing optic, with $f = 200\,mm$ in this setup. The resulting rotation velocity in dependence of the angular chirp is shown in figure 5.6 a). The corresponding angle that is covered during the sweep is shown in figure 5.6 b) as a function of the angular chirp. From this graph it can be seen that for a sweep over $\sim 27\,mrad$ an angular chirp of only $\sim 0.01\,\frac{\mu m}{nm}$ within the laser beam is needed. At the ATLAS, with its compressor consisting of large gratings, a slight misalignment of these gratings is able to introduce an angular chirp on this order of magnitude [154]. The influence of the angular chirp on the focus can also be calculated. The relation between the chirped beam waist w_f and the intrinsic beam waist w_0 is given by

$$\frac{w_f}{w_0} = \sqrt{1 + \left(\frac{w_i f}{\tau_{laser}} \right)^2}. \tag{5.3}$$

This relation is shown in figure 5.6 c), and it can be seen that for an angular chirp as small as $0.01\,\frac{\mu m}{nm}$, the two axis of the focus are of almost equal size and can not be distinguished by the focus diagnostic used in this experiment. Hence a small amount of angular chirp is a viable candidate for explaining the observed elongated XUV beam-profiles.

Although the 2D fit gives important information for the determination of the divergence of the harmonic beam, its main use is the retrieval of the fraction of the beam that is intercepted by the absolutely calibrated photo diode. Again 10 shots are evaluated and deliver a fraction of the harmonic intensity on the diode of $F_D = (3.2 \pm 0.28)\%$. The generated charge within the diode Q_D can be calculated by integration of the background corrected data of the oscilloscope (see figure 5.7) which is then divided by the resistance of $R = 1000\,\Omega$. Evaluating the diode data of the 10 shots corresponding to the evaluated data of the MCP images gives a charge of $Q_D = (3.1 \pm 0.54) \times 10^{-9}\,C$, which is equivalent to $N_e = (1.9 \pm 0.34) \times 10^9$ electrons. This number of electrons has to be distributed over the harmonic spectrum. For this purpose, a spectrum spanning the transmission window of the used
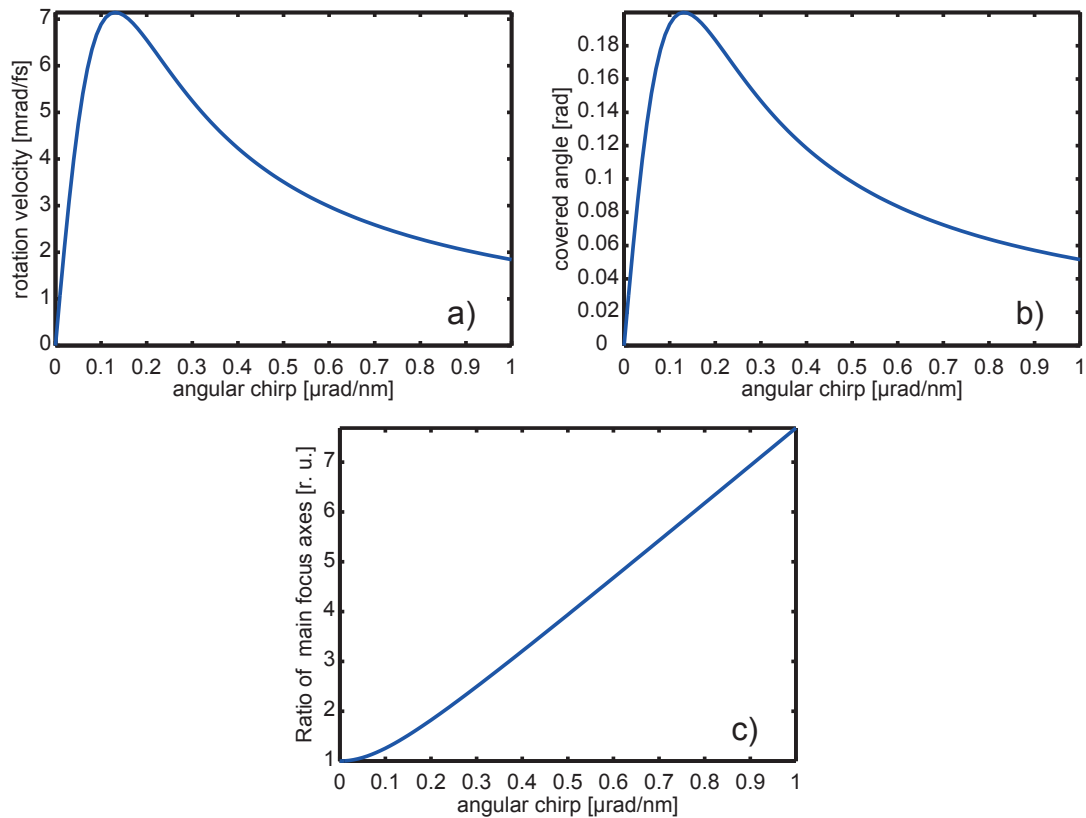
Figure 5.6.: Influence of angular chirp on a laser pulse with $28\,fs$ duration and a central wavelength of $800\,nm$. The rotation velocity of the electric field in the focus in dependence of the angular chirp of the pulse is plotted in a) for a $f = 200\,mm$ focusing optic. The corresponding angle that is covered by the emission is plotted in b). In c) the influence of the angular chirp on the proportion of the two main focal axes is shown.
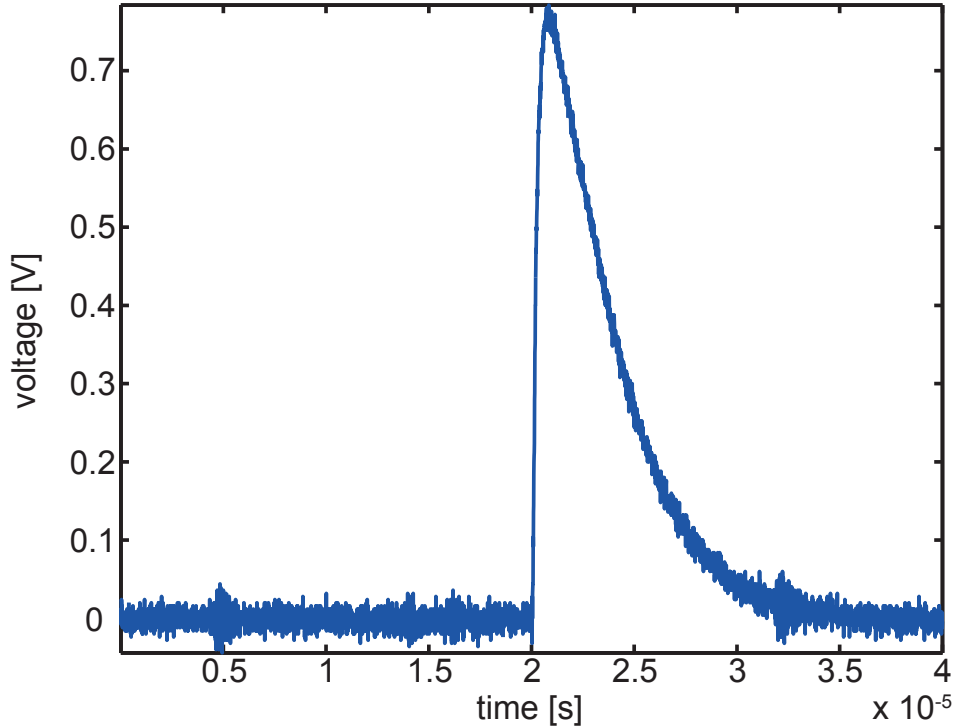
Figure 5.7.: Measured, background corrected, single shot voltage output over time of the absolutely calibrated photo diode. The integral, together with the resistance, gives the generated charge.

Al filter is generated by combining two single shot spectra, since the spectrometer is not able to record the whole spectral region within one shot. To reconstruct the harmonic spectrum generated at the target $d\Phi_T(\lambda)/d\lambda$, the combined spectrum has to be corrected for the transmission and quantum efficiencies of the parts in the beam path, which are shown in figure 5.9. In detail, these are the transmission of the Al filter [155], including a 10 nm Al_2O_3 oxide layer, which is considered for every Al filter throughout this thesis, the quantum efficiency of the CCD camera on the spectrometer (Andor DO440 BN) [156], the reflectivity of the gold mirror and the efficiency of the gold grating. Especially the last two calibrations are problematic. The gold grating has been studied in detail in previous measurements [157] but only up to 40 nm, and data at longer wavelengths is not available. The available data shows a slow increase in diffraction efficiency from 40 nm to 12 nm, from $\sim 8\%$ to $\sim 24\%$. This slow increase only effects the very high harmonics carrying a negligible amount of energy, and the efficiency for longer wavelength is assumed to be almost constant, judging from the reflectivity of a bare gold mirror. The correction for the efficiency of the gold grating is therefore omitted, because the resulting error introduced in the analysis is negligible
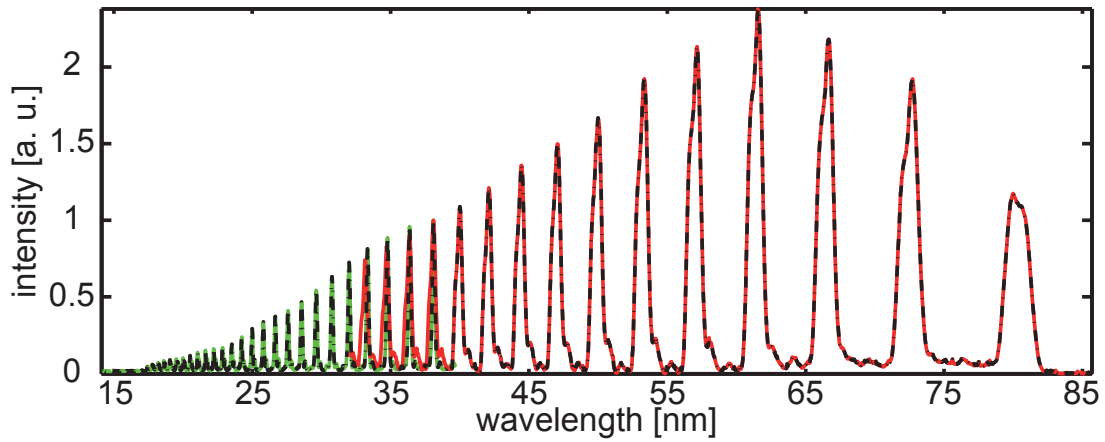
Figure 5.8.: Two single shot harmonic spectra (red) and (green) are combined into a single spectrum (black) that covers the transmission window of an Al filter.
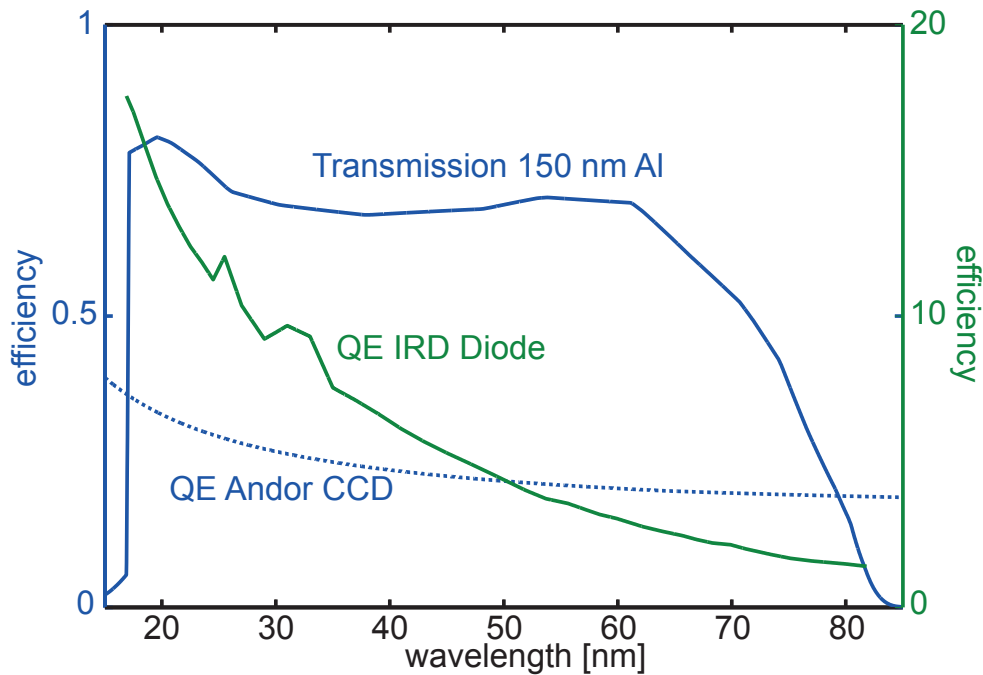

Figure 5.9.: The transmission efficiency of a $150\,nm$ thin-foil Al filter (solid blue), the quantum efficiency of the Andor CCD camera (dotted blue) mounted on the spectrometer and the quantum efficiency of the absolutely calibrated XUV diode (green) are plotted against wavelength.

compared to the other measurement errors. The reflectivity of the gold mirror used for coupling the harmonic beam into the spectrometer is almost as hard to obtain, since no data about the coating, the surface roughness and so forth is available. Because no one-to-one correspondence of the measured spectra to the measured beam-profiles is possible, there is an easy solution for this problem. Two spectra of a different experimental run with comparable laser parameters are used where the spectrometer is mounted directly in the harmonic beam coming off of the target (see chapter 6). Hence no correction for the reflectivity of the gold mirror is needed. To verify the applicability of these spectra they are compared to the ones measured in the course of the experiments discussed in this section and reveal no significant difference in the harmonic shape (compare figure 5.4 a) and figure 5.8). Let now $d\Phi_T(\lambda)/d\lambda$ be the total harmonic radiance integrated over time per unit wavelength $[J/nm]$ emitted by the target. This corresponds to a measured spectrum by the spectrometer corrected for the transmission of the applied Al filter $T_{Al}(d_2, \lambda)$ of thickness $d_2 = 150\,nm$ and the quantum efficiency of the CCD camera QE_{cam} i.e., $d\Phi_S(\lambda)/d\lambda = QE_{cam}(\lambda) \cdot T_{Al}(d_2, \lambda) \cdot d\Phi_T(\lambda)/d\lambda$, which is in arbitrary units. However, based on the measured total number of electrons N_e that this radiance induces on the photo diode, $d\Phi_T(\lambda)/d\lambda$ can be absolutely calibrated. This is accomplished through the relation:

$$N_e = C \cdot F_D \cdot \int \frac{QE_D(\lambda) \cdot T_{Al}(d_1, \lambda)}{E_p(\lambda)} \frac{d\Phi_T(\lambda)}{d\lambda} d\lambda, \qquad (5.4)$$

where C is the calibration constant, F_D the fraction of the harmonic intensity intercepted by the photo diode, $QE_D(\lambda)$ its quantum efficiency [158], $T_{Al}(d_1, \lambda)$ the transmission of the Al filter of thickness $d_1 = 1250\,nm$ used in front of the photo diode, and $E_p(\lambda)$ the photon energy corresponding to wavelength λ. From equation (5.4) the calibration constant C can be determined and subsequently the absolutely calibrated spectrum $d\Phi_T^0(\lambda)/d\lambda = C \cdot d\Phi_T(\lambda)/d\lambda$ can be obtained. The total energy in the emitted spectrum can now be readily calculated from the relation:

$$E_{XUV} = \int \frac{d\Phi_T^0(\lambda)}{d\lambda} d\lambda \qquad (5.5)$$

and accordingly the efficiency in the specified spectral range from

$$\eta_{XUV} = \frac{E_{XUV}}{E_L}. \qquad (5.6)$$

The laser energy on the target used for the 10 evaluated shots is $E_{laser} = (81 \pm 16)mJ$. The relatively large error of the laser energy stems not from large shot-to-shot fluctuations of the laser but from a drift of the laser energy over the course of the experiments. This results in a conversion efficiency of laser energy into harmonic radiation in the spectral region from $\sim 80\,nm$ to $\sim 17\,nm$ of

$\eta_{XUV} = (2.3 \pm 0.65) \times 10^{-4}$. But this still includes an instrumental factor not considered up to now. As described in section 5.2 the focusing of the laser is not perfect, and only $\sim 63\%$ of the laser energy is focused within the first Airy disc. Hence only this fraction of the laser energy gives substantial contribution to the measured spectra. Considering this effect results in a conversion efficiency of $\eta_{XUV} = (3.7 \pm 1.0) \times 10^{-4}$.

Comparisons of this efficiency to published predictions of models and simulations, e. g., in Tsakiris *et al.* [66] $\eta_{XUV} = 2 \times 10^{-3}$ for $a_0 = 2.5$, show a big difference. But as mentioned before, the exact parameters of the interaction, like laser pulse length and scale length of the pre-plasma, are expected to strongly influence the efficiency of the ROM process. Since the scale length of the pre-plasma is unknown, 1D PIC simulations for different scale lengths have been performed for the laser intensity and pulse length of the described experiments (see figure 5.10 a). Additionally the influence of the laser pulse energy has been studied (see figure 5.10 b). Interestingly, the dependency on the scale length appears to be smaller than expected and particularly does not show a strong decay of the efficiency towards longer scale lengths. It has to be noted though, that the plasma surface in a 1D simulation is intrinsically smooth and effects of turbulences and instabilities are neglected. The experimentally retrieved efficiencies are about a factor of 5 lower than the ones obtained from simulations. The lack of 2 dimensions in the simulations can explain this deviation. Higher dimensional effects of the interaction, like denting of the surface that will have an influence on the efficiency of the process are not included in the performed 1D simulation. The simulations also do not consider the intensity distribution in the focal spot of the laser, but are only performed at one specific intensity value per simulation. To correct this simplification the obtained efficiencies of the simulations for various normalized vector potentials shown in figure 5.10 b), have been fitted to determine the efficiency as a function of the laser intensity. The energy distribution in the focus of the laser has been modelled by a double Gaussian profile closely resembling the measured encircled energy fraction shown in figure 5.2 b). From this modelled distribution the normalized vector potential as a function of the radius is calculated. Using now the obtained function $\eta_{XUV} = 2.5 \times 10^{-4} a_0^{3.53}$ of the efficiency on the normalized vector potential the conversion efficiency can be expressed as a function of the radius. By $\langle \eta_{XUV} \rangle_{focus} = \int \eta_{XUV}(r) I_L(r) r dr / \int I_L(r) r dr$ the average conversion efficiency within the focal spot is calculated. The blue solid line in figure 5.10 b) shows the result of this calculation for various averaged normalized vector potentials. The correction to the initial results of the 1D PIC simulations is small, which justifies the use of averaged intensities in these kinds of simulations.

In the spatial domain, harmonics are only emitted within the first Airy minimum. Assuming a similar behaviour in the temporal domain, i. e., efficient attosecond pulse generation happens only for cycles with an intensity larger
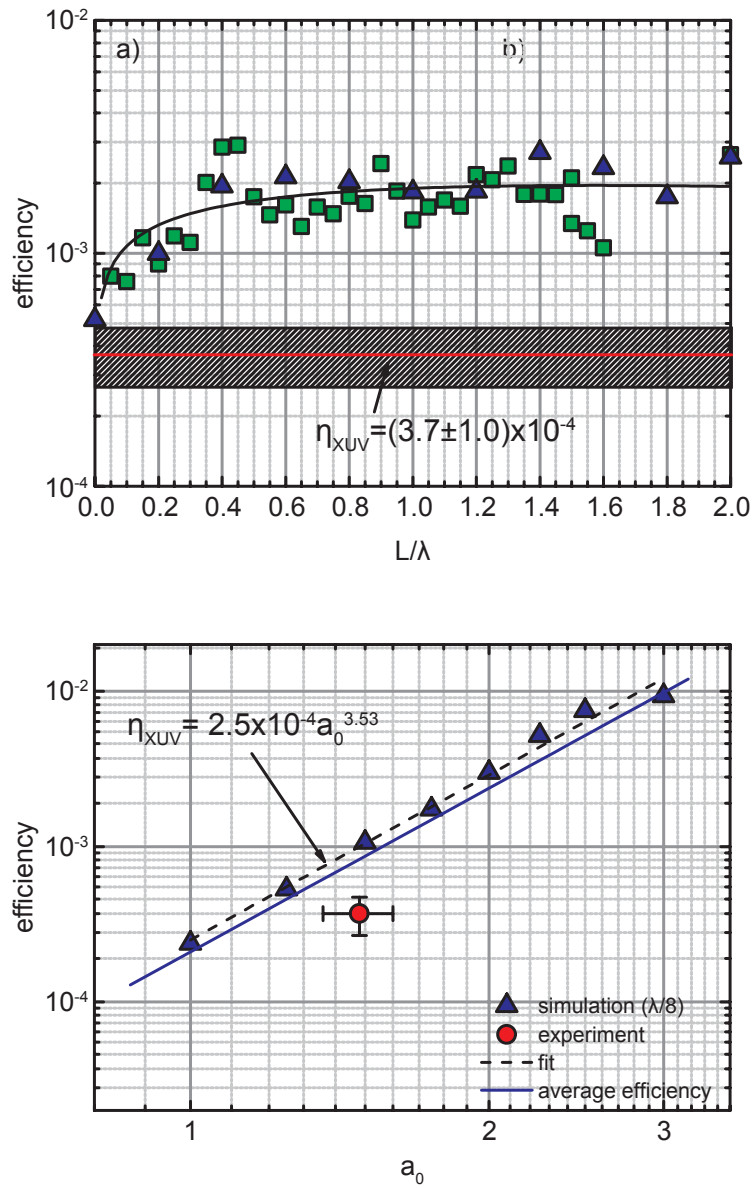
Figure 5.10.: Results of 1D PIC simulations. In a) the conversion efficiency is plotted against the pre-plasma scale length. The blue data points are simulations performed with more particles per cell than the green data point to exclude effects of truncation. The red line shows the measured value for the efficiency with the error given as a black box. The conversion efficiency (blue triangles) as a function of the laser intensity for a scale length of $\lambda/8$ is shown in b). A fit (black, dashed line) is performed on the data to calculate the correction for the use of average intensities (blue line). The red dot indicates the measured value with error bars.

than $\frac{1}{e}$ of the peak, results in an attosecond pulse train consisting of ~ 13 attosecond pulses. With an average pulse energy of the individual pulses of $E_{Pulse} \simeq 1.5\,\mu J$, these pulses are hence orders of magnitude more intense than pulses generated in gaseous media [38] and intense enough for application in pump-probe-experiments.

6. Focusing of Harmonics and Two-Photon Above-Threshold Ionization

With the demonstration of the possibility to generate a single attosecond pulse in chapter 4 and the proof of a beamed emission with high conversion efficiency of these pulses in chapter 5, it is now expedient to think about the full characterization of the pulses in the temporal domain and their application. The design and assembly of a dedicated beam-line for these purposes comprised the majority of the work leading to this thesis.

Most materials have a very low reflectivity in the spectral region of interest, i.e., for wavelengths smaller than $100\,nm$, because their index of refraction has a value smaller than 1. Such a small index of refraction also means that refractive optics, e.g., lenses, are not available and only reflective optics can be used for focusing a broad bandwidth. To achieve a high reflectivity over this broad bandwidth, the optics have to be used in a grazing incidence geometry, i.e., at a very high angle of incidence.

A similar problem is the choice of a non-linear material for the temporal characterization. In the optical devices, like second-order, third-order auto-correlators or FROG devices, that were already mentioned in previous chapters, non-linear crystals are used to generate the second- or third-order signal. Due to the lack of analogous solid-state non-linear materials in the XUV, multi-photon ionization processes in gases are used to temporally characterize bursts of light in this wavelength range. This results in the measurement of charged particles rather than photons.

Two-XUV-photon ionization induced by a superposition of harmonics generated in gases has already been observed [46, 159, 160] and was used in second-order intensity volume auto-correlation measurements to directly visualize XUV pulse trains [47, 48, 161, 162]. Further development led to the characterization of pulse trains by energy resolved [51, 163] as well as interferometric [164] second-order auto-correlation measurements. Recent XUV-pump-XUV-probe measurements using isolated XUV pulses with durations of $\sim 1\,fs$ [53] based on interferometric polarization gating [38, 144] open a new field of studies of dynamics on attosecond time scales. High harmonics from solid surfaces have unique features

making them the ideal tool for these kind of studies. CWE harmonics have already been exploited in an intensity volume auto-correlation measurement and proved the phase-locking of the harmonics [49]. But ROM harmonics with their superior phase properties [93, 123] and higher intensities are the tool of choice for such kinds of experiments. The phase properties of the harmonics are not accessible, by second-order auto-correlation techniques, which only provide an acceptable estimation of the pulse duration. Advanced techniques like FROG- [77] or SPIDER-(Spectral Phase Interferometry for Direct Electric field Reconstruction)-type [165, 166] measurements are needed to gain insight into the spectral phase of the XUV radiation. The SPIDER approach is a cross-correlation technique that requires two pulses that are spectrally slightly displaced but in other respects identical, which is difficult to achieve in the XUV. A FROG-type approach has the advantage that it is just a refinement of the second-order auto-correlation technique with additional energy resolved detection of the interaction products. This allows one to attain full spectral phase retrieval of the pulse and together with the spectral amplitude distribution, results in complete reconstruction of the pulse profile. In the XUV, this involves the energy resolved measurement of photo electrons that are generated by a two-photon process. A FROG-type measurement in the XUV using a single harmonic at $\lambda \approx 160\ nm$ has already been carried out [167]. Extending this approach to a broad XUV spectrum will bring considerable benefits for attosecond metrology.

In this chapter, the first measurement of photo electron spectra produced by a two-photon process triggered by harmonics generated by the ROM mechanism will be presented in section 6.3. This is a very promising step towards a full temporal characterization of this source of ultra-short bursts of light. A very important aspect for these measurements is the intensity of the XUV in the interaction volume. Hence, a thorough investigation of the focused XUV radiation is done in section 6.2. But first, the new XUV beam-line is discussed in section 6.1.

6.1. Experimental Setup

The experiments in this chapter were conducted with the ATLAS as a driving laser with reduced pulse energy as per the findings of chapter 5. The focusing parabolic mirror and the target mechanism are the same as in chapter 5. It is important to mention that the 5 degrees of freedom (translation in x, y and z as well as tip and tilt) of the focusing parabolic mirror are adjustable by computer-controlled stepper motors. Additionally all the flat mirrors before the focusing optic are motorized and computer-controlled. Hence with camera-controlled alignment-marks, full control over position and pointing of the focused beam is achieved. The flat-field spectrometer of chapter 5 is used again but this time is mounted directly in the harmonic beam emitted off of the target, without

the need for a coupling mirror (see figure 6.1). It is used to characterize the generated harmonics and find the optimum experimental parameters, i.e., set the position of the target in focus and tune the DAZZLER settings and laser energy to achieve best performance. After the harmonic spectrum is optimized a specially designed 135° off-axis parabolic mirror, with a surface quality better than $100\,nm$ and a micro-roughness smaller than $0.5\,nm$, is moved into the harmonic beam by means of motorized, computer-controlled stages. For this optic, too, all 5 free degrees of freedom are motorized and computer-controlled and hence make on-line adjustment during the experiments possible. The high off-axis angle is chosen to gain high reflectivity over a broad bandwidth in the spectral region of interest from $\sim 100\,nm$ down to $\sim 15\,nm$. The high angle of incidence makes it possible to use the fused silica parabola without any special coating but nevertheless still have a high reflectivity. A bare, uncoated mirror has the advantage that its laser induced damage threshold, i.e., the laser intensity it can withstand before getting irreversibly damaged, is very high. This allows the placement of the mirror very close to the source and hence reduces the necessary size of the optic to collect a substantial part of the beam. The off-axis parabolic mirror here has an effective focal length of $135\,mm$ and a clear aperture of $50\,mm$.

After the 135° off-axis parabolic mirror the well collimated beam is steered into a newly set up circular vacuum chamber. Here the beam hits two plane, bare Si mirrors (surface quality $\sim 15nm$, micro-roughness better than $0.5nm$). The angle of incidence is chosen to be 75°, corresponding to the Brewster angle for $800\,nm$ light. Hence these two mirrors are an efficient filter for the residual laser light in the harmonic beam. In theory the IR beam is suppressed by a factor of $\sim 10^5$ per plate [168], but this includes some assumptions like perfect alignment and a flawless surface. Especially the chemical degradation of the surface due to the contact with oxygen and the resulting formation of SiO_2 has a strong influence on this value. Hence, storage in an inert environment is very important. The measured suppression of the IR is $\gtrsim 50$ per plate, limited by the detector, leading to a factor of $\gtrsim 3 * 10^3$ for the IR suppression of the two mirrors. The first Si mirror is adjustable in the tip- and tilt- degrees of freedom, whereas the second mirror is mounted on a special construction. This mirror actually consist of two parts. The solid mirror is cleaved horizontally into two equally sized pieces. Along the cut no edge processing has been performed to get the sharpest edges possible and hence the lowest disturbance of the reflected beam. This split mirror serves as a full reflective beam splitter for the harmonic radiation. By shifting the lower mirror part in respect to the upper one along the surface normal, a delay can be introduced into the wave-front. The alignment of the whole unit is done by means of two stepper motors. Two additional stepper motors are used to align the lower mirror plate perfectly parallel to the upper one. With the use of a pico-motor which drives a translation stage along the surface normal of the lower mirror, a coarse alignment of the delay is done. For fine alignment and
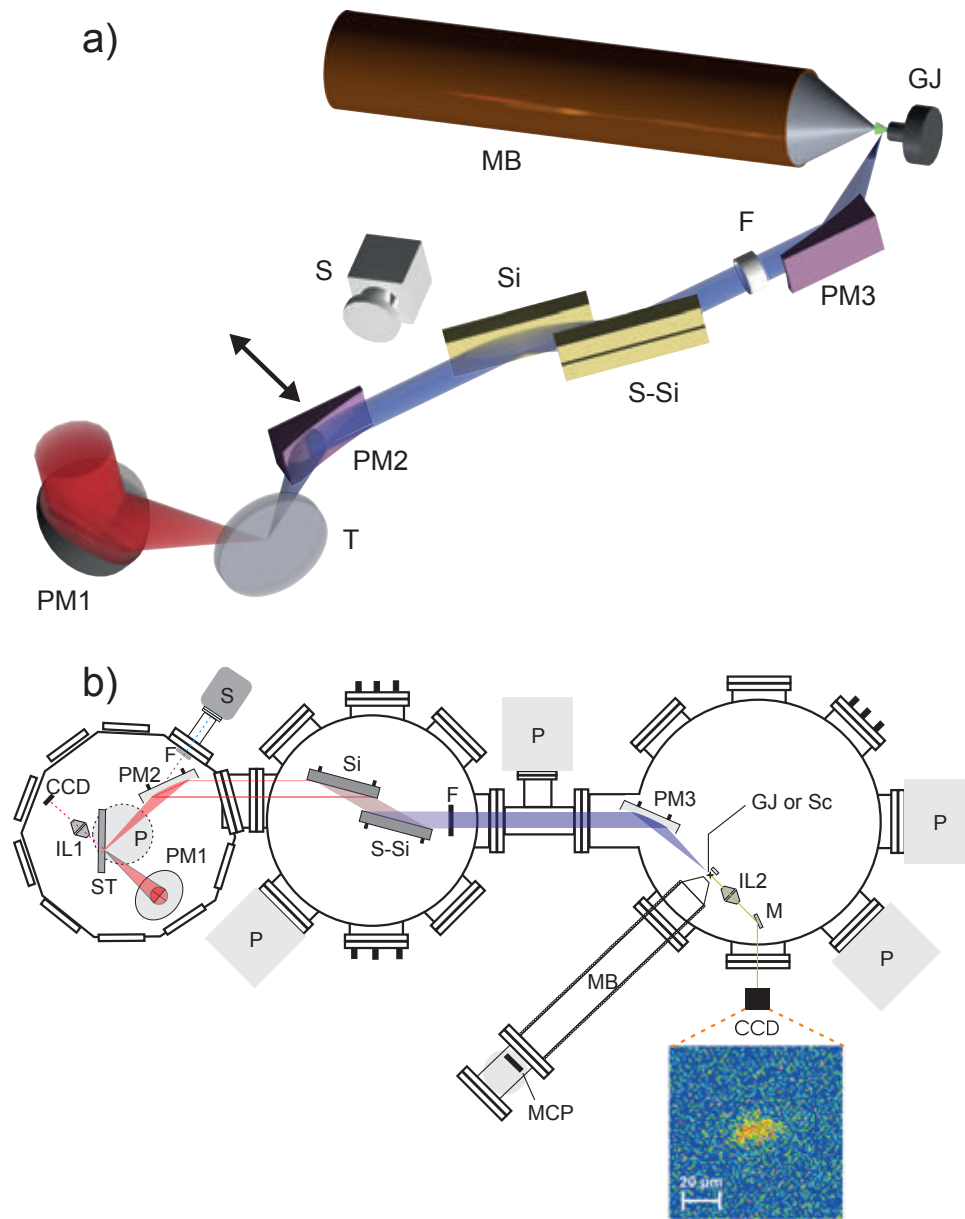
Figure 6.1.: A 3D scheme of the SHHG beam-line is shown in a), and a technical
drawing, that shows also the layout of the vacuum chambers and pumping
stages (P) is illustrated in b). The XUV beam-line consists of a 90° off-
axis parabolic mirror (PM1) to focus the IR, a fused silica target, a flat-
field spectrometer (S), a 135° off-axis recollimation parabola (PM2), a
flat Si mirror (Si), a horizontally split Si mirror (S-Si), a filter bench (F),
a focusing 130° off-axis parabola (PM3), a gas jet (GJ) in combination
with a magnetic-bottle time-of-flight spectrometer (MB) or a scintillating
crystal (SC) in combination with an imaging system (I-L) and a CCD
camera.

measurements in small steps, a piezo-drive with a closed-loop internal feedback is used, which allows for alignment on the nm-scale. In previous experiments [49], the delay unit was incorporated into the focusing optic. The separation into two discrete parts has the advantage that the introduction of a delay is not connected to the introduction of aberrations in the focus [70].

After the Si plates, the harmonic beam passes an arrangement of four flip-mounts where thin-foil filters and alignment cross-hairs are mounted before it enters another cylindrical vacuum chamber. This chamber is differentially pumped to a pressure in the low $10^{-6}\,mbar$ regime, and special care is taken to block any direct or scattered light of the driving laser from entering the chamber. A 135° off-axis parabolic mirror that is identical to the one used for collimation of the harmonic beam is used here to focus the XUV into the interaction volume.

At the focal region, a magnetic bottle electron spectrometer is placed in a horizontal geometry, perpendicular to the propagation direction of the XUV (see figure 6.1). This spectrometer consists of a pulsed gas nozzle with a permanent magnet at the very tip and a $1.5\,m$ long solenoid acting as a drift tube. The spectrometer efficiently collects photo electrons in a solid angle of $\sim 2\pi$. The gas nozzle itself acts as a repeller and it is electrically floated to be able to apply a voltage between the nozzle and the entrance of the drift tube to further increase the collection efficiency of the photo electrons generated in the jet and also to be able to measure the generated ion species. For the measurements presented in section 6.3 a voltage of $-17\,V$ was applied at the nozzle. This voltage repels electrons that initially are emitted towards the nozzle and pushes them back towards the entrance of the spectrometer. The voltage is kept at a low value in order to not reduce the energy resolution of the spectrometer. At the end of the drift tube, a MCP is mounted that is connected to a fast oscilloscope. The energy resolution of the spectrometer ($\Delta E/E \approx 3\%$) is high enough to distinguish peaks in the energy spectrum of the photo electrons, originating from the absorption of different combinations of two harmonic photons. The energy calibration of the spectrometer is done by single-photon ionization electrons of argon and is verified by the agreement of the intersection of the calibration line with the energy axis compared to the gained energy of the electrons by the applied repelling voltage.

As mentioned before, a pivotal parameter for the observation of non-linear processes is the intensity in the focal region. To get as many XUV photons as possible into the interaction region, the whole beam-line was specifically designed to have maximum throughput over the spectral region of interest, namely the transmission window of a thin-foil Al filter. The calculated transmission of the setup using tabulated data of the optical constants of the used materials that was taken from [168] and [155] is shown in figure 6.2. For almost the full bandwidth of the filter, the transmission is above 1%. This calculation also includes losses due to the surface roughness of the optics.
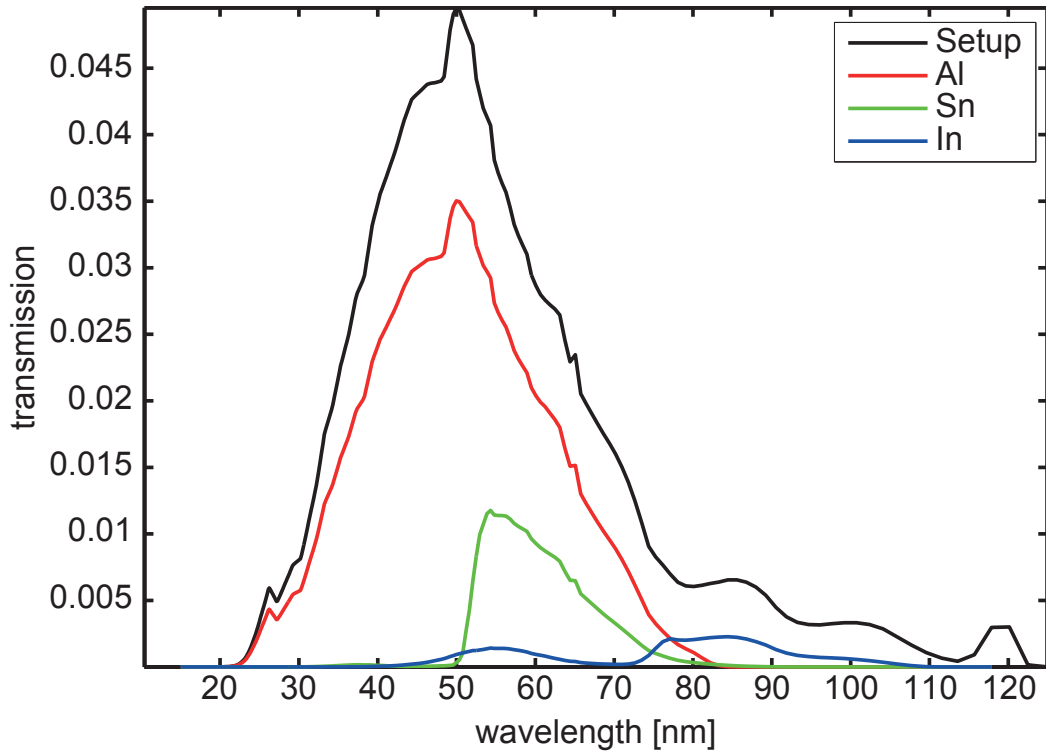
Figure 6.2.: The wavelength dependent transmission of the XUV beam-line alone
(black), as well as combined with three choices of $150\,nm$ thick thin-foil
filters, namely an Al- (red), a Sn- (green) or an In-foil (blue) is shown

The ability to focus the XUV radiation to a very small area is equally important
as the high transmission of the setup. Since the setup images the source in a one-
to-one manner into the interaction volume, a XUV spot-size on the order of the
laser focal spot is expected. The direct observation of a focal spot of this size
in the XUV spectral region is not trivial. The direct use of cameras or MCPs is
not possible since the expected spot size is on the order or even smaller than one
pixel or one channel, respectively. Hence some magnification system has to be
used. Since there are no broadband dispersive optics in the XUV spectral region,
this magnification system has to be fully reflective and is accordingly expensive
and complicated to align. An elegant solution to this problem is the conversion
of the XUV into visible light by means of a scintillating crystal. Therefore the
front side of a $100\,\mu m$ thin YAG:Ce crystal with a doping level of $0.15\,\%$ is placed
into the focus. This allows the use of standard optics for the observation of the
focal spot. A long-working-distance microscope objective is used to magnify the
spot which is then recorded with a cooled 16-bit camera resulting in a resolution
of $\sim 1\,\mu m$. To make sure, that no residual laser light reaches the camera it is
equipped with a high pass filter.

The beam-line is aligned with the laser pulse energy filtered down to a level that is insufficient to damage the fused silica target. The small part which is reflected of the target is then steered down the beam-line, and the IR focus is optimized in the interaction chamber by removing the high pass filter of the camera. The two halves of the split mirror are adjusted, and the focusing parabolic mirror is optimized. The zero delay of the split mirror can be found within one laser pulse duration by observing constructive and destructive interference in the focus. Since the IR beam is clipped on the thin-foil filter unit, the observed focal spot with a size of $\sim 5\,\mu m$ is larger than on the target. Once the alignment is done, the collimating parabolic mirror is moved out of the beam to let the generated XUV radiation enter the spectrometer. After the harmonic spectrum is optimized, the parabolic mirror is moved back into the beam, which is done with a precision on the μm scale, preserving the initial alignment.

6.2. Focusing of Harmonics

The technique of observing the focus with a scintillating crystal is meant to be used as a single shot method for two reasons. First, a multi shot method would have a reduced resolution due to fluctuations in the harmonic signal, e.g. pointing fluctuations but also spectral fluctuations. Second, the target used for the harmonic generation has only a limited size and hence the number of shots per target is limited, a solution to this problem is presented in appendix A. For the change of target, the first vacuum chamber has to be opened, which is time consuming and also slightly alters the alignment of the beam-line making a check of the alignment necessary.

In figure 6.3, three single shot images of the XUV focus are shown with different thin-foil filters placed in the beam-path. To verify that the observed signal is solely produced by XUV radiation, a glass plate is placed in the beam-path right after the thin-foil filter. The XUV is fully absorbed by this glass plate, and the signal vanishes, while the IR is transmitted, and the signal is unaltered. With the glass plated inserted no signal is observed. The foci are hence solely produced by XUV radiation. In all three images, the recorded signal is very low. This is a clear disadvantage of the single shot method and makes the use of a cooled CCD with a low background level necessary. For two Al filters with a thickness of $150\,nm$ each placed in the beam, a spot with a diameter on the order of $\sim 10\,\mu m$ surrounded by a weak halo with about $\sim 100\,\mu m$ of diameter is visible on the image. Removing one of the Al filters makes this even clearer. Both the spot and the halo gain intensity but the overall structure is preserved. Since the beam-line performs a one-to-one imaging of the source region onto the scintillating crystal, there are two sources of radiation with different dimensions. Indeed, two very different types of XUV radiation come off of the plasma. One is the
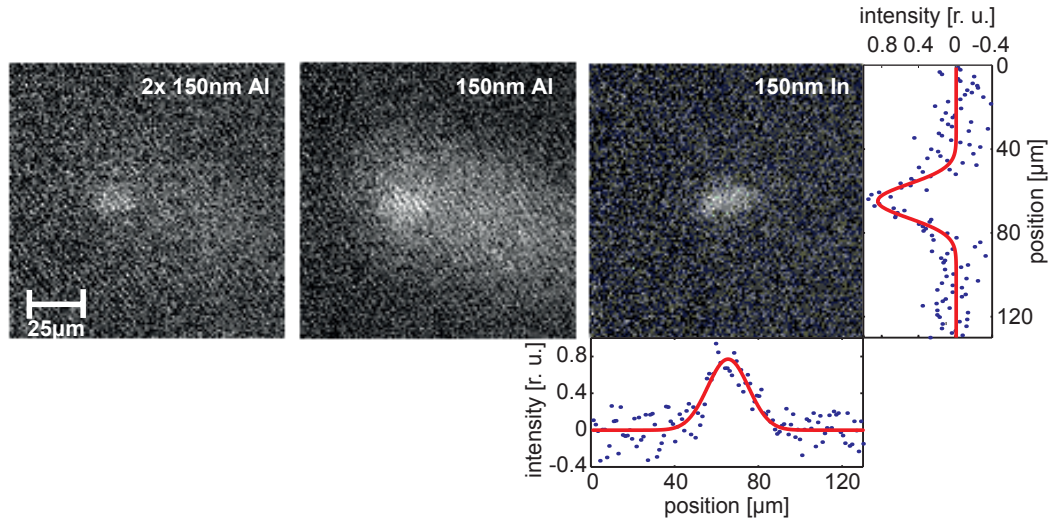
Figure 6.3.: Images of single shot XUV foci with three different thin foil filters applied
are shown. The big halo observed with Al filters is due to incoherent line
radiation. A focal spot size of $\sim 15\,\mu m$ is measured.

coherent harmonic radiation, which is emitted only during the direct interaction
of the laser pulse with the plasma and is hence localized within the focus. The
second type of emitted XUV light is incoherent plasma radiation. This type
of radiation is generated by the recombination of the separated electrons with
the ion background and is therefore emitted over much larger time scales. Also
this second type is not very localized since the plasma spreads out over time
and recombination will occur everywhere within the plasma plume. A size of
this plume on the order of $\sim 100\,\mu m$ is very likely. To test if the observed halo
really originates from the incoherent plasma background, test shots on previously
damaged target spots are performed. Although a plasma still forms, recombines
and irradiates due to the interaction of the laser pulse with a rough surface, the
generation of harmonics is efficiently suppressed. Accordingly, on the measured
images of the crystal, only the large halo is visible, while the small spot is missing.

To be able to measure the harmonic spot without the incoherent background
signal a different filter is necessary. The plasma radiation is emitted into a broad
spectral region, and a reduction of the transmitted spectral bandwidth to only
a few low order harmonics hence reduces the transmitted plasma background,
while it preserves a comparatively strong harmonic signal. An appropriate filter
material is, for example, indium (In). As can be seen in figure 6.2, it reduces the
transmitted spectral range mainly to harmonics 8, 9 and 10. A measured XUV
focal spot with a $150\,nm$ thick In thin-foil filter inserted in the beam-line is shown
in figure 6.3. The XUV focal spot is clearly visible, while the halo is completely

absent. The evaluation of the XUV focal spot size by Gaussian fits to line-outs of the recorded images yields a spot size of $d_{FWHM,ver} = 15.2 \pm 2.1\,\mu m$ [75]. The size of the spot is much larger than expected from the assumption that the area of harmonic generation, i.e. an area smaller than the laser spot of $\sim 3\,\mu m$ in diameter, is directly imaged onto the scintillating crystal. An XUV focus that is larger than expected can be produced by inaccurate alignment of the beam-line. But the pre-alignment of the beam-line with the residual IR excludes errors in focal-spot size larger than $\sim 5\,\mu m$ due to alignment issues. The source of the bigger than expected size of the measured XUV focus was rather found to be within the scintillating crystal. The minimum energy per laser pulse to saturate the crystal is $E_\gamma \approx 1 \times 10^{-8}\,J$ [169]. To calculate the focused XUV energy, the results of chapter 5 can be used. The transmission window of the In filter extends to longer wavelengths than the one of the Al filter. Hence, a direct calculation using the combined spectrum of section 5.3 is not possible, and some estimations have to be made. The part of the transmission window at longer wavelengths has a higher transmission (see figure 6.2), and the lower order harmonics carry more energy. Therefore the very conservative assumption is made that the generation and transmission efficiency of this part of the spectrum is about 1.5 times the efficiency of the short wavelength part. This assumption results in a focused XUV energy of $E_{foc} \approx 6 \times 10^{-8}\,J$. This is more than 5 times the energy needed to saturate the crystal. Also, a measurement replacing the In filter again with a $150\,nm$ Al-filter shows the saturation of the crystal. Here the focal position was moved in small steps from in front of the crystal to behind the crystal by shifting the focusing parabolic mirror and a focal spot was recorded for every step. Although the size of the focal spot changes, neither the maximum nor the averaged intensity changes during the scan which hints at a saturation of the crystal. More details of these measurements can be found in the diploma thesis of L. Waldecker [169]. Despite the saturation of the crystal, it is possible to state that a focusing of the generated harmonics into a spot size $< 16\,\mu m$ is possible. This small spot size allows the measurements presented in the next section.

6.3. Two-Photon Above-Threshold Ionization

A prerequisite for a FROG-type diagnostic of an XUV pulse is the measurement of energy resolved photo electron peaks generated by a two-photon ionization process. This is more difficult when using harmonics from surfaces than using harmonics generated in gases, since both odd harmonics and even harmonics are produced, and accordingly, more and closer spaced peaks occur. Due to the small cross-section of two-photon processes compared to single-photon events, a way of separating the two signals is needed. This can be done by the right choice of filter and target gas. In the experiments presented here, a $150\,nm$ thick tin (Sn)

foil in combination with argon (Ar) gas is used. The transmission of Sn begins at the 10th harmonic and ends at the 16th, where the transmission of the 16th is very small (see figure 6.4). The first ionization potential of Ar is $\sim 15.8\,eV$ and

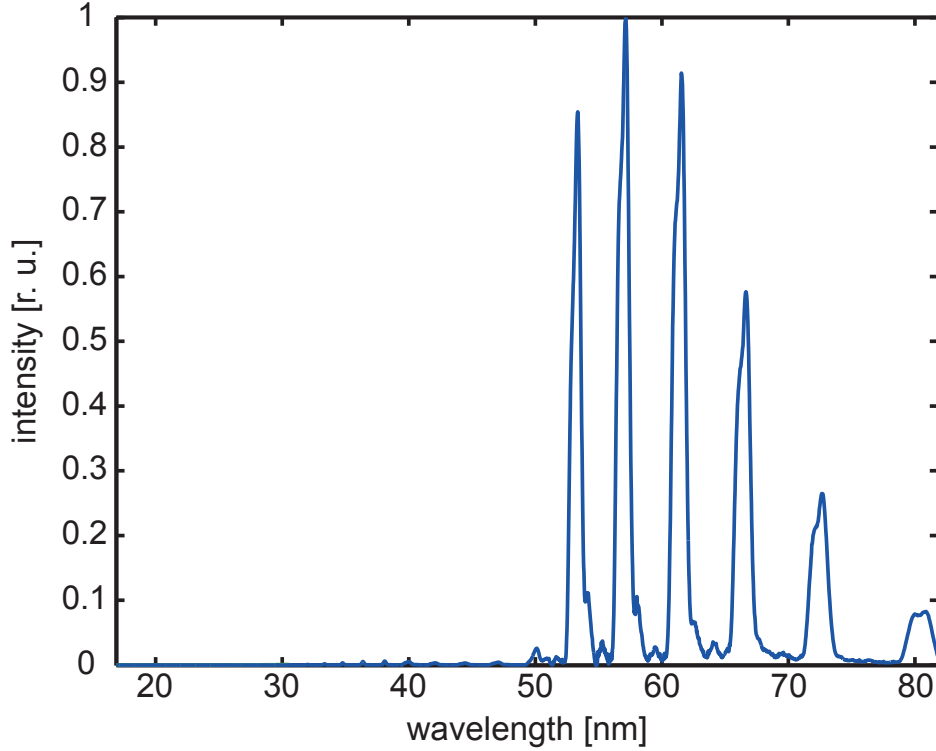**Figure 6.4.:** The spectrum that is transmitted by the XUV beam-line with an inserted $150\,nm$ thick Sn filter. Harmonic 16 at $50\,nm$ is suppressed by more than a factor of 10 compared to harmonic 14.

the second ionization potential is $\sim 43.4\,eV$. Single-photon ionization (SPI) is hence possible for harmonics 11 and higher (see figure 6.5). The effective ionizing spectrum therefore consist of harmonics 11 to 16. Absorption of one photon of these harmonics leads to SPI of Ar and a photo electron spectrum consisting of six peaks separated by the energy of one photon of the driving laser ($1.55\,eV$) at

$$E_{SPI} = n_{harm}\hbar\omega_{laser} - IP, \tag{6.1}$$

where n_{harm} is the harmonic number, ω_{laser} is the frequency of the driving laser, and IP is the first ionization potential of Ar.

If now, a second photon of the harmonic spectrum is absorbed prior to the formation of Ar ions, the electron gains additional energy and the process is called above-threshold ionization (ATI). The ATI photo electron spectrum also consists of discrete peaks that are spaced by the energy of one photon of the

driving laser at

$$E_{ATI} = (n_{harm,1} + n_{harm,2})\hbar\omega_{laser} - IP. \qquad (6.2)$$

From equation (6.1) and equation (6.2) it can be directly seen that the highest peak of the SPI spectrum is located at $16\hbar\omega_{laser} - IP$, whereas the lowest peak of the ATI spectrum is observed at $22\hbar\omega_{laser} - IP$. The two spectra are hence positioned at well separated spaces on the energy scale, and it is possible to observe the orders of magnitude lower ATI signal at the foot of the SPI spectrum. The ATI process can be a one- or two-colour effect depending on whether two photons of the same harmonic or of different harmonics are involved. The relative strength of the ATI peaks is governed, amongst other factors by the cross section of the process, the relative strength of the involved harmonics as well as by the number of reaction paths leading to this peak, because different combinations of harmonics contribute to the same peak. An ionization scheme, showing the various combinations is shown in figure 6.5. The peak at $24\hbar\omega_{laser} - IP$,
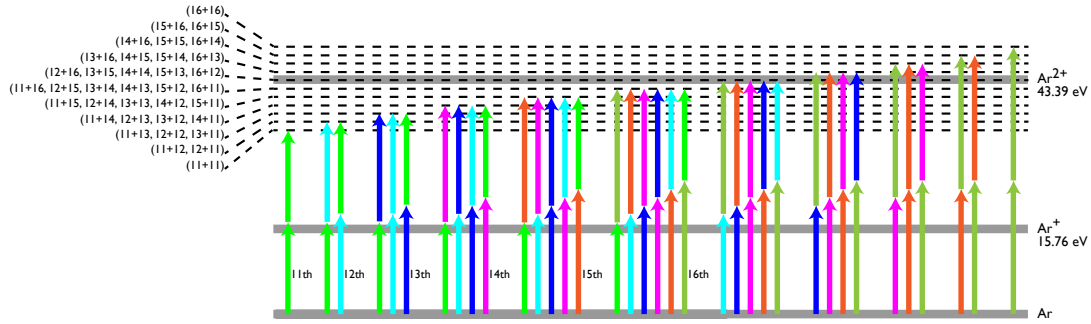
Figure 6.5.: Ionization scheme of Ar. All possible combinations of harmonic photons that contribute to the ATI peaks are displayed.

for example, can be reached by absorbing a photon of the 11th harmonic and subsequently a photon of the 13th, or by absorbing a photon of the 13th harmonic followed by the absorption of a photon of the 11th, or, as a third option, by subsequently absorbing two photons of the 12th harmonic. These are three combinations of harmonics that contribute to the ATI peak at $24\hbar\omega_{laser} - IP$, but they constitute four ionization channels. Similarly, one combination of harmonics (11th+11th) builds the lowest ATI peak at $22\hbar\omega_{laser} - IP$ and forms two ionization channels leading to this peak. Also, the highest ATI peak at $32\hbar\omega_{laser} - IP$ originates from only two ionization channels with one combination of harmonics (16th+16th). These two peaks are hence comparatively weak. The central ATI peaks at $26\hbar\omega_{laser} - IP$, $27\hbar\omega_{laser} - IP$ and $28\hbar\omega_{laser} - IP$ have 6 possible ionization channels with 6 harmonic combinations for the central one and 5 for the other two peaks, respectively. All of these interactions can be exploited in an

energy resolved second-order auto-correlation measurement which subsequently can be used as an input for a FROG-type determination of the temporal profile of the XUV emission.

In figure 6.5, it can be seen that some of the harmonic combinations provide enough energy to doubly ionize the Ar atoms through a process that is called two-photon direct double ionization (TPDDI). The low excess energy of the generated photo electrons by TPDDI is in the same range as the excess energy of electrons generated by the SPI process. Hence, these two spectra overlap. Since TPDDI is a two-photon process, it has a much lower rate then the one-photon SPI process, and hence the electrons generated by TPDDI have a negligible contribution to the photo electron spectrum. Also, sequential double ionization (SDI) plays only a negligible role for the chosen set of harmonics, because it becomes a three-photon process. A photon energy $> 27.63 eV$ is needed for the formation of doubly ionized Ar^{2+} following the formation of Ar^+, which is more than the harmonic with the highest photon energy in the chosen set can supply ($24.80\ eV$).

Having chosen the harmonic spectrum and the non-linear process, it is now interesting to estimate the amount of generated photo electrons. Using the efficiency of the ROM process measured in chapter 5 and the transmission of the XUV beam-line in combination with the Sn filter calculated in section 6.1, an overall efficiency of $\eta_{foc} \approx (1.1 \pm 0.30) \times 10^{-6}$ is obtained. The available pulse energy of ATLAS is again reduced to $E_{laser} \approx 100\ mJ$ in order to have a high XUV beam quality. This results in a focused XUV intensity within the focal spot with a diameter of $d_{foc} \approx 15 \times 10^{-6}\ m$ of $I_{foc} \approx (1.4 \pm 0.8) \times 10^{12}\ \frac{W}{cm^2}$. The photo electron yield is, according to [54], given by

$$Y_{ATI} = \sigma F^2 \tau_{pulse} n \qquad (6.3)$$

where σ is the cross section of the process given in $cm^4 s$, F is the photon flux in $\frac{photons}{cm^2 s}$, τ_{pulse} is the XUV pulse duration, and n is the number of atoms in the interaction volume. Using an average transmitted photon energy of $E_{photon} = 20.7\ eV$ corresponding to a wavelength of $\lambda = 60\ nm$, the photon flux can be calculated from the focused intensity by $F = \frac{I_{foc}}{E_{photon}} = 4 \times 10^{29}\ \frac{1}{cm^2 s}$. The pulse length is approximated to be equal to the driving laser's pulse duration $\tau_{pulse} \approx 28\ fs$, which is adequate for an order of magnitude estimation. The number of atoms n within the interaction volume V can be calculated from the atomic density within the gas jet, which is estimated to be $\rho \approx 10^{15} - 10^{16}\ \frac{1}{cm^3}$. The interaction volume itself is calculated from the size of the focus $d = 15\ \mu m$ and the length of the gas jet of $l \approx 1 mm$. The last missing factor is the interaction cross section, which is calculated by Miyamoto et al. [163] for a photon energy of $E_{photon} = 25\ eV$ to be $\sigma \approx 2.0 \times 10^{-51} cm^4 s$ and is also used for this estimation for all the harmonic combinations. Putting all of the numbers into equation (6.3) results in a photo electron yield of $Y_{ATI} \approx 2 \times 10^3$, where for the gas density the

lower value of $\rho = 10^{15}\frac{1}{cm^3}$ was taken to be on the safe side. Taking a rather underestimated value of $\eta_{col} = 0.1$ for the collection efficiency of the magnetic bottle spectrometer results in ~ 200 detected ATI photo electrons per laser shot, which should be enough to resolve the ATI peaks of Ar.

In figure 6.6 a) a measured single-shot SPI photo electron spectrum is shown. The ionizing spectrum is clearly observable and harmonics 11 to 15 are well resolved. The 16th harmonic, which has only a very low transmission through the Sn filter, is only barely visible. Determining the energy content of each harmonic by integrating the respective part of the spectrum and comparing the result to the same analysis performed on the measured flat-field spectrum (shown in figure 6.4) that was corrected for the beam-line transmission, reveals a very similar behaviour. The obtained data points are shown in figure 6.7. Both sets show a low signal at the 11th harmonic that rises to a maximum and then declines again towards the 16th harmonic. The maximum of the corrected flat-field spectrum is slightly shifted compared to the photo electron spectrum. This shift is possibly due to the difference of the theoretical transmission and reflectivity values compared to the real values, and these may deviate due to degradation or contamination of the surfaces.

The ATI signal is expected to appear in the energy range between $18\ eV$ and $40\ eV$ but with much lower signal strength than the SPI signal. A single shot spectrum with higher resolution is presented in figure 6.6 b) (black line). On the very left edge of the spectrum, the high energy tail of the SPI spectrum is still visible. The fast decay of this signal allows the observation of a peak structure with much lower intensities at higher energies. Ten peaks in the expected energy range for the ATI signal are distinguishable from the background. These peaks are spaced by $1.55\,eV$ corresponding to the energy of one driving laser photon and are situated at energies ranging from $22\hbar\omega_{laser}-IP$ to $31\hbar\omega_{laser}-IP$. These positions match perfectly with the expected spectrum of a two-photon ATI process that is triggered by combinations of harmonics 11 to 16. Because of the low transmission of the 16th harmonic through the setup, the peak at $32\hbar\omega_{laser}-IP$ corresponding to the one-colour ATI process of only the 16th harmonic is not observable. The ATI signal shows strong fluctuations in signal strength and harmonic shape from shot to shot. A spectrum averaged over 9 shots is shown in figure 6.6 b) (grey line). The ATI signal is still visible and the peak positions are conserved also in the averaged spectrum. To guide the eye, a 150 points moving average is performed on the 9 shot average spectrum and also plotted in figure 6.6 b) (red line). Again, the peaks occur at the expected positions of the ATI process that is triggered by the combination of the given harmonics.

Another proof for the two-photon nature of the observed photo electron peaks is the dependence of the integrated ATI peaks on the energy of the ionizing XUV radiation. In the current configuration of the XUV beam-line, it is not possible to simultaneously measure the harmonic signal with the flat-field spectrometer and
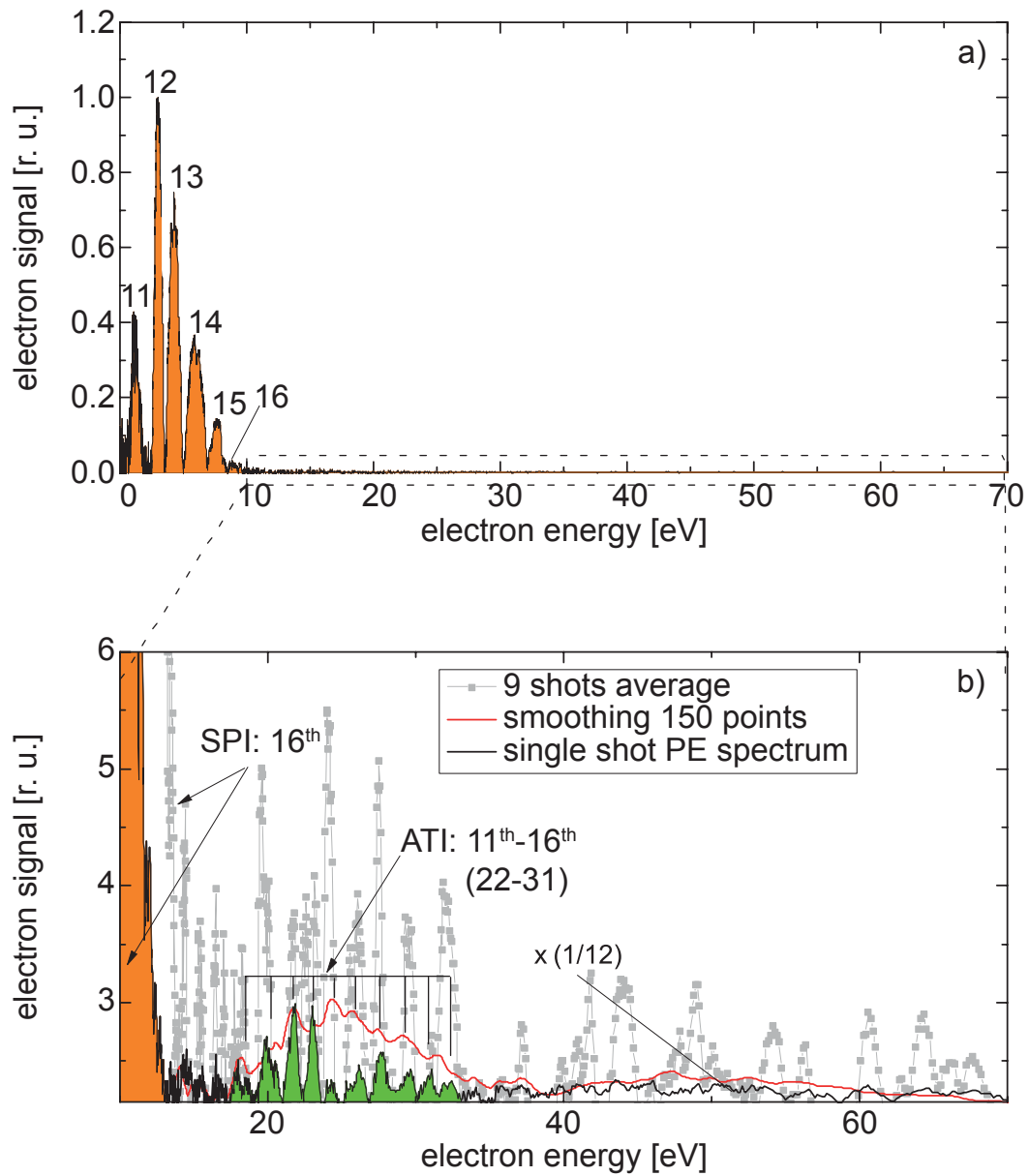
Figure 6.6.: Single- (SPI) and two-photon above-threshold ionization (ATI) spectra of Ar. In a), a background corrected single-shot SPI photo electron spectrum of Ar (black line, orange filled) is shown. b) shows a two-XUV-photon ATI spectrum of Ar. A single-shot spectrum is plotted as a black line (green filled). The grey dotted line is an average of 9 shots. The red line is obtained from the grey data by performing a 150 points moving average. The orange filled area is the high energy tail of the single-shot SPI signal.
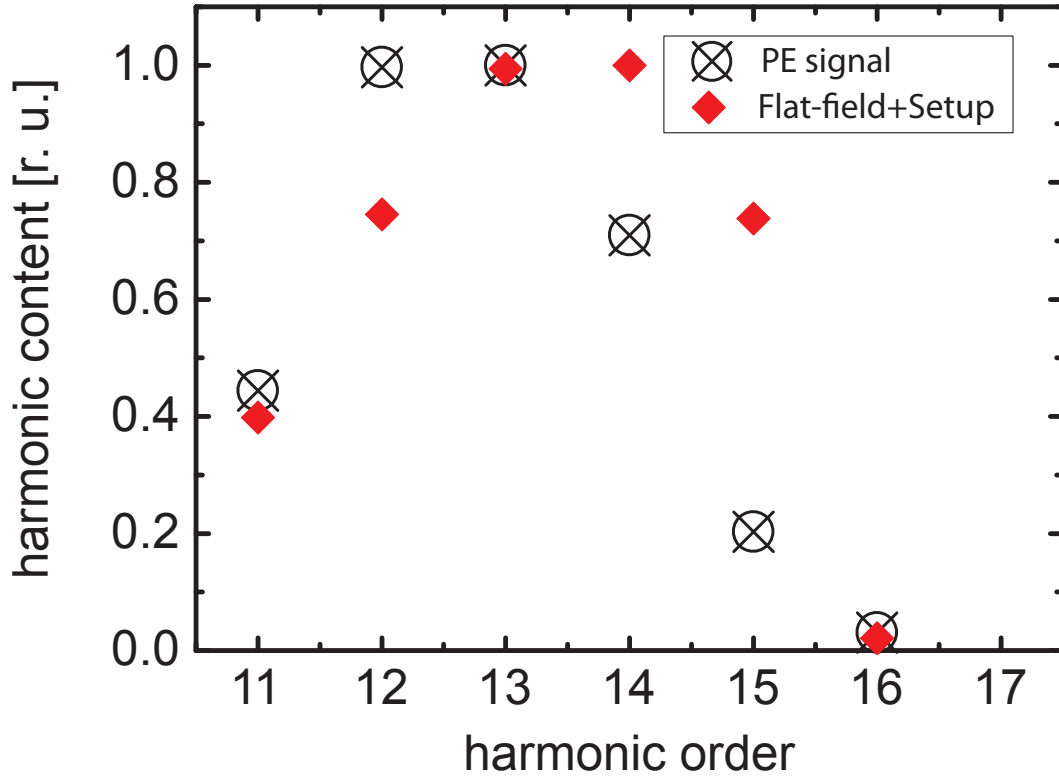
Figure 6.7.: Comparison of the corrected photon spectrum with the photo electron spectrum. The red rhombs are the integrated harmonic content of the corrected flat-field spectrum in figure 6.4. The crossed circles are the integrated harmonic content of the photo electron spectrum in figure 6.6 a).

the ATI spectrum with the magnetic bottle spectrometer. Therefore, the back reflected SPI signal is used to deduce the focused energy of the ionizing harmonic spectrum within the gas jet. In figure 6.8, the dependence of the integrated signal of the ten ATI peaks is plotted against the incident XUV energy. Due to the small signal levels, the error-bars on the data points are large. A linear fit to the log-log diagram reveals a slope of 1.7 ± 0.6. This slope complies within the error with the expected value of 2 and serves as another indication of a two-photon process.

The use of ROM harmonics for the measurement of energy resolved photo electron spectra generated by a two-photon process is a very important step towards the full temporal characterization as well as the application of these harmonics. The strong shot-to-shot fluctuations of the ATI signal, which are larger than the expected changes of the signal during a FROG-type characterization of the generated attosecond pulse train, prohibited the accomplishment of such a measurement. These fluctuations of the signal can be mostly attributed to
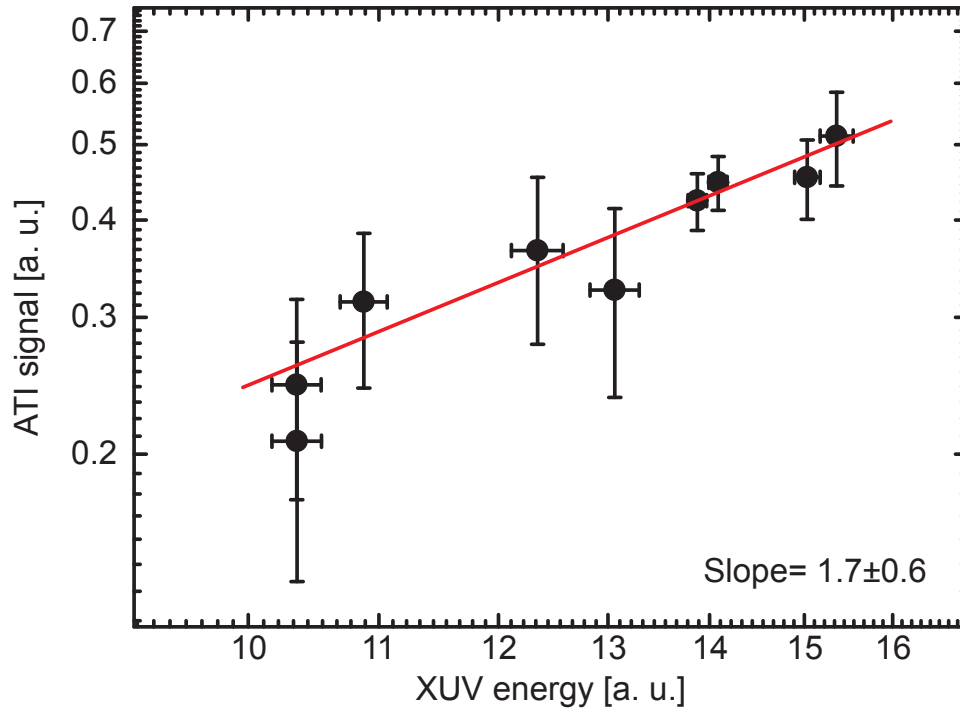
Figure 6.8.: Total ATI photo electron yield as a function of the XUV energy. The back reflected SPI photo electron signal is used as a measure for the XUV energy.

the unstable interaction of the driving laser with the target due to the imperfect contrast and associated pre-plasma conditions. The upgraded LWS-20 with its presumably superior contrast is a promising tool for such kinds of measurements.

7. Conclusions and Outlook

The experiments and results presented in this thesis give new insights into the process of relativistic high-order harmonic generation on solid surfaces. The work at hand aims at a full characterization of the temporal, spectral and spatial properties of this source as well as its conversion efficiency. The findings constitute a major step towards the application of relativistic harmonics generated on solid surfaces in XUV-XUV attosecond-pump-attosecond-probe type experiments. These kind of investigations will promote the field of attoscience to new regimes which are not accessible with state of the art attosecond pulse sources based on gaseous media.

The first demonstration of the generation of harmonic radiation off a solid surface following the ROM process driven by an intense, few-cycle laser (LWS-20) has been shown. The use of a laser pulse consisting of only 3 cycles of its electric field is very important for the applicability of this source of ultra-short bursts of light, since it allows for the generation of isolated attosecond pulsed that are a necessity for attosecond-pump-attosecond-probe type experiments without the need for additional gating techniques. Harmonics down to a wavelength of $17nm$ are reproducibly observed. The accessible wavelength range was limited by the transmission window of the applied Al filter. The harmonics show a distinct spectral broadening compared to harmonics generated with longer driving laser pulses. Since the spectral width is inversely proportional to the temporal envelope of the generated attosecond pulse train, the broadening of the harmonics leads to a strong confinement of the attosecond pulse generation. Additionally, spectral modulations of the harmonics, changing from shot to shot, are observed. These modulations can be attributed to the strong effect of the varying CEP of the driving pulse on the interaction dynamics, when using few-cycle pulses. With the varying relative instantaneous intensity of the cycles of the electric field, the dynamics of the reflecting electron layer also changes leading to an emission of an attosecond pulse train, where the individual pulses are not equally spaced in time. This can then be observed as a modulation of the harmonics in the spectral domain. Detailed analysis of the interaction with the use of 1D PIC simulations reveals this behaviour, but more importantly shows that a 3 cycle driving laser pulse is already short enough to confine the attosecond pulse emission to only a single cycle of the electric field of the laser, hence enabling the production of isolated attosecond pulses. Due to the lack of CEP stabilization in LWS-20, it is interesting to know how many of the laser shots produce a single attosecond

pulse. The 1D PIC simulation gives an answer to this question and indicates a probability as high as 17% for the generation of an isolated attosecond pulse. In the worst case, a pulse train with as many as four attosecond pulses, with a probability of 5% for this scenario, will be generated. It is also important to note, that there was no need for any external contrast improvement of the LWS-20. This system, owing to the use of the OPCPA technique, delivers pulses with an inherent and sufficient contrast that directly leads to a clean and very reproducible interaction.

In the second experimental chapter of this thesis, the first direct and unequivocal measurement of the conversion efficiency of laser energy into the high harmonic spectrum is demonstrated. At the same time, the emission of the harmonic beam into a small solid angle is shown. The use of the ATLAS, a Ti:Sapphire based system, with worse contrast properties demanded an examination of the influence of the pre-plasma. A study of the dependence of the spatial emission properties and the spectral characteristics on the laser pulse energy and hence the connected pre-plasma scale length has been performed. It is found that for a exceedingly high laser energy, the pre-plasma forms a turbulent and rough surface from which the harmonics are emitted into a wide solid angle and a distorted spectrum. For optimum interaction conditions, an elongated harmonic beam-profile was observed. The divergence of the beam is found to be $\sim 17\,mrad$ in accordance with previous publications [125]. The most likely explanation for the observed elongated harmonic beam is a small amount of angular chirp on the driving laser pulse caused by a slight misalignment of the gratings of the compressor. The simultaneous measurement of the energy content of the harmonic spectrum with a calibrated photo diode and the harmonic beam-profile facilitates the direct evaluation of the conversion efficiency. A conversion efficiency as high as $\sim 4 \times 10^{-4}$ has been found for a driving laser with an averaged normalized vector potential over the focal spot area of $a_0 \approx 1.5$. The high conversion efficiency in combination with a pulse energy of $\sim 100\,mJ$ results in an average attosecond pulse energy of $\sim 1.5\,\mu J$. This is a more than one order of magnitude higher energy per pulse compared to the attosecond pulses of highest energy generated in gaseous media with $\sim 100\,nJ$ of pulse energy [38]. Attosecond pulses of such high energies are perfect tools for the execution of XUV-pump-XUV-probe type experiments.

Driven by the findings of the first two chapters, a dedicated beam-line for the temporal characterization and application of the generated relativistic harmonics has been constructed. The uniqueness of this compared to conventional attosecond beam-lines is the isolation of the beam-splitter and the focusing optic. This beam-line hence allows, within the accuracy of the used optics, an aberration free imaging of the harmonic beam. An online, single-shot method for the focus characterization reveals a focal spot size of the XUV of $< 15\,\mu m$. The use of a scintillating crystal for the conversion of the XUV into visible light allows for

the use of standard optical components for the imaging of the focal spot. At the same time, this scintillating crystal limits the observable spot size because of the saturation of the material. The measured spot diameter of 15 μm is hence to be understood as an upper limit of the focal spot size. Also considering the transmission of the beam-line with an appropriate spectral filter (Sn), focused XUV intensities of $2 \times 10^{12} \frac{W}{cm^2}$ are achievable. Even higher intensities are possible by implementing filters with a broader transmission window. These high intensities allowed for the generation of photo electron spectra of Ar atoms. Electrons generated by the absorption of a single photon of the harmonic comb could be observed as well as electrons produced by two-photon above-threshold ionization. This is the first observation of a non-linear process using harmonics generated by the ROM mechanism. At the same time, this is also the first energy resolved measurement of photo electrons originating from a two-photon process induced by harmonics from solid surfaces. This constitutes a major step towards a FROG-type characterization to reveal full temporal information of this source of intense attosecond pulses and may eventually lead to the application of ROM harmonics in XUV-XUV attosecond-pump-attosecond-probe type experiments. While the results of the experiments resolve some open questions on the applicability of the harmonics off of solid surfaces, confirm some theoretical predictions and give some new insight into the process leading to the harmonic generation, still some problems remain unresolved. A very important question for future experiments is the interplay of the various interaction parameters. Especially the fine tuning of the pre-plasma scale length for a given laser parameters in order to achieve highest possible conversion efficiencies into the spectral region of interest is important, but an extremely difficult task. For the successors of LWS-20, this could also mean the judicious degradation of the temporal contrast of the laser pulse to achieve the optimum scale length.

The upgraded LWS-20 and the currently built Petawatt Field Synthesizer (PFS) [146, 147, 170] with their pulse durations of only 5 fs are promising candidates for the stable generation of isolated attosecond pulses from solid surfaces. 1D PIC simulations for LWS-20 parameters with its pulse length reduced to only 2 cycles of the electric field reveal a probability of $> 50\%$ for isolated attosecond pulse generation, when the CEP is not stabilized. This relieves the need for CEP stabilization of the laser system allowing measurements with CEP tagging [148] only. The CEP tagging technique will allow the direct correlation of the CEP with the observed harmonic substructure allowing deeper insight and better understanding into the interaction dynamics. It will also give the opportunity to measure FROG traces of multiple CEP values in a single run by sorting the received single-shot ATI spectra according to the measured CEP. The upgraded LWS-20 is supposed to have a pulse energy of $\sim 100\,mJ$. This corresponds to the reduced pulse energy of ATLAS used in the experiments presented in this thesis. Due to the much shorter pulse length of 5 fs, this pulse energy corresponds to

a higher normalized vector potential, which will supposedly lead to even higher conversion efficiencies. At the same time, the generated XUV radiation will be distributed onto less attosecond pulses. Hence, attosecond pulses with unprecedented pulse energies will become available. These will be exceeded by already scheduled upgrades of LWS-20 or the availability of the PFS.

Another remaining problem of the attosecond pulse generation on solid surfaces is the demand of a clean solid surface for the interaction. Since every shot destroys a part of the target substrate, only a limited number of shots is available before the target has to be replaced. This puts a limit on the pump-probe measurements that can be performed. Scans with too high temporal resolution, asking for too many data points exceeding the number of shots available per target are not possible. Similarly, experiments with long integration times where a large number of shots have to be accumulated are only possible within certain limits. The glass discs used throughout this thesis can sustain $1000 - 4000$ shots, which is enough for most experiments. But for ever stronger laser pulses, the damaged spots on the discs increase in size and hence reduce the number of available shots per disc. A problem directly connected to needed supply of a fresh area of target for every shot is the repetition rate of the laser. Current high-field laser systems deliver pulses from a few times per second to a few times per day. At these repetition rates, the mechanical operation to provide a fresh area of glass is easily manageable, but advances in high-intensity laser technology towards ever higher repetition rates and their first applications [96] demand new target mechanisms. In this respect, the conventional generation of high harmonics in gas jets has clear advantages. The interaction material is constantly renewed, and there are almost no limitations on available shot number or repetition rate. First results for a similar approach in the generation of high harmonics from solid surfaces are presented in appendix A. The solid target is replaced by a μm sized continuously flowing liquid jet. Similar to the gas harmonic case, no limitations on shot number or repetition rate exist. Preliminary successful experiments producing harmonics of this liquid surface have been performed. Although this is a very promising source for future experiments, a lot of research and development has to be performed before liquid jet targets will be able to replace the conventional fused silica discs.

A different way to tackle the problem of the limited amount of shots available is to use advanced, single-shot measurement techniques. For example an adaptation of the single-shot second-order auto-correlation technique to the XUV regime has been co-developed in the course of this thesis. The concept of this measurement for a train of attosecond pulses synthesized by gas harmonics is presented in figure 7.1. An isolated attosecond pulse or pulse train is split into two identical replicas, and these are subsequently focused into an interaction volume filled with gas where they overlap at an angle. The two pulses ionize the surrounding gas in the interaction volume by single-photon ionization and if the intensity
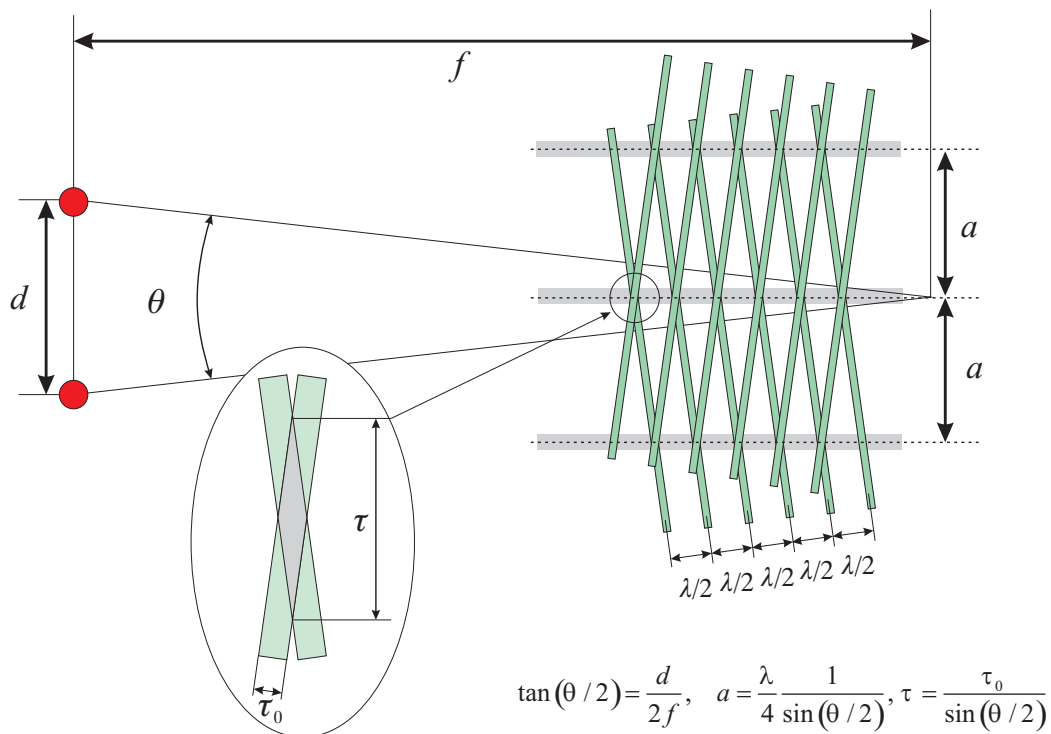
Figure 7.1.: Principle of the single-shot second-order auto-correlator. The number of visible stripes is a measure for the number of attosecond pulses in the train. The width of the stripes incorporates temporal information about the individual attosecond pulses.

of the pulses is high enough, also by two-photon ionization. As can be seen in figure 7.1 in the regions where the two pulses overlap, the intensity is higher, and accordingly, more ions are formed within these stripes. An ion microscope [171] can now be used to observe the pattern of the generated ion species. The number of stripes is a direct measure for the number of attosecond pulses that constitute the attosecond pulse train whereas the width of the stripes incorporates temporal information about the individual pulses. Instead of using a beam splitter to generate two replicas of the XUV pulse, a mask to isolate two parts of the beam can be used. In figure 7.2, a selection of different masks with their respective single- and two-photon signals are shown. First proof of principle experiments of this new technique are currently performed at the Institute of Electronic Structure and Laser (FORTH-IESL) and already delivered first results.

The high conversion efficiencies together with the applicable high laser intensities will make ultra-short pulses from solid surfaces ever more interesting, important and eventually inevitable, especially in the aspect of the advancements in laser technology. These bursts of light with unprecedented energies will ad-
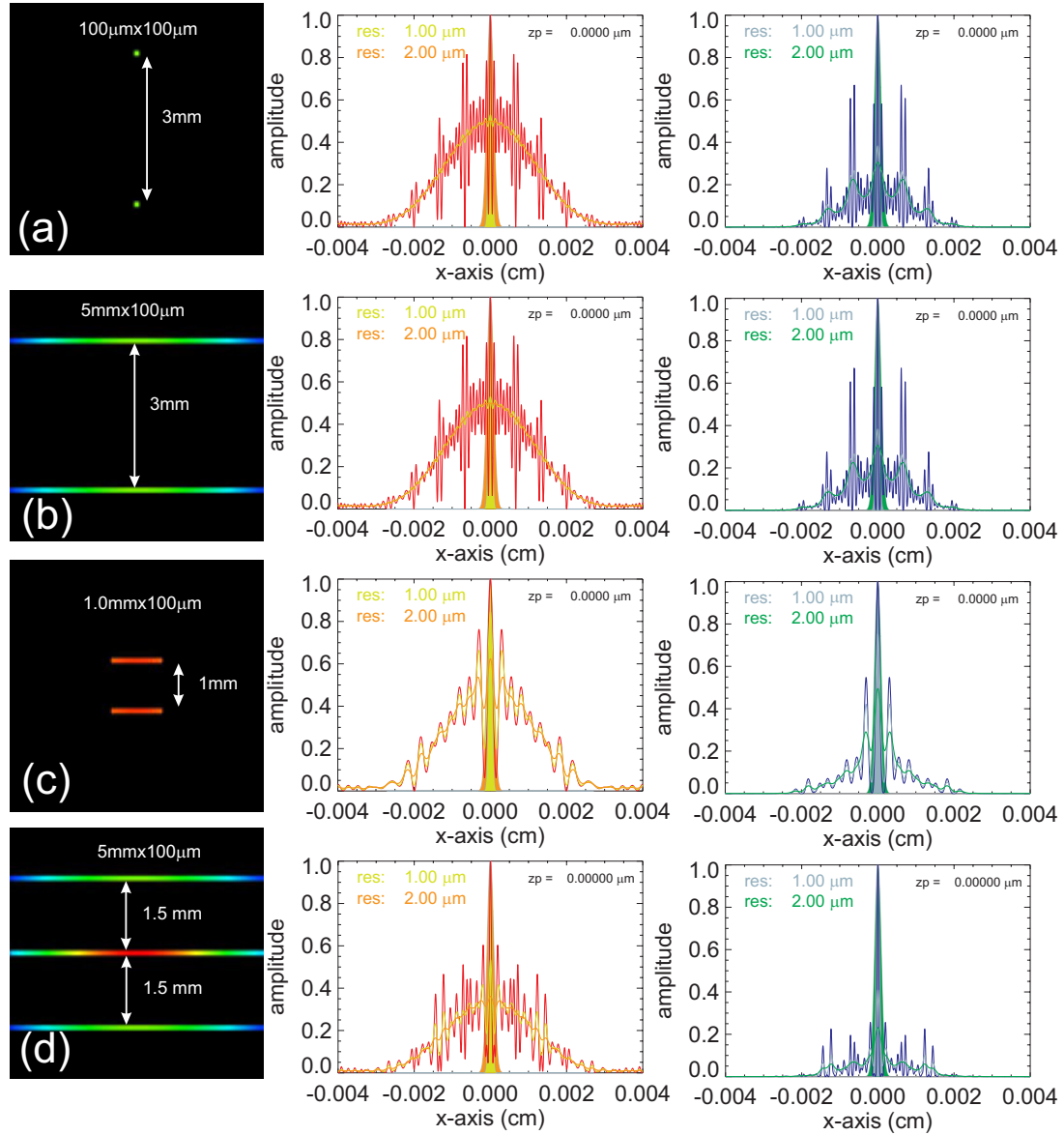
Figure 7.2.: Selection of mask designs with their respective ion signals. The left column shows various designs of masks. The middle column shows the single-photon ion signal (red). The yellow line is calculated from the red one by convolution with the microscope resolution. The right column presents the calculated two-photon signal. The green line is calculated from the blue one by convolution with the microscope resolution.

vance into new regimes of attoscience and presumably deliver new insights into dynamics on ever shorter time and length scales. But will people in ~ 30000 years from now look at the resulting images the same way we look at those cave drawings?

A. Experiments with Liquid Jets

High harmonic generation on solid surfaces demands a very clean interaction surface, making it necessary to supply a fresh target area after every shot. Conventional glass targets last only for a few hundred up to a few thousand shots, depending on target and damage spot size, before they have to be replaced. Advances in high-intensity laser technology towards ever higher repetition rates and their first applications [96] demand new target mechanisms. Especially in the prospect of the Extreme Light Infrastructure (ELI) [172], this is an urgent task for making the transition from pure exploration of these new attosecond sources to their application in e.g. XUV-pump XUV-probe type experiments. Promising candidates for a self-refreshing target with no limitations on shot number are smooth jets of liquids [173–175]. First experiments on using these jets for plasma mirrors have already been performed [176]. However, these experiments have been carried out under atmospheric pressure, limiting the focused laser power to below $10^{14} \; \frac{W}{cm^2}$.

For extending the usable laser power to intensities high enough for real applications, studies of the interaction of high power laser pulses with an atomically smooth liquid surface in the context of high harmonic generation in vacuum were performed. This broadband, coherent emission is in many aspects different from previous experiments with liquid jets which generated quasimonochromatic, incoherent XUV radiation [177].

For the experiments, the ATLAS is used as a driving laser, which is focused by a f/2 parabolic mirror. The liquid enters the chamber through a glass nozzle with a diameter on the order of $10 \; \mu m$. The nozzle is mounted in a horizontal configuration at an angle of $45°$ to the focused laser beam. The continuously flowing liquid jet propagates freely through the vacuum chamber for $\sim 0.1 \; m$ and is then collected in a double walled cylinder cooled with liquid nitrogen (see figure A.1). Using such a cold trap, a pressure in the $10^{-5} \; mbar$ regime can be sustained in the interaction chamber during jet operation. The volume of this cylinder is the only limiting factor for the time of operation of the jet. For the cold trap used in this setup, > 8 hours of uninterrupted experimental time are available, depending on nozzle size and flow rate of the liquid. By using a high pressure liquid chromatography (HPLC) pump, a steady operation of the jet can be maintained while the temperature of the liquid is controlled by a cryostat. Already after some mm of propagation, the jet starts to disperse and the surface quality degrades. Therefore, great care is taken to place the tip of the nozzle
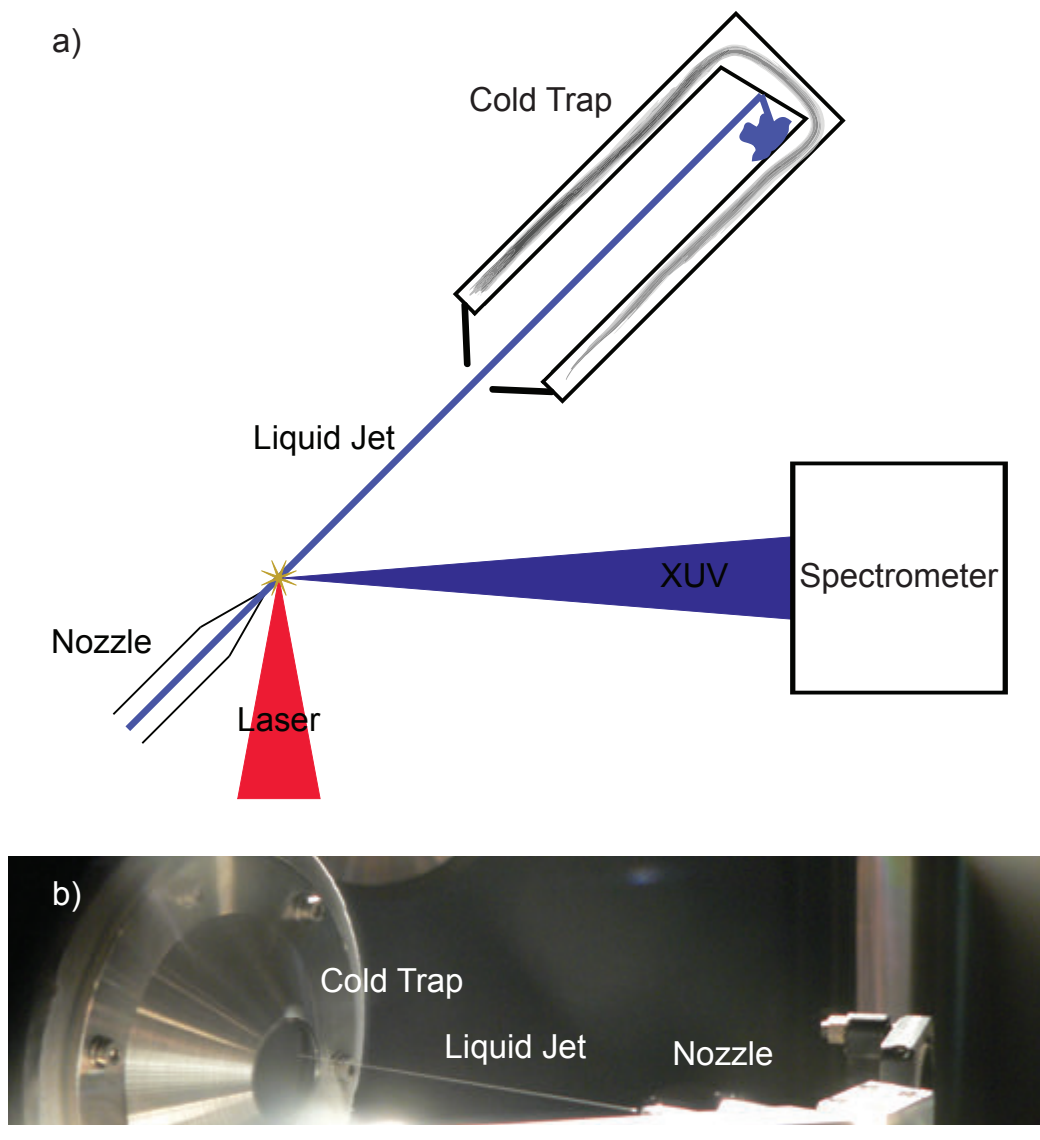
Figure A.1.: Sketch of the experimental setup a) and image of the jet in operation
b). The laser is focused on a continuously flowing liquid jet under an
angle of 45°. The liquid jet with a diameter on the order of $\sim 10\ \mu m$
enters the vacuum chamber through a circular glass nozzle in a horizontal
configuration. After propagating freely for $\sim 0.1\ m$, it enters a metallic
cylinder that is cooled by liquid nitrogen, where it freezes out. The
specularly reflected light off the liquid surface is analyzed by a XUV-
spectrometer.

very close to the focus of the laser beam. The specularly reflected light is then analysed by an Acton normal incidence XUV-spectrometer, which is described in detail in reference [87].

For choosing the target material out of a vast number of available liquids, some constraints have to be kept in mind. The liquid should be non-toxic and easy to handle. It should not react with or degrade optical coatings. And the vapour pressure should be low, since any residual gas in the interaction chamber will interact with the incoming laser beam and the outgoing XUV. Several runs with three different liquids were performed: water, an aqueous solution of LiCl and ethanol. These liquids differ in multiple parameters as e.g. vapour pressure, density, freezing point. With all three materials the generation of high-order harmonics of the driving laser frequency is possible. Although the cut-off of the CWE process is not observable due to the spectral range of the spectrometer, it is very likely that the harmonics are solely produced by the CWE mechanism. Two observations lead to this statement. First, the harmonic spectra show a fast drop in intensity towards the expected cut-off (see figure A.2). Second, only
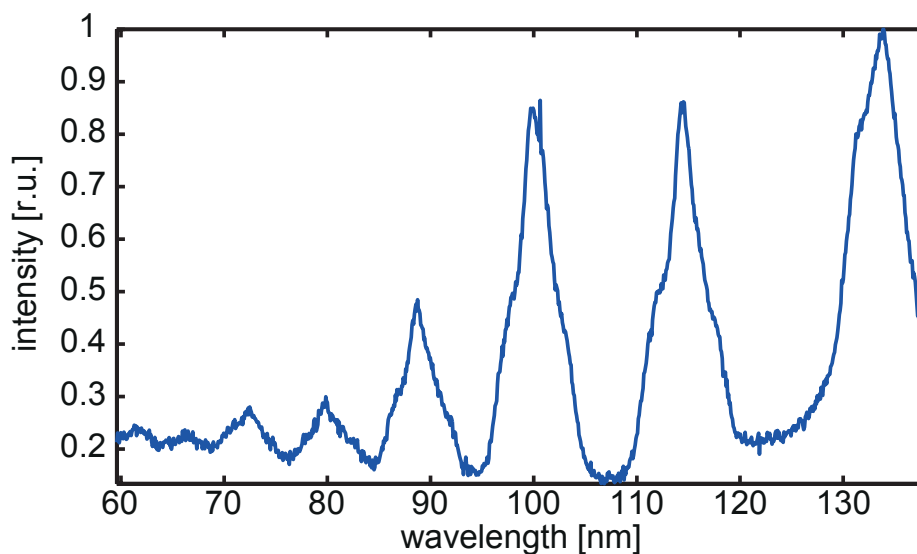
Figure A.2.: Accumulated spectrum of ~ 150 shots with $\sim 200\,mJ$ of laser energy on the target on an aqueous solution of LiCl at $-15°C$.

a very small dependence of the harmonic signal on laser intensity and target position is observed, which is in strong contrast compared to observations with ROM harmonics off of glass targets.

Notwithstanding the ability to generate harmonics off any of the three investigated liquids, they show very different behaviour during the experiments. Water, the most obvious liquid, shows over all very good performance. By cooling the water from $\sim 20°C$ down to $0°C$ and hence lowering the vapour pressure, the

harmonic signal can be enhanced by a factor of ~ 2 (see figure A.3). In figure A.4,
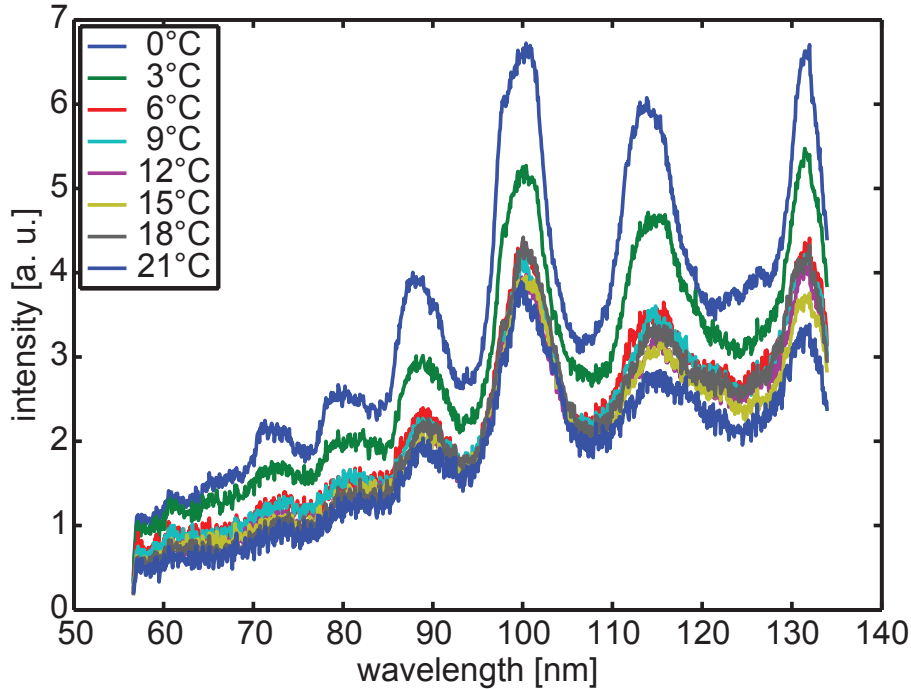

Figure A.3.: Harmonic spectra generated on a water surface for various temperature
of the liquid.

the temperature dependence of the 7th harmonic together with a double exponential fit are plotted. A fast drop towards $5°C$ and slow decay towards higher temperatures can be observed. After some time of operation, water tends to form small sticks of ice at the entrance of the cold trap (see figure A.5). These sticks grow along the incoming water jet, eventually reaching the nozzle, freezing it up and preventing further jet operation. The stick formation is not predictable and can set in at any time, from minutes to hours after starting operation. This can be circumvented by increasing the diameter of the orifice of the cold trap but only within certain limits, since this also influences the stability of operation of the jet.

By adding 7% of LiCl to the water, the freezing point is lowered, and by cooling the liquid to lower temperature the vapour pressure can be further reduced. Indeed an aqueous solution of LiCl shows improved performance over pure water. The harmonic signal strength increases by going down to $-15°C$. The issue of formation of ice at the entrance of the cold trap persists, but due to a change in the crystal structure of the formed ice, the sticks can no longer reach the nozzle but break under their own weight already after a few centimetres. A major drawback for the use of this liquid is the formation of Li and Cl ions in the laser
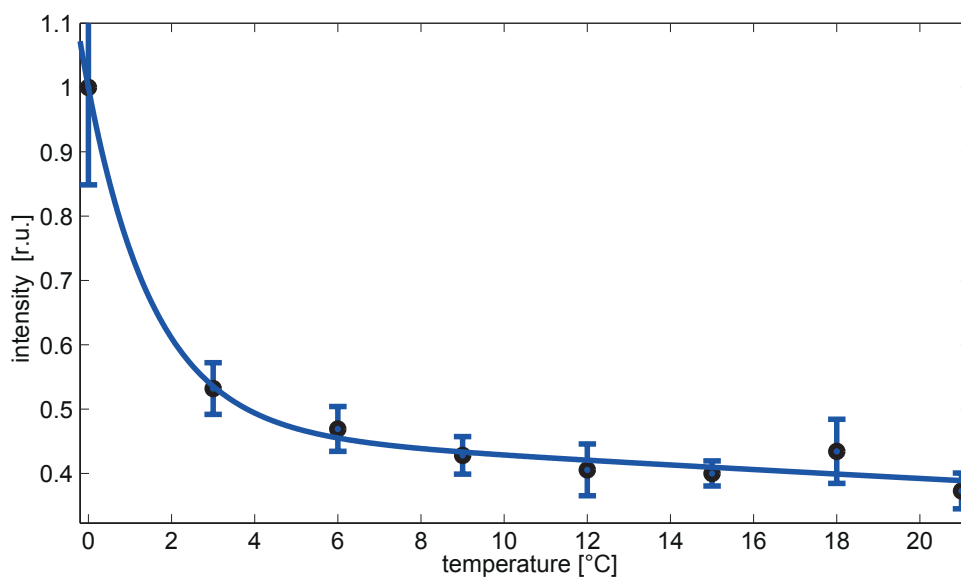
Figure A.4.: Temperature dependence of harmonic 7 using water as a target. A fast decay of the signal going from $0°C$ to $5°C$ is observed followed by a slow decay for higher temperatures.
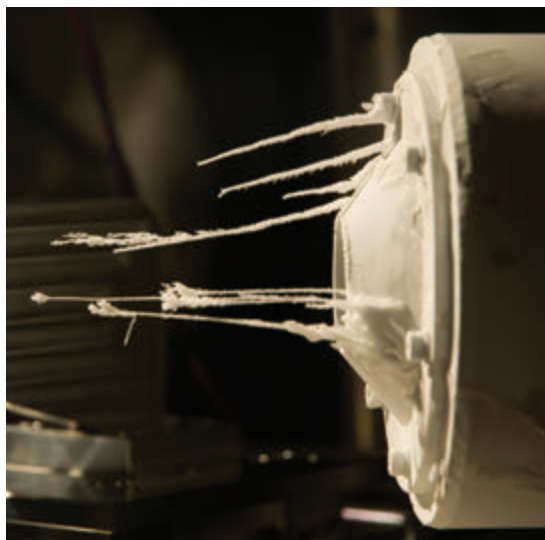

Figure A.5.: Ice sticks formed at the orifice of the cold trap, that eventually reach and block the nozzle.

focus. These ion species effectively corrode any surface, including optics, within the vacuum chamber. This leads to damaged optical coatings as well as battered mechanical parts.

The freezing point of the third liquid under consideration, ethanol, at $-114°C$ allows for even lower temperatures of operation and accompanying very low vapour pressures. This should lead to even better performance in terms of harmonic generation, but the low freezing point at the same time also hinders the efficient trapping of the liquid within the cold trap. On the one hand, this prevents formation of sticks of ice, which could congest the nozzle. But on the other hand, this also leads to a higher pressure in the 10^{-4} $mbar$ regime in the vacuum chamber and unpredictable, sudden jumps of the chamber pressure. Also an increased dose of ionizing radiation outside the vacuum chamber was detectable.

All of the used liquids share a common problem of reducing the harmonic signal detected with the spectrometer that stems from the geometry of the nozzle. For these studies, circular nozzles with diameters of $12-27\mu m$ are used to generate the liquid jet. These nozzles hence produce a circular symmetric jet with diameters in the interaction region of slightly larger size. The size of the focal spot of the laser beam is also on the scale of a few μm. Now, small fluctuations in the backing pressure of the jet or tiny movements of optical parts in the laser beam line will lead to μm jitter of the position of the jet and the focal spot respectively. These μm deviations of the perfect alignment of the laser on the cylindrical surface of the jet cause strong deflections of the reflected light off the optical axis, eventually reducing the collected signal at the spectrometer. This can only be circumvented by the use of larger diameter nozzles, which increases the gas load in the interaction chamber, or the use of flat jets. Designs for these flat jets already exist but need to be tested.

All in all, the presented results are very promising for the use of these targets in further applications, but additional investigations in target materials and nozzle configurations are necessary.

Bibliography

[1] R. Hughes and D. Bjerklie. Behold the Stone Age. *Time Magazine*, 145(6):52, 1995.

[2] R. P. Hardie and R. K. Gaye. Physica. In W. D. Ross, editor, *The Works of Aristotle*, chapter Book VII. Claredon Press, Oxford, 1930.

[3] A. Toepler. *Beobachtungen nach einer neuen optischen Methode*. Max Cohen & Sohn, Bonn, 1864.

[4] Munn & Co. A Horses Motion Scientifically Determined. *Scientific American*, 39(16):241, 1878.

[5] A. Schawlow and C. Townes. Infrared and Optical Masers. *Physical Review*, 112(6):1940–1949, 1958.

[6] T. H. Maiman. Stimulated Optical Radiation in Ruby. *Nature*, 187(4736):493–494, 1960.

[7] L. E. Hargrove, R. L. Fork, and M. A. Pollack. Locking of HeNe Laser Modes Induced by Synchronous Intracavity Modulation. *Applied Physics Letters*, 5(1):4, 1964.

[8] M. DiDomenico. Small-Signal Analysis of Internal (Coupling-Type) Modulation of Lasers. *Journal of Applied Physics*, 35(10):2870, 1964.

[9] F. J. McClung and R. W. Hellwarth. Giant Optical Pulsations from Ruby. *Journal of Applied Physics*, 33(3):828, 1962.

[10] D. Strickland and G. Mourou. Compression of amplified chirped optical pulses. *Optics Communications*, 56(3):219–221, 1985.

[11] A. Baltuška, Z. Wei, M. S. Pshenichnikov, D. A. Wiersma, and R. Szipcs. All-solid-state cavity-dumped sub-5-fs laser. *Applied Physics B: Lasers and Optics*, 65(2):175–188, 1997.

[12] M. Nisoli, S. Stagira, S. De Silvestri, O. Svelto, S. Sartania, Z. Cheng, M. Lenzner, C. Spielmann, and F. Krausz. A novel-high energy pulse compression system: generation of multigigawatt sub-5-fs pulses. *Applied Physics B: Lasers and Optics*, 65(2):189–196, 1997.

[13] G. Steinmeyer. Frontiers in Ultrashort Pulse Generation: Pushing the Limits in Linear and Nonlinear Optics. *Science*, 286(5444):1507–1512, 1999.

[14] A. H. Zewail. Laser femtochemistry. *Science*, 242(4886):1645–53, 1988.

[15] R. Szipocs, K. Ferencz, C. Spielmann, and F. Krausz. Chirped multilayer coatings for broadband dispersion control in femtosecond lasers. *Optics Letters*, 19(3):201, 1994.

[16] A. L. Cavalieri, E. Goulielmakis, B. Horvath, W. Helml, M. Schultze, M. Fieß, V. Pervak, L. Veisz, V. S. Yakovlev, M. Uiberacker, A. Apolonski, F. Krausz, and R. Kienberger. Intense 1.5-cycle near infrared laser waveforms and their use for the generation of ultra-broadband soft-x-ray harmonic continua. *New Journal of Physics*, 9(7):242–242, 2007.

[17] H.-S. Chan, Z.-M. Hsieh, W.-H. Liang, A. H. Kung, C.-K. Lee, C.-J. Lai, R.-P. Pan, and L.-H. Peng. Synthesis and measurement of ultrafast waveforms from five discrete optical harmonics. *Science*, 331(6021):1165–8, 2011.

[18] S.-w. Huang, G. Cirmi, J. Moses, K.-h. Hong, S. Bhardwaj, J. R. Birge, L.-j. Chen, E. Li, B. J. Eggleton, G. Cerullo, F. X. Ka, and F. X. Kärtner. High-energy pulse synthesis with sub-cycle waveform control for strong-field physics. *Nature Photonics*, 5(8):475–479, 2011.

[19] A. Wirth, M. T. Hassan, I. Grguras, J. Gagnon, A. Moulet, T. T. Luu, S. Pabst, R. Santra, Z. A. Alahmed, A. M. Azzeer, V. S. Yakovlev, V. Pervak, F. Krausz, and E. Goulielmakis. Synthesized light transients. *Science*, 334(6053):195–200, 2011.

[20] J. Feist, S. Nagele, C. Ticknor, B. Schneider, L. Collins, and J. Burgdörfer. Attosecond Two-Photon Interferometry for Doubly Excited States of Helium. *Physical Review Letters*, 107(9):1–5, 2011.

[21] E. Goulielmakis, M. Schultze, M. Hofstetter, V. S. Yakovlev, J. Gagnon, M. Uiberacker, a. L. Aquila, E. M. Gullikson, D. T. Attwood, R. Kienberger, F. Krausz, and U. Kleineberg. Single-cycle nonlinear optics. *Science*, 320(5883):1614–7, 2008.

[22] M. Drescher, M. Hentschel, R. Kienberger, G. Tempea, C. Spielmann, G. A. Reider, P. B. Corkum, and F. Krausz. X-ray pulses approaching the attosecond frontier. *Science*, 291(5510):1923–7, 2001.

[23] M. Hentschel, R. Kienberger, C. Spielmann, G. A. Reider, N. Milosevic, T. Brabec, P. Corkum, U. Heinzmann, M. Drescher, and F. Krausz. Attosecond metrology. *Nature*, 414(6863):509–13, 2001.

[24] P. M. Paul, E. S. Toma, P. Breger, G. Mullot, F. Auge, P. Balcou, H. G. Muller, and P. Agostini. Observation of a train of attosecond pulses from high harmonic generation. *Science*, 292(5522):1689–92, 2001.

[25] P. Corkum. Plasma perspective on strong field multiphoton ionization. *Physical Review Letters*, 71(13):1994–1997, 1993.

[26] T. W. Hänsch. A proposed sub-femtosecond pulse synthesizer using separate phase-locked laser oscillators. *Optics Communications*, 80(1):71–75, 1990.

[27] G. Farkas and C. Tóth. Proposal for attosecond light pulse generation using laser induced multiple-harmonic conversion processes in rare gases. *Physics Letters A*, 168(5-6):447–450, 1992.

[28] A. Baltuska, T. Udem, M. Uiberacker, M. Hentschel, E. Goulielmakis, C. Gohle, R. Holzwarth, V. S. Yakovlev, A. Scrinzi, T. W. Hänsch, and F. Krausz. Attosecond control of electronic processes by intense light fields. *Nature*, 421(6923):611–5, 2003.

[29] F. Krausz. Attosecond physics. *Reviews of Modern Physics*, 81(1):163–234, 2009.

[30] L. Xu, C. Spielmann, A. Poppe, T. Brabec, F. Krausz, and T. W. Hänsch. Route to phase control of ultrashort light pulses. *Optics letters*, 21(24):2008–10, 1996.

[31] A. Poppe, R. Holzwarth, A. Apolonski, G. Tempea, C. Spielmann, T. W. Hänsch, and F. Krausz. Few-cycle optical waveform synthesis. *Applied Physics B*, 72(3):373–376, 2001.

[32] M. Drescher, M. Hentschel, R. Kienberger, M. Uiberacker, V. Yakovlev, A. Scrinzi, T. Westerwalbesloh, U. Kleineberg, U. Heinzmann, and F. Krausz. Time-resolved atomic inner-shell spectroscopy. *Nature*, 419(6909):803–7, 2002.

[33] R. Kienberger, M. Hentschel, M. Uiberacker, C. Spielmann, M. Kitzler, A. Scrinzi, M. Wieland, T. Westerwalbesloh, U. Kleineberg, U. Heinzmann, M. Drescher, and F. Krausz. Steering attosecond electron wave packets with light. *Science*, 297(5584):1144–8, 2002.

[34] M. Schultze, M. Fiess, N. Karpowicz, J. Gagnon, M. Korbman, M. Hofstetter, S. Neppl, A. L. Cavalieri, Y. Komninos, T. Mercouris, C. A. Nicolaides, R. Pazourek, S. Nagele, J. Feist, J. Burgdörfer, A. M. Azzeer, R. Ernstorfer, R. Kienberger, U. Kleineberg, E. Goulielmakis, F. Krausz, and V. S. Yakovlev. Delay in photoemission. *Science*, 328(5986):1658–62, 2010.

[35] M. Holler, F. Schapper, L. Gallmann, and U. Keller. Attosecond Electron Wave-Packet Interference Observed by Transient Absorption. *Physical Review Letters*, 106(12):1–4, 2011.

[36] A. L. Cavalieri, N. Müller, T. Uphues, V. S. Yakovlev, A. Baltuska, B. Horvath, B. Schmidt, L. Blümel, R. Holzwarth, S. Hendel, M. Drescher, U. Kleineberg, P. M. Echenique, R. Kienberger, F. Krausz, and U. Heinzmann. Attosecond spectroscopy in condensed matter. *Nature*, 449(7165):1029–32, 2007.

[37] S. H. Chew, F. Suß mann, C. Spath, A. Wirth, J. Schmidt, S. Zherebtsov, A. Guggenmos, A. Oelsner, N. Weber, J. Kapaldo, A. Gliserin, M. I. Stockman, M. F. Kling, and U. Kleineberg. Time-of-flight-photoelectron emission microscopy on plasmonic structures using attosecond extreme ultraviolet pulses. *Applied Physics Letters*, 100(5):051904, 2012.

[38] E. Skantzakis, P. Tzallas, J. Kruse, C. Kalpouzos, and D. Charalambidis. Coherent continuum extreme ultraviolet radiation in the sub-100-nJ range generated by a high-power many-cycle laser field. *Optics Letters*, 34(11):1732, 2009.

[39] M. Bellini, C. Corsi, and M. Gambino. Neutral depletion and beam defocusing in harmonic generation from strongly ionized media. *Physical Review A*, 64(2):1–10, 2001.

[40] F. Ferrari, F. Calegari, M. Lucchini, C. Vozzi, S. Stagira, G. Sansone, and M. Nisoli. High-energy isolated attosecond pulses generated by above-saturation few-cycle fields. *Nature Photonics*, 4(12):875–879, 2010.

[41] J. Itatani, F. Quéré, G. Yudin, M. Ivanov, F. Krausz, and P. Corkum. Attosecond Streak Camera. *Physical Review Letters*, 88(17):1–4, 2002.

[42] M. Ivanov and O. Smirnova. How Accurate Is the Attosecond Streak Camera? *Physical Review Letters*, 107(21):1–5, 2011.

[43] S. Nagele, R. Pazourek, J. Feist, K. Doblhoff-Dier, C. Lemell, K. Tkési, and J. Burgdörfer. Time-resolved photoemission by attosecond streaking: extraction of time information. *Journal of Physics B: Atomic, Molecular and Optical Physics*, 44(8):081001, 2011.

[44] R. López-Martens, K. Varjú, P. Johnsson, J. Mauritsson, Y. Mairesse, P. Salières, M. Gaarde, K. Schafer, A. Persson, S. Svanberg, C.-G. Wahlström, and A. LHuillier. Amplitude and Phase Control of Attosecond Light Pulses. *Physical Review Letters*, 94(3):1–4, 2005.

[45] F. Quéré, Y. Mairesse, and J. Itatani. Temporal characterization of attosecond XUV fields. *Journal of Modern Optics*, 52(2):339–360, 2005.

[46] N. A. Papadogiannis, L. A. A. Nikolopoulos, D. Charalambidis, G. D. Tsakiris, P. Tzallas, and K. Witte. Two-Photon Ionization of He through a Superposition of Higher Harmonics. *Physical Review Letters*, 90(13):133902, 2003.

[47] P. Tzallas, D. Charalambidis, N. A. Papadogiannis, K. Witte, and G. D. Tsakiris. Direct observation of attosecond light bunching. *Nature*, 426(6964):267–71, 2003.

[48] P. Tzallas, D. Charalambidis, N. a. Papadogiannis, K. Witte, and G. D. Tsakiris. Second-order autocorrelation measurements of attosecond XUV pulse trains. *Journal of Modern Optics*, 52(2):321–338, 2005.

[49] Y. Nomura, R. Hörlein, P. Tzallas, B. Dromey, S. Rykovanov, Z. Major, J. Osterhoff, S. Karsch, L. Veisz, M. Zepf, D. Charalambidis, F. Krausz, and G. D. Tsakiris. Attosecond phase locking of harmonics emitted from laser-produced plasmas. *Nature Physics*, 5(2):124–128, 2008.

[50] T. Sekikawa, A. Kosuge, T. Kanai, and S. Watanabe. Nonlinear optics in the extreme ultraviolet. *Nature*, 432(7017):605–8, 2004.

[51] Y. Nabekawa, H. Hasegawa, E. J. Takahashi, and K. Midorikawa. Production of Doubly Charged Helium Ions by Two-Photon Absorption of an Intense Sub-10-fs Soft X-Ray Pulse at 42 eV Photon Energy. *Physical Review Letters*, 94(4):1–4, 2005.

[52] K. Midorikawa, Y. Nabekawa, and A. Suda. XUV multiphoton processes with intense high-order harmonics. *Progress in Quantum Electronics*, 32(2):43–88, 2008.

[53] P. Tzallas, E. Skantzakis, L. A. A. Nikolopoulos, G. D. Tsakiris, and D. Charalambidis. Extreme-ultraviolet pumpprobe studies of one-femtosecond-scale electron dynamics. *Nature Physics*, 7(10):781–784, 2011.

[54] A. Saenz and P. Lambropoulos. Theoretical two-, three- and four-photon ionization cross sections of helium in the XUV range. *Journal of Physics B: Atomic, Molecular and Optical Physics*, 32(23):5629–5637, 1999.

[55] S. Laulan and H. Bachau. Correlation effects in two-photon single and double ionization of helium. *Physical Review A*, 68(1):1–6, 2003.

[56] K. T. Kim, K. S. Kang, M. N. Park, T. Imran, G. Umesh, and C. H. Nam. Comparison of RABITT and FROG measurements in the temporal characterization of attosecond pulse trains. *Arxiv preprint arXiv:0707.4228*, pages 3–6, 2007.

[57] Y. Mairesse and F. Quéré. Frequency-resolved optical gating for complete reconstruction of attosecond bursts. *Physical Review A*, 71(1):1–4, 2005.

[58] G. Sansone, E. Benedetti, F. Calegari, C. Vozzi, L. Avaldi, R. Flammini, L. Poletto, P. Villoresi, C. Altucci, R. Velotta, S. Stagira, S. De Silvestri, and M. Nisoli. Isolated single-cycle attosecond pulses. *Science*, 314(5798):443–6, 2006.

[59] J. Gagnon, E. Goulielmakis, and V. Yakovlev. The accurate FROG characterization of attosecond pulses from streaking measurements. *Applied Physics B*, 92(1):25–32, 2008.

[60] M. Kohler, C. Ott, P. Raith, R. Heck, I. Schlegel, C. Keitel, and T. Pfeifer. High Harmonic Generation Via Continuum Wave-Packet Interference. *Physical Review Letters*, 105(20):203902, 2010.

[61] V. Tosa, H. T. Kim, I. J. Kim, and C. H. Nam. High-order harmonic generation by chirped and self-guided femtosecond laser pulses. II. Time-frequency analysis. *Phys. Rev. A*, 71(6):063808—-, 2005.

[62] M. C. Chen, P. Arpin, T. Popmintchev, M. Gerrity, B. Zhang, M. Seaberg, D. Popmintchev, M. M. Murnane, and H. C. Kapteyn. Bright, Coherent, Ultrafast Soft X-Ray Harmonics Spanning the Water Window from a Tabletop Light Source. *Physical Review Letters*, 105(17):173901, 2010.

[63] T. Popmintchev, M.-C. Chen, P. Arpin, M. M. Murnane, and H. C. Kapteyn. The attosecond nonlinear optics of bright coherent X-ray generation. *Nature Photonics*, 4(12):822–832, 2010.

[64] A. Willner, F. Tavella, M. Yeung, T. Dzelzainis, C. Kamperidis, M. Bakarezos, D. Adams, M. Schulz, R. Riedel, M. Hoffmann, W. Hu, J. Rossbach, M. Drescher, N. Papadogiannis, M. Tatarakis, B. Dromey, and M. Zepf. Coherent Control of High Harmonic Generation via Dual-Gas Multijet Arrays. *Physical Review Letters*, 107(17):1–5, 2011.

[65] A. Willner, F. Tavella, M. Yeung, T. Dzelzainis, C. Kamperidis, M. Bakarezos, D. Adams, R. Riedel, M. Schulz, M. C. Hoffmann, W. Hu, J. Rossbach, M. Drescher, V. S. Yakovlev, N. a. Papadogiannis, M. Tatarakis, B. Dromey, and M. Zepf. Efficient control of quantum paths via dual-gas high harmonic generation. *New Journal of Physics*, 13(11):113001, 2011.

[66] G. D. Tsakiris, K. Eidmann, J. Meyer-ter Vehn, and F. Krausz. Route to intense single attosecond pulses. *New Journal of Physics*, 8(06):19–19, 2006.

[67] N. H. Burnett, H. a. Baldis, M. C. Richardson, and G. D. Enright. Harmonic generation in CO2 laser target interaction. *Applied Physics Letters*, 31(3):172, 1977.

[68] R. Carman, C. Rhodes, and R. Benjamin. Observation of harmonics in the visible and ultraviolet created in CO$_2$-laser-produced plasmas. *Physical Review A*, 24(5):2649–2663, 1981.

[69] R. Carman, D. Forslund, and J. Kindel. Visible Harmonic Emission as a Way of Measuring Profile Steepening. *Physical Review Letters*, 46(1):29–32, 1981.

[70] Y. Nomura. *Temporal characterization of harmonic radiation generated by intense laser-plasma interaction.* PhD thesis, Ludwig-Maximilians-Universität München, 2008.

[71] U. Teubner and P. Gibbon. High-order harmonics from laser-irradiated plasma surfaces. *Reviews of Modern Physics*, 81(2):445–479, 2009.

[72] C. Thaury and F. Quéré. High-order harmonic and attosecond pulse generation on plasma mirrors: basic mechanisms. *Journal of Physics B: Atomic, Molecular and Optical Physics*, 43(21):213001, 2010.

[73] D. Herrmann, L. Veisz, R. Tautz, F. Tavella, K. Schmid, V. Pervak, and F. Krausz. Generation of sub-three-cycle, 16 TW light pulses by using noncollinear optical parametric chirped-pulse amplification. *Optics Letters*, 34(16):2459, 2009.

[74] P. Heissler, R. Hörlein, J. M. Mikhailova, L. Waldecker, P. Tzallas, A. Buck, K. Schmid, C. M. S. Sears, F. Krausz, L. Veisz, M. Zepf, and G. D. Tsakiris. Few-cycle driven relativistically oscillating plasma mirrors - a source of intense, isolated attosecond pulses [accepted]. *Physical Review Letters*.

[75] L. Waldecker, P. Heissler, R. Hörlein, K. Allinger, M. Heigoldt, K. Khrennikov, J. Wenz, S. Karsch, F. Krausz, and G. D. Tsakiris. Focusing of high order harmonics from solid density plasmas. *Plasma Physics and Controlled Fusion*, 53(12):124021, 2011.

[76] P. Heissler, P. Tzallas, J. M. Mikhailova, K. Khrennikov, L. Waldecker, F. Krausz, S. Karsch, D. Charalambidis, and G. D. Tsakiris. Two-photon above-threshold ionization using extreme-ultraviolet harmonic emis-

sion from relativistic laserplasma interaction. *New Journal of Physics*, 14(4):043025, 2012.

[77] D. J. Kane and R. Trebino. Characterization of arbitrary femtosecond pulses using frequency-resolved optical gating. *IEEE Journal of Quantum Electronics*, 29(2):571–579, 1993.

[78] J. Griffiths, David. *Introduction to Electrodynamics (3rd Edition)*. Prentice Hall of India/Benjamin Cummings, 1998.

[79] P. Gibbon. *Short Pulse Laser Interactions with Matter: An Introduction*. World Scientific Publishing Company, London, 2005.

[80] W. L. Kruer. *The Physics of Laser Plasma Interactions (Frontiers in Physics)*. Westview Press, 2003.

[81] F. Brunel. Not-so-resonant, resonant absorption. *Physical Review Letters*, 59(1):52–55, 1987.

[82] U. Teubner, K. Eidmann, U. Wagner, U. Andiel, F. Pisani, G. Tsakiris, K. Witte, J. Meyer-ter Vehn, T. Schlegel, and E. Förster. Harmonic Emission from the Rear Side of Thin Overdense Foils Irradiated with Intense Ultrashort Laser Pulses. *Physical Review Letters*, 92(18):1–4, 2004.

[83] F. Quéré, C. Thaury, P. Monot, S. Dobosz, P. Martin, J.-P. Geindre, and P. Audebert. Coherent wake emission of high-order harmonics from overdense plasmas. *Physical review letters*, 96(12):125004, 2006.

[84] C. Thaury, F. Quéré, J.-P. Geindre, A. Levy, T. Ceccotti, P. Monot, M. Bougeard, F. Réau, P. DOliveira, P. Audebert, R. Marjoribanks, and P. Martin. Plasma mirrors for ultrahigh-intensity optics. *Nature Physics*, 3(6):424–429, 2007.

[85] F. Quéré, C. Thaury, H. George, J. P. Geindre, E. Lefebvre, G. Bonnaud, S. Hüller, P. Monot, and P. Martin. Basic mechanisms of laser high-order harmonic generation from plasma mirrors. *Journal of Modern Optics*, 55(16):2711–2721, 2008.

[86] R. Hörlein, Y. Nomura, J. Osterhoff, Z. Major, S. Karsch, F. Krausz, and G. D. Tsakiris. High harmonics from solid surfaces as a source of ultrabright XUV radiation for experiments. *Plasma Physics and Controlled Fusion*, 50(12):124002, 2008.

[87] R. Hörlein. *Investigation of the XUV Emission from the Interaction of Intense Femtosecond Laser Pulses with Solid Targets*. PhD thesis, Ludwig-Maximilians-Universität München, 2009.

[88] M. Zepf, G. D. Tsakiris, G. Pretzler, I. Watts, D. M. Chambers, P. A. Norreys, U. Andiel, A. E. Dangor, K. Eidmann, C. Gahn, A. Machacek, J. Wark, and K. Witte. Role of the plasma scale length in the harmonic generation from solid targets. *Physical Review E*, 58(5):R5253–R5256, 1998.

[89] P. Heissler, R. Hörlein, M. Stafe, J. M. Mikhailova, Y. Nomura, D. Herrmann, R. Tautz, S. G. Rykovanov, I. B. Földes, K. Varjú, F. Tavella, A. Marcinkevicius, F. Krausz, L. Veisz, and G. D. Tsakiris. Toward single attosecond pulses using harmonic emission from solid-density plasmas. *Applied Physics B*, 101(3):511–521, 2010.

[90] T. Stix. Radiation and Absorption Via Mode Conversion in an Inhomogeneous Collision-Free Plasma. *Physical Review Letters*, 15(23):878–882, 1965.

[91] Z.-M. Sheng, K. Mima, J. Zhang, and H. Sanuki. Emission of Electromagnetic Pulses from Laser Wakefields through Linear Mode Conversion. *Physical Review Letters*, 94(9):95003, 2005.

[92] R. Hörlein, Y. Nomura, P. Tzallas, S. G. Rykovanov, B. Dromey, J. Osterhoff, Z. Major, S. Karsch, L. Veisz, M. Zepf, D. Charalambidis, F. Krausz, and G. D. Tsakiris. Temporal characterization of attosecond pulses emitted from solid-density plasmas. *New Journal of Physics*, 12(4):043020, 2010.

[93] F. Quéré, C. Thaury, J.-P. Geindre, G. Bonnaud, P. Monot, and P. Martin. Phase Properties of Laser High-Order Harmonics Generated on Plasma Mirrors. *Physical Review Letters*, 100(9):95004, 2008.

[94] C. Thaury, H. George, F. Quéré, R. Loch, J.-P. Geindre, P. Monot, and P. Martin. Coherent dynamics of plasma mirrors. *Nature Physics*, 4(8):631–634, 2008.

[95] S. G. Rykovanov, M. Geissler, J. Meyer-ter Vehn, and G. D. Tsakiris. Intense single attosecond pulses from surface harmonics using the polarization gating technique. *New Journal of Physics*, 10(2):025025, 2008.

[96] A. Borot, A. Malvache, X. Chen, D. Douillet, G. Iaquianiello, T. Lefrou, P. Audebert, J.-P. Geindre, G. Mourou, F. Quéré, and R. Lopez-Martens. High-harmonic generation from plasma mirrors at kilohertz repetition rate. *Optics letters*, 36(8):1461–3, 2011.

[97] A. Borot, A. Malvache, X. Chen, A. Jullien, J.-P. Geindre, P. Audebert, G. Mourou, F. Quéré, and R. Lopez-Martens. Attosecond control of collective electron motion in plasmas. *Nature Physics*, 8(4):1–6, 2012.

[98] I. Földes. Harmonic generation in plasmas of different density gradients. *Physics Letters A*, 258(4-6):312–316, 1999.

[99] B. Dromey, S. Rykovanov, D. Adams, R. Hörlein, Y. Nomura, D. Carroll, P. Foster, S. Kar, K. Markey, P. McKenna, D. Neely, M. Geissler, G. Tsakiris, and M. Zepf. Tunable Enhancement of High Harmonic Emission from Laser Solid Interactions. *Physical Review Letters*, 102(22):1–4, 2009.

[100] R. Hörlein, S. Steinke, A. Henig, S. Rykovanov, M. Schnürer, T. Sokollik, D. Kiefer, D. Jung, X. Yan, T. Tajima, J. Schreiber, M. Hegelich, P. Nickles, M. Zepf, G. Tsakiris, W. Sandner, and D. Habs. Dynamics of nanometer-scale foil targets irradiated with relativistically intense laser pulses. *Laser and Particle Beams*, pages 1–6, 2011.

[101] A. Einstein. Zur Elektrodynamik bewegter Körper. *Annalen der Physik*, 322(10):891–921, 1905.

[102] S. Gordienko, A. Pukhov, O. Shorokhov, and T. Baeva. Relativistic Doppler Effect: Universal Spectra and Zeptosecond Pulses. *Physical Review Letters*, 93(11):1–4, 2004.

[103] S. V. Bulanov, N. M. Naumova, and F. Pegoraro. Interaction of an ultra-short, relativistically strong laser pulse with an overdense plasma. *Physics of Plasmas*, 1(3):745, 1994.

[104] S. Gordienko, A. Pukhov, O. Shorokhov, and T. Baeva. Coherent Focusing of High Harmonics: A New Way Towards the Extreme Intensities. *Physical Review Letters*, 94(10):1–4, 2005.

[105] T. Baeva, S. Gordienko, and A. Pukhov. Relativistic plasma control for single attosecond x-ray burst generation. *Physical Review E*, 74(6):2–5, 2006.

[106] T. Baeva, S. Gordienko, and A. Pukhov. Scalable Dynamics of High Energy Relativistic Electrons: Theory, Numerical Simulations and Experimental Results. *Astrophysics and Space Science*, 307(1-3):335–340, 2006.

[107] T. Baeva, S. Gordienko, and A. Pukhov. Theory of high-order harmonic generation in relativistic laser interaction with overdense plasma. *Physical Review E*, 74(4):1–11, 2006.

[108] T. Baeva, S. Gordienko, and A. Pukhov. Relativistic plasma control for single attosecond pulse generation: Theory, simulations, and structure of the pulse. *Laser and Particle Beams*, 25(03):339–346, 2007.

[109] P. Gibbon. Harmonic Generation by Femtosecond Laser-Solid Interaction: A Coherent Water-Window Light Source? *Physical Review Letters*, 76(1):50–53, 1996.

[110] L. Plaja, L. Roso, K. Rzazewski, and M. Lewenstein. Generation of attosecond pulse trains during the reflection of a very intense laser on a solid surface. *Journal of the Optical Society of America B*, 15(7):1904, 1998.

[111] N. M. Naumova, J. a. Nees, I. V. Sokolov, B. Hou, and G. a. Mourou. Relativistic Generation of Isolated Attosecond Pulses in a $\lambda\hat{\ }\{3\}$ Focal Volume. *Physical Review Letters*, 92(6):3–6, 2004.

[112] N. M. Naumova, C. P. Hauri, J. a. Nees, I. V. Sokolov, R. Lopez-Martens, and G. a. Mourou. Towards efficient generation of attosecond pulses from overdense plasma targets. *New Journal of Physics*, 10(2):025022, 2008.

[113] M. Geissler, S. Rykovanov, J. Schreiber, J. Meyer-ter Vehn, and G. D. Tsakiris. 3D simulations of surface harmonic generation with few-cycle laser pulses. *New Journal of Physics*, 9(7):218–218, 2007.

[114] D. an der Brugge and A. Pukhov. Propagation of relativistic surface harmonics radiation in free space. *Physics of Plasmas*, 14(9):093104, 2007.

[115] D. an der Brugge and A. Pukhov. Enhanced relativistic harmonics by electron nanobunching. *Physics of Plasmas*, 17(3):033110, 2010.

[116] R. Lichters, J. Meyer-ter Vehn, and A. Pukhov. Short-pulse laser harmonics from oscillating plasma surfaces driven at relativistic intensity. *Physics of Plasmas*, 3(9):3425, 1996.

[117] T. J. M. Boyd and R. Ondarza-Rovira. Plasma Modulation of Harmonic Emission Spectra from Laser-Plasma Interactions. *Physical Review Letters*, 98(10):1–4, 2007.

[118] T. J. M. Boyd and R. Ondarza-Rovira. Anomalies in Universal Intensity Scaling in Ultrarelativistic Laser-Plasma Interactions. *Physical Review Letters*, 101(12):1–4, 2008.

[119] T. J. M. Boyd and R. Ondarza-Rovira. Power law decay of harmonic spectra in ultrarelativistic laser-plasma interactions. *Physics of Plasmas*, 17(8):080701, 2010.

[120] T. J. M. Boyd and R. Ondarza-Rovira. Plasma effects in attosecond pulse generation. *Physics Letters A*, 374(13-14):1517–1521, 2010.

[121] P. A. Norreys, M. Zepf, S. Moustaizis, A. P. Fews, J. Zhang, P. Lee, M. Bakarezos, C. N. Danson, A. Dyson, P. Gibbon, P. Loukakos, D. Neely, F. N. Walsh, J. S. Wark, and A. E. Dangor. Efficient Extreme UV Harmonics Generated from Picosecond Laser Pulse Interactions with Solid Targets. *Physical Review Letters*, 76(11):1832–1835, 1996.

[122] A. Tarasevitch, K. Lobov, C. Wünsche, and D. von der Linde. Transition to the Relativistic Regime in High Order Harmonic Generation. *Physical Review Letters*, 98(10):10–13, 2007.

[123] B. Dromey, M. Zepf, A. Gopal, K. Lancaster, M. S. Wei, K. Krushelnick, M. Tatarakis, N. Vakakis, S. Moustaizis, R. Kodama, M. Tampo, C. Stoeckl, R. Clarke, H. Habara, D. Neely, S. Karsch, and P. Norreys. High harmonic generation in the relativistic limit. *Nature Physics*, 2(7):456–459, 2006.

[124] B. Dromey, S. Kar, C. Bellei, D. Carroll, R. Clarke, J. Green, S. Kneip, K. Markey, S. Nagel, P. Simpson, L. Willingale, P. McKenna, D. Neely, Z. Najmudin, K. Krushelnick, P. Norreys, and M. Zepf. Bright Multi-keV Harmonic Generation from Relativistically Oscillating Plasma Surfaces. *Physical Review Letters*, 99(8):1–4, 2007.

[125] B. Dromey, D. Adams, R. Hörlein, Y. Nomura, S. G. Rykovanov, D. C. Carroll, P. S. Foster, S. Kar, K. Markey, P. McKenna, D. Neely, M. Geissler, G. D. Tsakiris, and M. Zepf. Diffraction-limited performance and focusing of high harmonics from relativistic plasmas. *Nature Physics*, 5(2):146–152, 2009.

[126] M. Behmke, C. Rödel, M. Heyer, M. Kübel, T. Toncian, O. Jackel, M. Toncian, H. C. Ahlswede, D. Hemmers, U. Teubner, O. Willi, G. G. Paulus, and G. Pretzler. Surface harmonics generation with a 100 TW table-top laser system. In *Proceedings of SPIE*, volume 7501, pages 75010A–75010A–8, 2009.

[127] M. Behmke, D. an der Brügge, C. Rödel, M. Cerchez, D. Hemmers, M. Heyer, O. Jäckel, M. Kübel, G. Paulus, G. Pretzler, A. Pukhov, M. Toncian, T. Toncian, and O. Willi. Controlling the Spacing of Attosecond Pulse Trains from Relativistic Surface Plasmas. *Physical Review Letters*, 106(18):1–4, 2011.

[128] I. Watts, M. Zepf, E. Clark, M. Tatarakis, K. Krushelnick, A. Dangor, R. Allott, R. Clarke, D. Neely, and P. Norreys. Dynamics of the Critical Surface in High-Intensity Laser-Solid Interactions: Modulation of the XUV Harmonic Spectra. *Physical Review Letters*, 88(15):8–11, 2002.

[129] K. Krushelnick, I. Watts, M. Tatarakis, A. Gopal, U. Wagner, F. N. Beg, E. L. Clark, R. J. Clarke, A. E. Dangor, P. A. Norreys, M. S. Wei, and M. Zepf. Using self-generated harmonics as a diagnostic of high intensity laser-produced plasmas. *Plasma Physics and Controlled Fusion*, 44(12B):B233–B245, 2002.

[130] U. Teubner, G. Pretzler, T. Schlegel, K. Eidmann, E. Förster, and K. Witte. Anomalies in high-order harmonic generation at relativistic intensities. *Physical Review A*, 67(1):1–11, 2003.

[131] R. Lichters. *Relativistische Wechselwirkung intensiver kurzer Laserpulse mit überdichten Plasmen: Erzeugung hoher Harmonischer.* PhD thesis, Max-Planck-Institut für Quantenoptik, 1997.

[132] H. George, F. Quéré, C. Thaury, G. Bonnaud, and P. Martin. Mechanisms of forward laser harmonic emission from thin overdense plasmas. *New Journal of Physics*, 11(11):113028, 2009.

[133] K. Krushelnick, W. Rozmus, U. Wagner, F. N. Beg, S. G. Bochkarev, E. L. Clark, A. E. Dangor, R. G. Evans, A. Gopal, H. Habara, S. Mangles, P. Norreys, A. Robinson, M. Tatarakis, M. Wei, and M. Zepf. Effect of Relativistic Plasma on Extreme-Ultraviolet Harmonic Emission from Intense Laser-Matter Interactions. *Physical Review Letters*, 100(12):125005, 2008.

[134] A. S. Pirozhkov, S. V. Bulanov, T. Z. Esirkepov, M. Mori, A. Sagisaka, and H. Daido. Generation of high-energy attosecond pulses by the relativistic-irradiance short laser pulse interacting with a thin foil. *Physics Letters A*, 349(1-4):256–263, 2006.

[135] A. S. Pirozhkov, S. V. Bulanov, T. Z. Esirkepov, M. Mori, A. Sagisaka, and H. Daido. Attosecond pulse generation in the relativistic regime of the laser-foil interaction: The sliding mirror model. *Physics of Plasmas*, 13(1):013107, 2006.

[136] S. Kohlweyer. *Erzeugung von Harmonischen durch Reflexion hochintensiver Laserpulse an einem überdichten Plasma.* PhD thesis, Max-Planck-Institut für Quantenoptik, 1996.

[137] E. Rácz, I. B. Földes, G. Kocsis, G. Veres, K. Eidmann, and S. Szatmári. On the effect of surface rippling on the generation of harmonics in laser plasmas. *Applied Physics B*, 82(1):13–18, 2005.

[138] S. C. Wilks, W. L. Kruer, M. Tabak, and A. B. Langdon. Absorption of ultra-intense laser pulses. *Physical Review Letters*, 69(9):1383–1386, 1992.

[139] D. Chambers, P. Norreys, A. Dangor, R. Marjoribanks, S. Moustaizis, D. Neely, S. Preston, J. Wark, I. Watts, and M. Zepf. Feasibility study of high harmonic generation from short wavelength lasers interacting with solid targets. *Optics Communications*, 148(4-6):289–294, 1998.

[140] J. Schwinger. On Gauge Invariance and Vacuum Polarization. *Physical Review*, 82(5):664–679, 1951.

[141] H. Vincenti and F. Quéré. Attosecond Lighthouses: How To Use Spatiotemporally Coupled Light Fields To Generate Isolated Attosecond Pulses. *Physical Review Letters*, 108(11):1–5, 2012.

[142] S. Akturk, X. Gu, P. Bowlan, and R. Trebino. Spatio-temporal couplings in ultrashort laser pulses. *Journal of Optics*, 12(9):093001, 2010.

[143] G. Pretzler, a. Kasper, and K. Witte. Angular chirp and tilted light pulses in CPA lasers. *Applied Physics B: Lasers and Optics*, 70(1):1–9, 2000.

[144] P. Tzallas, E. Skantzakis, C. Kalpouzos, E. P. Benis, G. D. Tsakiris, and D. Charalambidis. Generation of intense continuum extreme-ultraviolet radiation by many-cycle laser fields. *Nature Physics*, 3(12):846–850, 2007.

[145] T. H. Dou, R. Tautz, X. Gu, G. Marcus, T. Feurer, F. Krausz, and L. Veisz. Dispersion control with reflection grisms of an ultra-broadband spectrum approaching a full octave. *Optics Express*, 18(26):27900, 2010.

[146] Z. Major, S. A. Trushin, I. Ahmad, M. Siebold, C. Wandt, S. Klingebiel, T.-j. Wang, J. A. Fülöp, A. Henig, S. Kruber, R. Weingartner, A. Popp, J. Osterhoff, R. Hörlein, J. Hein, V. Pervak, A. Apolonski, F. Krausz, and S. Karsch. Basic Concepts and Current Status of the Petawatt Field Synthesizer - A New Approach to Ultrahigh Field Generation. *The Review of Laser Engineering*, 37(6):431–436, 2009.

[147] S. Klingebiel, C. Wandt, C. Skrobol, I. Ahmad, S. a. Trushin, Z. Major, F. Krausz, and S. Karsch. High energy picosecond Yb:YAG CPA system at 10 Hz repetition rate for pumping optical parametric amplifiers. *Optics Express*, 19(6):5357, 2011.

[148] T. Wittmann, B. Horvath, W. Helml, M. G. Schätzel, X. Gu, A. L. Cavalieri, G. G. Paulus, and R. Kienberger. Single-shot carrierenvelope phase measurement of few-cycle laser pulses. *Nature Physics*, 5(5):357–362, 2009.

[149] A. Dubietis, G. Jonušauskas, and A. Piskarskas. Powerful femtosecond pulse generation by chirped and stretched pulse parametric amplification in BBO crystal. *Optics Communications*, 88(4-6):437–440, 1992.

[150] A. Buck. *Advanced characterization and control of laser wakefield acceleration*. PhD thesis, Ludwig-Maximilians-Universität München, 2011.

[151] J. M. Mikhailova, A. Buck, A. Borot, K. Schmid, C. M. S. Sears, G. D. Tsakiris, F. Krausz, and L. Veisz. Ultra-high-contrast few-cycle pulses for multipetawatt-class laser technology. *Optics Letters*, 36(16):3145, 2011.

[152] Y. Ralchenko, A. E. Kramida, J. Reader, and N. A. T. (2011). NIST Atomic Spectra Database (ver. 4.1.0), 2011.

[153] S. G. Rykovanov, H. Ruhl, J. Meyer-ter Vehn, R. Hörlein, B. Dromey, M. Zepf, and G. D. Tsakiris. Plasma surface dynamics and smoothing in the relativistic few-cycle regime. *New Journal of Physics*, 13(2):023008, 2011.

[154] A. Popp. Private Communications, 2011.

[155] B. Henke. X-Ray Interactions: Photoabsorption, Scattering, Transmission, and Reflection at E = 50-30,000 eV, Z = 1-92. *Atomic Data and Nuclear Data Tables*, 54(2):181–342, 1993.

[156] Andor. http://www.andor.com/pdfs/spec_sheets/DO440.pdf.

[157] D. Neely, D. Chambers, C. Danson, P. Norreys, S. Preston, F. Quinn, M. Roper, J. Wark, and M. Zepf. A multi-channel soft X-ray flat-field spectrometer. In *AIP Conference Proceedings*, volume 479, pages 479–484, 1998.

[158] IRD. http://www.ird-inc.com/index.html.

[159] Y. Kobayashi, T. Sekikawa, Y. Nabekawa, and S. Watanabe. 27-fs extreme ultraviolet pulse generation by high-order harmonics. *Optics Letters*, 23(1):64, 1998.

[160] Y. Kobayashi, T. Ohno, T. Sekikawa, Y. Nabekawa, and S. Watanabe. Pulse width measurement of high-order harmonics by autocorrelation. *Applied Physics B: Lasers and Optics*, 70(3):389–394, 2000.

[161] O. Faucher, P. Tzallas, E. P. Benis, J. Kruse, A. Peralta Conde, C. Kalpouzos, and D. Charalambidis. Four-dimensional investigation of the 2nd order volume autocorrelation technique. *Applied Physics B*, 97(2):505–510, 2009.

[162] L. Nikolopoulos, E. Benis, P. Tzallas, D. Charalambidis, K. Witte, and G. Tsakiris. Second Order Autocorrelation of an XUV Attosecond Pulse Train. *Physical Review Letters*, 94(11):1–4, 2005.

[163] N. Miyamoto, M. Kamei, D. Yoshitomi, T. Kanai, T. Sekikawa, T. Nakajima, and S. Watanabe. Observation of Two-Photon Above-Threshold Ionization of Rare Gases by xuv Harmonic Photons. *Physical Review Letters*, 93(8):1–4, 2004.

[164] Y. Nabekawa, T. Shimizu, T. Okino, K. Furusawa, H. Hasegawa, K. Yamanouchi, and K. Midorikawa. Interferometric Autocorrelation of an Attosecond Pulse Train in the Single-Cycle Regime. *Physical Review Letters*, 97(15):1–4, 2006.

[165] C. Iaconis and I. A. Walmsley. Spectral phase interferometry for direct electric-field reconstruction of ultrashort optical pulses. *Optics Letters*, 23(10):792, 1998.

[166] E. Cormier, I. Walmsley, E. Kosik, A. Wyatt, L. Corner, and L. DiMauro. Self-Referencing, Spectrally, or Spatially Encoded Spectral Interferometry for the Complete Characterization of Attosecond Electromagnetic Pulses. *Physical Review Letters*, 94(3):1–4, 2005.

[167] T. Sekikawa, T. Katsura, S. Miura, and S. Watanabe. Measurement of the Intensity-Dependent Atomic Dipole Phase of a High Harmonic by Frequency-Resolved Optical Gating. *Physical Review Letters*, 88(19):3–6, 2002.

[168] E. D. Palik. *Handbook of Optical Constants of Solids, Five-Volume Set: Handbook of Optical Constants of Solids: Volume 1 (Academic Press Handbook)*. Academic Press Inc., 1985.

[169] L. Waldecker. Charakterisierung und Optimierung des Fokus kohärenter XUV-Strahlung von Oberflächen. Diploma thesis, Ludwig-Maximilians-Universität München, 2011.

[170] Z. Major, T.-j. Wang, I. Ahmad, S. Trushin, J. Hein, C. Wandt, S. Klingebiel, A. Popp, H. Rainer, V. Pervak, A. Apolonski, and S. Karsch. OPA development on the Petawatt Field Synthesizer. *OSA/ASSP*, (i):5–7, 2009.

[171] M. Schultze, B. Bergues, H. Schröder, F. Krausz, and K. L. Kompa. Spatially resolved measurement of ionization yields in the focus of an intense laser pulse. *New Journal of Physics*, 13(3):033001, 2011.

[172] J.-P. Chambaret, O. Chekhlov, G. Cheriaux, J. Collier, R. Dabu, P. Dombi, A. M. Dunne, K. Ertel, P. Georges, J. Hebling, J. Hein, C. Hernandez-Gomez, C. Hooker, S. Karsch, G. Korn, F. Krausz, C. Le Blanc, Z. Major, F. Mathieu, T. Metzger, G. Mourou, P. Nickles, K. Osvay, B. Rus,

W. Sandner, G. Szabo, D. Ursescu, and K. Varju. Extreme light infrastructure: laser architecture and major challenges. In *Library*, volume 7721, pages 77211D–77211D–15, 2010.

[173] M. Faubel and T. Kisters. Non-equilibrium molecular evaporation of carboxylic acid dimers. *Nature*, 339(6225):527–529, 1989.

[174] M. Faubel, S. Schlemmer, and J. P. Toennies. A molecular beam study of the evaporation of water from a liquid jet. *Zeitschrift für Physik D Atoms, Molecules and Clusters*, 10(2-3):269–277, 1988.

[175] A. Charvat, E. Lugovoj, M. Faubel, and B. Abel. New design for a time-of-flight mass spectrometer with a liquid beam laser desorption ion source for the analysis of biomolecules. *Review of Scientific Instruments*, 75(5):1209, 2004.

[176] D. Panasenko, A. J. Shu, C. B. Schroeder, A. J. Gonsalves, K. Nakamura, N. H. Matlis, E. Cormier-Michel, G. Plateau, C. Lin, C. Toth, C. G. R. Geddes, E. Esarey, and W. P. Leemans. Staging Laser Plasma Accelerators for Increased Beam Energy. In C. B. Schroeder, W. Leemans, and E. Esarey, editors, *AIP Conference Proceedings*, volume 1086 of *American Institute of Physics Conference Series*, pages 215–220. AIP, 2009.

[177] B. Kim, B. Ahn, D. Lee, J. Kim, and D. Kim. Optimization of laser parameters for the maximum efficiency in the generation of water-window radiation using a liquid nitrogen jet. *Applied Physics Letters*, 88(14):141501, 2006.

Data Storage and Analysis

The experimental raw data, the simulation files, the evaluation files and the figures can be found on the archive server of the Laboratory for Attosecond Physics of the Max Planck Institute of Quantum Optics. The files are ordered by chapter. The software used for evaluation is either Matlab, OriginPro or IDL. The experimental raw data is placed in a folder named by the day the data was acquired.

- **Chapter 2**

  Figure 2.1 Introduction of ionization types

  > **figure file** chapter2\IonizationMechanisms.pdf

  Figure 2.2 Illustration of laser contrast

  > **figure file** chapter2\LaserContrast.pdf

- **Chapter 3**

  Figure 3.1 Model calculations and PIC simulations of the CWE process

  > **raw data and evaluation** see archived data for Heissler et al., Applied Physics B 101, 511 (2010); [89]

  > **figure file** chapter3\CWEtraj.pdf

  Figure 3.2 Illustration of the CWE process

  > **figure file** chapter3\CWEdepth.pdf

  Figure 3.3 Sample CWE spectrum

  > **raw data** chapter3\CWEspec\20100312\image_414.sif

  > **evaluation** chapter3\CWEspec\McPherson_mod_multi.m

  > **figure file** chapter3\CWEspec.pdf

  Figure 3.4 Model calculations of the CWE process with a 3 cycle and a 15 cycle pulse, respectively

  > **evaluation** see archived data for Heissler et al., Applied Physics B 101, 511 (2010); [89]

  > **figure file** chapter3\3cyc15cyccomp.pdf

Figure 3.5 Comparison of model calculations, PIC simulations and experimental results

> **raw data and evaluation** see archived data for Heissler et al., Applied Physics B 101, 511 (2010); [89]

> **figure file** chapter3\ExpModPICa.pdf

Figure 3.6 Illustration of the ROM process

> **figure file** chapter3\TsakMod.pdf

Figure 3.7 Model of the ROM process

> **figure file** chapter3\TsakModMo.pdf

Figure 3.8 Illustration of the lighthouse effect

> **evaluation** chapter3\lighthouse\lighthouse.m

> **figure file** chapter3\lighthouse.pdf

Figure 3.9 PIC simulations for the ROM process with a few-cycle driving laser, for two CEP values

> **raw data and evaluation** see archived data for Heissler et al., Physical Review Letters, (2012); [74]

> **figure file** chapter3\TwoPicCas.pdf

Figure 3.10 PIC simulations for the ROM process with a few-cycle driving laser, for 40 CEP values

> **evaluation** see archived data for Heissler et al., Physical Review Letters, (2012); [74]

> **figure file** chapter3\FortyPicCas.pdf

- **Chapter 4**

Figure 4.1 Spectrum, second- and third-order auto-correlation trace of LWS-20

> **raw data** chapter4\LWSPar\20100317\AC20100317-2002.txt

> **evaluation** chapter4\LWSPar\20100317\contrast.OPJ

> **raw data** chapter4\LWSPar\20100331\SHG AC fspix 0.233 form 1.3 fwhm 8.6 av 8.7.txt

> **evaluation** chapter4\LWSPar\20100331\SHG.OPJ

> **figure file** chapter4\LWSPar.pdf

Figure 4.2 Focus-diagnostic of LWS-20

    raw data chapter4\LWSFoc\20100331\LWS_BA.tiff

    evaluation chapter4\LWSFoc\Focus_Evaluation.m

    figure file chapter4\LWSFoc.pdf

Figure 4.3 Experimental setup

    figure file chapter4\TagStaSet.pdf

Figure 4.4 Spectrometer calibration using emission of oxygen

    evaluation chapter4\Ospec

    figure file chapter4\Ospec.pdf

Figure 4.5 Raw CCD image of harmonic spectrum

    raw data chapter4\LWSRawSpec\20100326\image_401.sif

    evaluation chapter3\CWEspec\McPherson_mod_multi.m

    tabulated data chapter4\LWSRawSpec\oxygenlines_160_180A.dat

    figure file chapter4\LWSRawHarma.pdf

Figure 4.6 Gaussian fits to spectrum of figure 4.5

    raw data chapter4\LWSFitSpec\20100326\image_495.sif

    evaluation chapter3\CWEspec\McPherson_mod_multi.m

    evaluation chapter4\LWSFitSpec\harmonic-bandwidth.opj

    figure file chapter4\LWSRawHarmb.pdf

Figure 4.7 Intensity scan of harmonic emission

    raw data all files in chapter4\Irisscan\20100326

    simulation data all files in chapter4\Irisscan\LPIC-intens-sim

    evaluation chapter3\CWEspec\McPherson_mod_multi.m and

    evaluation chapter4\Irisscan\Focus_Evaluation_Iris_scan.m

    figure file chapter4\LWSIrisscan.pdf

Figure 4.8 Comparison of experimental spectra

    raw data and evaluation see archived data for Heissler et al., Physical Review Letters, (2012); [74]

    figure file chapter4\LWSRomSpec.pdf

- **Chapter 5**

Figure 5.1 FROG trace and Contrast of ATLAS

    raw data chapter5\ATLASPar\20110517\2run.bmp and atlas_contrast_-
    110517.txt

    figure file chapter5\ATLASPar.pdf

Figure 5.2 Focus of ATLAS

    raw data all files in chapter5\ATLASFoc\20101220

    evaluation chapter4\LWSFoc\Focus_Evaluation.m

    figure file chapter5\AtlasFoc.pdf

Figure 5.3 Focus of ATLAS

    figure file chapter5\setup.pdf

Figure 5.4 Comparison of harmonic spectra generated with three different
laser energies

    raw data all files in chapter5\Comp3En\20110417 and chapter5\Comp3En\20110803

    evaluation chapter3\CWEspec\McPherson_mod_multi.m

    figure file chapter5\Comp3En.pdf

Figure 5.5 Three XUV beam-profiles and image reconstruction

    raw data all files in chapter5\CompMCP\20110803 and chapter5\CompMCP\20110804

    evaluation chapter5\CompMCP\proc_guangjin.m and

    evaluation chapter5\CompMCP\proc_guangjin_2.m and

    evaluation chapter5\CompMCP\ellipsefit_ver2.m and

    evaluation chapter5\CompMCP\surffit_ver2.m

    figure file chapter5\beamprofilesb.pdf

Figure 5.6 Influence of angular chirp on XUV properties

    evaluation chapter3\lighthouse\lighthouse.m

    figure file chapter5\spatiotemp.pdf

Figure 5.7 Charge measurement with calibrated diode

    raw data all files in chapter5\CharMea\20110804

    evaluation chapter5\CharMea\signal_read_10V_bias.m

    figure file chapter5\ChargeMea.pdf

Figure 5.8 Combined harmonic spectrum spanning Al filter transmission
window

    raw data chapter5\Combspec\20110417\image_153.sif

  raw data chapter5\Combspec\20110901\image_40.sif

  evaluation chapter3\CWEspec\McPherson_mod_multi.m and

  evaluation chapter5\Combspec\Calibration.m and

  evaluation chapter5\Combspec\Calibration_vec.m

  tabulated data chapter5\Combspec\qe_axuv.txt and

  tabulated data chapter5\Combspec\TR10nmAl2O3.dat and

  tabulated data chapter5\Combspec\TR150nmAl.dat and

  tabulated data chapter5\Combspec\TR1250nmAl.dat and

  figure file chapter5\Combspec.pdf

Figure 5.9 Various transmission and quantum efficiencies

  figure file chapter5\TransEff.pdf

Figure 5.10 Comparison of PIC simulations and experimental results

  raw data all files in chapter5\PICComp\20110804

  simulation data all files in chapter5\PICComp\LPIC-sim

  evaluation MATLAB routines in chapter5\Combspec and chapter5\CharMea

  figure file chapter5\PIC.pdf

- **Chapter 6**

Figure 6.1 Illustrations of the XUV beamline

  figure file chapter6\beamline.pdf

Figure 6.2 Calculated transmission of the beamline for various filters

  evaluation chapter6\BeamTran

  figure file chapter6\Transmission.pdf

Figure 6.3 Measurements of XUV foci for three different filter settings

  evaluation see archived data for Waldecker et al., Plasma Physics and Controlled Fusion 53, 124021 (2011); [75]

  figure file chapter6\3foci.pdf

Figure 6.4 Calculated spectrum in interaction region

  tabulated data chapter6\BeamTran\Al_140nm.txt and

  tabulated data chapter6\BeamTran\Al2O3_10nm.txt and

  tabulated data chapter6\BeamTran\Al150nm.txt and

  tabulated data chapter6\BeamTran\In150nm.txt and

tabulated data chapter6\BeamTran\Sn150nm.txt and

tabulated data chapter6\BeamTran\SiO2optprop.CSV and

tabulated data chapter6\BeamTran\Sioptprop.CSV and

tabulated data chapter6\BeamTran\roughness.xls

evaluation chapter6\BeamTran\Transmission.m in combination with chapter5\Combspec

figure file chapter6\TransSpec.pdf

Figure 6.5 Possible harmonic combinations for ATI

figure file chapter6\ATI_Spectrum.pdf

Figure 6.6 Measured photo electron spectra

evaluation see archived data for Heissler et al., New Journal of Physics 14, 043025 (2012); [76]

figure file chapter6\ATISpec.pdf

Figure 6.7 Comparison of measured and calculated spectrum

evaluation see archived data for Heissler et al., New Journal of Physics 14, 043025 (2012); [76] and evaluation for figure 6.4

figure file chapter6\TranPEa.pdf

Figure 6.8 Non-linearity of the process

evaluation see archived data for Heissler et al., New Journal of Physics 14, 043025 (2012); [76]

figure file chapter6\NonLin.pdf

Chapter 7

Figure 7.1 Illustration of the single-shot XUV second-order auto-correlation

figure file chapter7\SSAC.pdf

Figure 7.2 Calculated signals for different mask designs

figure file chapter7\SSAC_masks.pdf

- **Appendix A**

Figure A.1 Experimental setup

figure file Appendix\Setup.pdf

Figure A.2 Harmonic spectrum off of a liquid jet

raw data chapter6\LJ\Spec\20100916\image020.pmi

> **evaluation** chapter6\LJ\TempScan\LJ_Temp_scan.m
>
> **figure file** chapter6\Spec.pdf

Figure A.3 Temperature dependence of the harmonic spectrum

> **raw data** all files in chapter6\LJ\TempScan\20100315
>
> **evaluation** chapter6\LJ\TempScan\LJ_Temp_scan.m
>
> **figure file** chapter6\TempScan.pdf

Figure A.4 Temperature dependence of the 7th harmonic

> **raw data** all files in chapter6\LJ\TempScan\20100315
>
> **evaluation** chapter6\LJ\TempScan\LJ_Temp_scan.m
>
> **figure file** chapter6\Tempdep.pdf

Figure A.5 Ice formation at cold trap

> **figure file** chapter6\Ice.pdf

Publications

Published Papers

- **P. Heissler**, P. Tzallas, J.M. Mikhailova, K. Khrennikov, L. Waldecker, F. Krausz, S. Karsch, D. Charalambidis, G.D. Tsakiris, *'Two-photon above-threshold ionization using extreme-ultraviolet harmonic emission from relativistic laserplasma interaction'*, New Journal of Physics 14, 043025 (2012)

- L. Waldecker, **P. Heissler**, R. Hoerlein, K. Allinger, M. Heigoldt, K. Khrennikov, J. Wenz, S. Karsch, F. Krausz, G. D. Tsakiris, *'Focussing of high order harmonics from solid density plasmas'*, Plasma Physics and Controlled Fusion 53, 124021 (2011)

- **P. Heissler**, R. Hörlein, M. Stafe, J.M. Mikhailova, Y. Nomura, D. Herrmann, R. Tautz, S.G. Rykovanov, I.B. Földes, K. Varjú, F. Tavella, A. Marcinkevicius, F. Krausz, L. Veisz, G.D. Tsakiris, *'Toward single attosecond pulses using harmonic emission from solid-density plasmas'*, Applied Physics B 101, 511 (2010)

Accepted Papers

- **P. Heissler**, R. Hörlein, J. M. Mikhailova, L. Waldecker, P. Tzallas, A. Buck, K. Schmid, C. M. S. Sears, F. Krausz, L. Veisz, M. Zepf, G. D. Tsakiris, *'Few-cycle driven relativistically oscillating plasma mirrors - a source of intense, isolated attosecond pulses'*, Physical Review Letters, accepted

In Preparation

- **P. Heissler**, A. Barna, J. M. Mikhailova, K. Khrennikov, S. Karsch, L. Veisz, F. Krausz, I. B. Földes, G.D. Tsakiris, *'Efficiency and divergence measurements of relativistic harmonics from solid targets'*, In preparation

- **P. Heissler**, E. Lugovoy, R. Hörlein, L. Waldecker, J. Wenz, M. Heigoldt, K. Khrennikov, S. Karsch, F. Krausz, B. Abel, G. D. Tsakiris, *'High-harmonic generation using liquid jets'*, In preparation

- I. B. Földes, **P. Heissler**, R. Hörlein, M. Stafe, J. M. Mikhailova, K. Varjú, F. Krausz, L. Veisz and G. D. Tsakiris, *'Investigations of polarization of high-harmonics from solid-density plasmas'*, In preparation

- P. Tzallas, G. Kolliopoulos, A. C. Paolo, D. Charalambidis, **P. Heissler**, B. Bergues, H. Schröder, G. D. Tsakiris, *'A single-shot XUV auto-correlator'*, In preparation

Acknowledgements

Especially I would like to thank Nick Borys not only for proof reading and correcting the manuscript of this thesis but also for showing me the beauty of rock climbing, cinco de mayo celebrations and the taste of peanut butter and jelly sandwiches.

Zu guter Letzt möchte ich mich bei meiner Familie bedanken, welche mich während meiner gesamten Studiendauer immer unterstützt hat und mir diese Arbeit damit überhaupt ermöglichte. Speziell meiner Ehefrau Patricia, die während den Jahren stets verständnisvoll an meiner Seite stand und meiner Tochter Emilia Leticia, die immer zur rechten Zeit ein Lächeln für mich bereit hielt, möchte ich danken.

Curriculum Vitae

Peronal Data

Name: Patrick Heißler

Date of birth: 06.12.1981

Place of birth: Augsburg, Germany

Citizenship: Germany

Education

07/2008 - present   Ph.D. student (continued)
Max Planck Institute of Quantum Optics, Garching, Germany and
Ludwig-Maximilians-Universität München, Munich, Germany
Thesis: Relativistic Laser Plasma Interaction: A Novel Route to Intense, Single Attosecond Pulses
Supervisor: Prof. Ferenc Krausz

03/2007 - 02/2008   Diploma thesis
Chair for Photonics and Optoelectronics at the
Ludwig-Maximilians-Universität München, Munich, Germany
Thesis: Influence of Magnetic Fields on Conjugated Polymers
Supervisor: Prof. Jochen Feldmann

10/2004 - 02/2008   Graduate student
Ludwig-Maximilians-Universität München, Munich, Germany

10/2002 - 10/2004   Undergraduate student
University of Augsburg, Augsburg, Germany

06/2001   Abitur
Maria-Theresia-Gymnasium, Augsburg, Germany

Academic Experience

03/2008 - 05/2008   Visiting scientist
Group of Prof. John Lupton at the
University of Utah, Salt Lake City, USA

10/2007 - 02/2008   Tutor for solid state physics exercise classes
                    Ludwig-Maximilians-Universität München, Munich, Germany

02/2005 - 03/2005   Working student
                    Chair for Photonics and Optoelectronics at the
                    Ludwig-Maximilians-Universität München, Munich, Germany
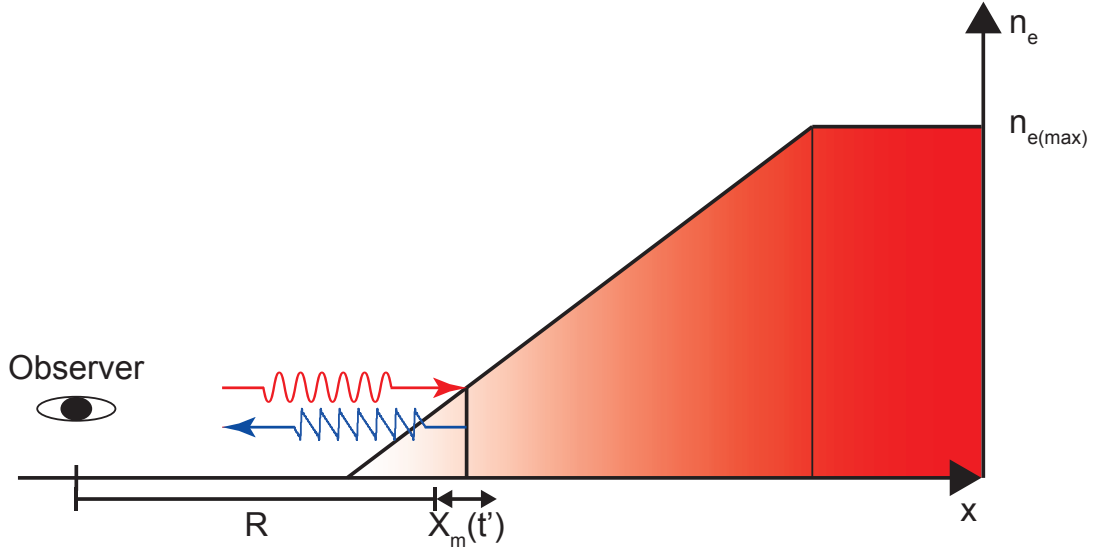
May 21, 2012

Figure 3.6.: Illustration of the oscillating mirror model. The incident electric field of the laser is reflected off an oscillating layer of electrons. The phase of the reflected field seen by the observer depends on the position of this layer at the time of reflection. These phase distortions lead to a strong harmonic content in the reflected field.

due to the complicated interplay of the forces within the plasma. But as Baeva, Gordienko and Pukhov show in their so-called BGP-model [107], the emitted harmonic spectrum shows universal features that are independent of the exact form of the function $X_m(t')$. Hence, a reasonable simplification is that the motion of the electrons closely follows the $\mathbf{v} \times \mathbf{B}$ force, with a phase shift ϕ_m and a time dependent amplitude $A_m = \frac{\lambda_L}{4\pi} \frac{a_0}{\sqrt{1+a_0^2}}$ [66]. The time of arrival of the laser pulse at the oscillating surface is then given by:

$$t' = t + \frac{R + X_m(t')}{c} \tag{3.4}$$

with the function for the motion

$$X_m(t') = \frac{\lambda_L}{4\pi} \frac{a_0}{\sqrt{1+a_0^2}} \sin(2\omega_L t' + \phi_m). \tag{3.5}$$

By solving this implicit function for t', it is possible to calculate the reflected field $E_{ref}(t) \propto \sin(\omega_L t + 2k_L X(t'))$ seen by the observer at time $t + 2(t' - t)$, omitting the constant phase terms $2k_L R$ and ϕ_m. Since the laser is reflected by a moving surface, its frequency is shifted by the doppler effect. The important quantity for the shift is the maximum velocity v_{max} of the reflecting object, which
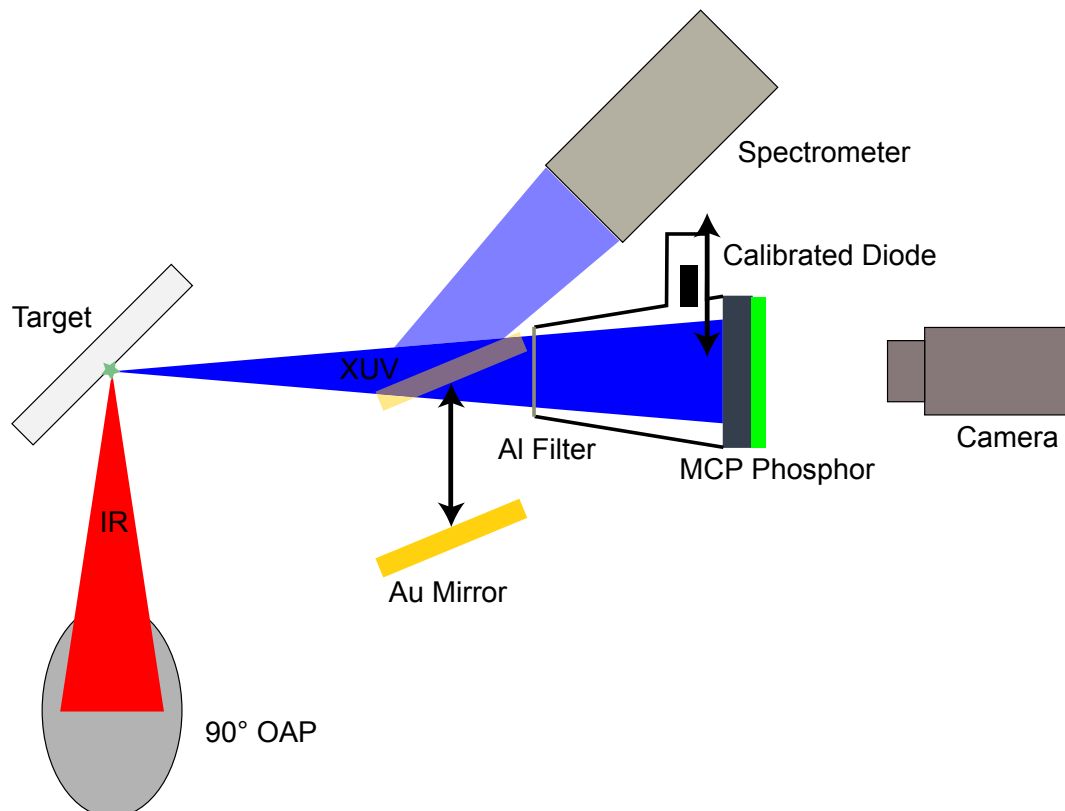
Figure 5.3.: A 90° off-axis parabolic mirror focuses the laser beam onto a fused silica target. The generated XUV beam enters a light sealed chamber and hits a MCP detector connected to a phosphor screen that is imaged by a 14-bit CCD camera. An absolutely calibrated photo diode can be moved into the beam. To control the emitted harmonic spectrum, the beam can be coupled into a flat-field spectrometer by a gold mirror.
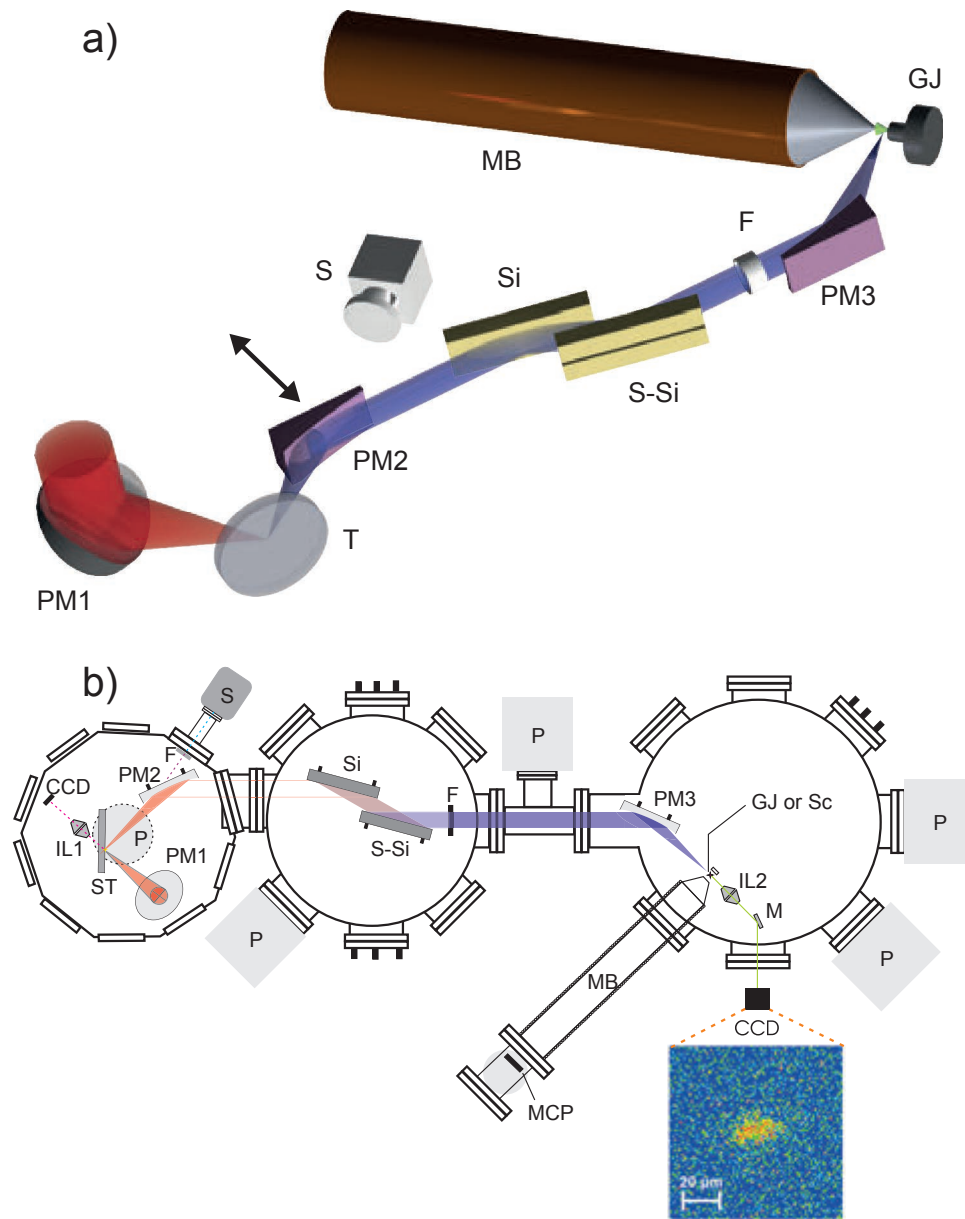
Figure 6.1.: A 3D scheme of the SHHG beam-line is shown in a), and a technical
drawing, that shows also the layout of the vacuum chambers and pumping
stages (P) is illustrated in b). The XUV beam-line consists of a 90° off-
axis parabolic mirror (PM1) to focus the IR, a fused silica target, a flat-
field spectrometer (S), a 135° off-axis recollimation parabola (PM2), a
flat Si mirror (Si), a horizontally split Si mirror (S-Si), a filter bench (F),
a focusing 130° off-axis parabola (PM3), a gas jet (GJ) in combination
with a magnetic-bottle time-of-flight spectrometer (MB) or a scintillating
crystal (SC) in combination with an imaging system (I-L) and a CCD
camera.